Dual beam FIB methods for nano-prototyping and their application in magnetic thin film sensor development and microscopy

August 2021

PhD Thesis in Physics

written by

Björn Büker

Bielefeld University

Department of Physics

Declaration of authorship I hereby certify that the work presented in this dissertation is my original work without the use of anything other than the listed resources. All ideas that are not mine have been fully and properly acknowledged.

(Björn Büker)

Reviewers:

- Prof. Dr. Andreas Hütten
- Prof. Dr. Thomas Huser

Acknowledgments

Here, I would like to thank everyone, who helped to make this work possible.
First and foremost my heartfelt thanks go out to Andreas Hütten, who as a supervisor gave me this opportunity and continued to support me in my efforts, especially when experiments did not do what they were supposed to. I would also like to thank the other members of the examination committee Thomas Huser, Gabi Schierning, and Thomas Dahm.
For spending countless hours with me in the laboratory, preparing experiments and discussing successes and failures alike, I would like to thank my Master's students and friends Laila Bondzio and Pierre Maurice Piel. Laila did a fantastic job preparing FEBID-Co structures, as well as direct-write granular GMR structures using the FIB. She will also take over the collaboration with Double Helix Optics in the future. Pierre proved to be talented with lithography and prepared interesting nanopatterned GMR structures. Without you two, this work would not be the same.
I would like to thank Andreas Hütten for supporting this work with micromagnetic simulations, as well as Daniela Ramermann, Inga Ennen, and Judith Bünte for their outstanding work on the TEM taking magnetic images of my samples and the following discussions of the results. A special thanks goes to Karsten Rott, who is an irreplaceable part of the D2 group at Bielefeld University and who supported me through many discussions and repair sessions on the FIB. I also thank all current and former colleagues from D2 for fun times in the break room, at barbecues, Christmas parties, at conferences, or after-work outings. My office colleagues Martin Gottschalk, who taught me the ways of the FIB, Andreas "Manni" Becker and Nadine Fokin deserve a special mention here.
Deserving of particular gratitude are my parents Andreas and Margret Büker, my grandparents Helmut and Christel Büker, as well as other family members who always encouraged me to push forward. Thank you for your love, support, and understanding.
Lastly, I would like to thank all friends who were with me on this journey. Thank you for your support, patience, and much needed distraction. You know who you are.

Contents

1 Introduction

When Ernst Rustka and Max Knoll built the first prototype electron microscope with a magnification of 400x in 1931 in Berlin, they could barely imagine what future developments would do to improve their invention. In just a few decades the maximum magnification and resolution of electron microscopes increased a thousandfold. Since the invention of the transistor in 1947 at Bell Laboratories, the definition of "small" has been redefined on more than one occasion, and as the ability to observe the micro- and nanoworld evolved, the technology of miniaturization evolved with it. In 2012, researchers at IBM managed to successfully store a single data bit in a magnetic structure consisting of only 12 atoms. This, as well as their famous stop motion video "A boy and his atom", which was created by manipulating single atoms using the tip of a scanning tunneling microscope (STM), were just a proof of concept and not ready for commercial use, but modern electron microscopy methods still played a critical role in the successful miniaturization of today's electronics.
A large part of the strive toward miniaturization was driven by the semiconductor and magnetic storage industry, where processors needed to be smaller and faster, and as the amount of processed data increased, so did the need for space and energy efficient data storage. Electron beam lithography systems in the factories of market leaders like Intel realize transistors in the order of tens of nanometers, which is far beyond the resolution limit of any photo-optical or mechanical abrasive process. With the help of modern nanofabrication methods, technology that once filled entire buildings is now carried around day to day in people's pockets.
Even though fields like magnetic storage and circuit miniaturization are still at the forefront of industrial research, nanotechnology has become more accessible in recent years. As electron and ion microscopes become more readily available, methods that have been previously exclusive to the semiconductor industry and related fields of research have become more widespread. Today, anti-reflective coatings with a thickness of a few hundred nanometers are used naturally in photography lenses and eyeglasses, and electron or ion microscopy is also used in biology, chemistry, or mechanical engineering. These new interdisciplinary connections bear the potential for excellent new methods in both fundamental research and practical technological innovations that will soon be used in everyday life. Compared to many conventional fabrication methods on a larger scale that have been known and perfected for decades or more, nanotechnology is still in its infancy. For that reason, the unexplored phenomena and the potential for entirely new ideas are still plentiful.
One of the core aims of this work is to explore the potential of well-known nanofabrication methods like lithography and comparatively new techniques like dual beam microscopy in new contexts that make use of their outstanding versatility. This thesis consists of three main topics that each use different aspects of these techniques. Building on several past projects in the 'Thin films and physics of nanostructures' research group at Bielefeld University, the first topic of this work deals with the fabrication and characterization of granular magnetoresistive sensors. Both a bottom-up process that uses a direct-write approach for the creation of nanoparticles from a metal-organic precursor gas similar to a nano-3D-printer, and a top-down method that uses a focused ion beam to cut highly ordered nanostructures from thin films are thoroughly explored and assessed based on their merit in giant magnetoresistance devices. The second topic compares focused ion beam methods and a lithography

approach to the prototyping of high precision optical devices for super-resolution microscopy. This interdisciplinary project was supported by Double Helix Optics LLC, a company that specializes in optical components for various types of laser microscopy.
In the last section of this work, the nanofabrication methods presented in the previous chapters are used to create highly ordered nanopatterns in magnetic thin films and magnetic multilayer systems that exhibit the giant magnetoresistance effect (GMR). These patterns significantly alter the magnetic properties of the films and provide a fresh take on the effect of magnetic Lorentz fields, a phenomenon that has been well known since the 1960s, but was never thoroughly investigated using modern nanofabrication methods. Nanopatterned GMR sensors of various sizes and symmetries were prepared using both focused ion beam and lithography methods and their electrical transport properties were characterized. Along with the transmission electron microscopy (TEM) group around Daniela Ramermann, Inga Ennen and Judith Bünte it was possible to directly image the magnetic order in these systems after transferring the nanopatterned thin films to thin membranes. Combining the gathered data with micromagnetic simulations provided by Andreas Hütten allowed the formulation of a sound hypothesis on the interplay of different magnetic interactions.
Each topic in this thesis has a similar structure with a separate introduction, theoretical background, experimental methods, a discussion of the results, and a conclusion. While the individual topics differ greatly, they are connected through the experimental methods, namely the dual beam microscope and electron beam lithography. Therefore, the next chapter will provide a thorough introduction to these common methods. The final 'conclusion and outlook' section briefly summarizes the results and puts them into the broader context of the future perspective for nanofabrication methods in different fields. A detailed summary related to the specific experimental results is found in the summary section of each chapter.

2 Nanofabrication methods

2.1 Lithography

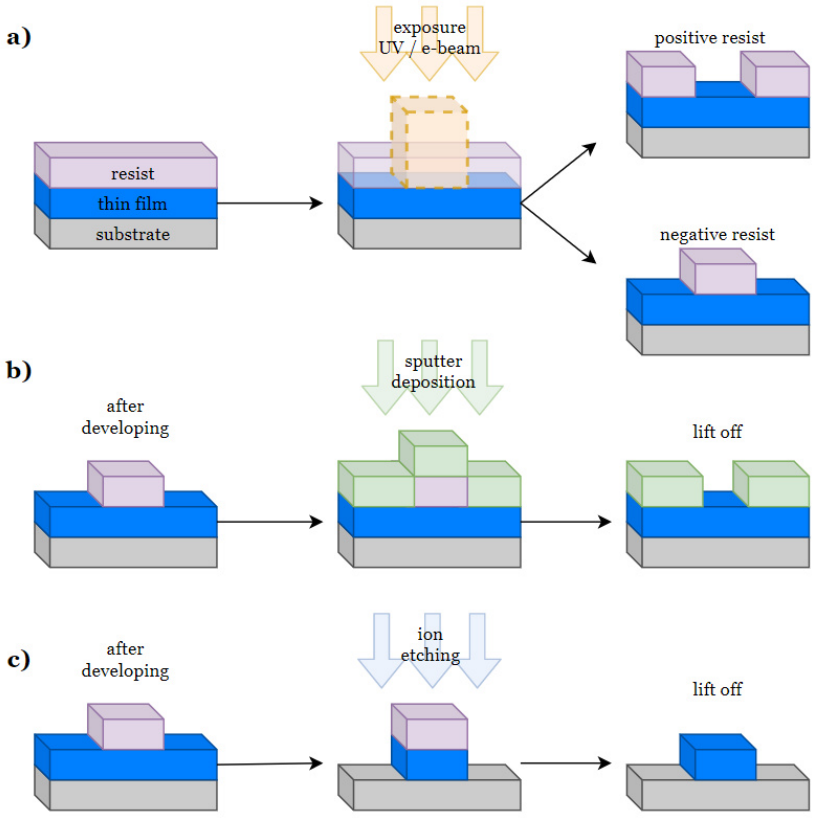

Figure 2.1: Schematic sketch of a basic lithography process: a) resist application, exposure, and development. A positive resist leaves the exposed area open while a negative resist only covers the exposed area. b) deposition of additional layers after resist application and development c) ion etching to remove parts of previously deposited thin films.

A large part of this work is dedicated to the application of nanofabrication methods like lithography and dual beam techniques involving a FIB to create highly ordered structures and explore the unique properties of nanopatterned materials. In particular, most lithography processes were developed and executed on a LEO 1530 SEM, equipped with a highly precise laser interferometer stage, which is an older model of the Gemini-SEM product family by Zeiss. At the typical acceleration voltage of 20 kV, an imaging resolution limit of roughly 1.5 nm can be achieved[1]. In general, many different lithography techniques exist that share the same basic principle in order to create patterned surfaces on different length scales.
All lithography processes share the basic steps of resist application, exposure, and development before the exposed pattern is used as a template to build upon the underlying sample. The key components to determine the resolution limit of the pattern are the choice of resist and the method of exposure. Typical resists consist of photosensitive polymers or epoxy compounds that change their mechanical prop-

erties upon irradiation with UV light or electrons, leading to the broad classification of either e-beam or UV lithography. Within each category, resists can be further differentiated into positive resists that soften when exposed and negative resists that harden during exposure, which is illustrated in Fig.2.1 a).
That means that depending on the resist type inverted structures can be created after developing the resist by using the same irradiation pattern or photomask. The patterned and developed resist can subsequently be used as either a deposition mask to build structured thin films or an etching mask to selectively remove previously deposited material, as illustrated in Fig.2.1 b) and c). While chemical etching is possible, Argon ion etching is commonly used for small structures in thin films, due to precise control of the etch depth with secondary ion mass spectrometry (SIMS). After the process the resist can be removed with an organic solvent like acetone or N-methyl-2-pyrrolidone.
Due to the diffraction limit e-beam lithography has a significantly lower resolution limit than UV lithography, which is almost exclusively used for large structures like contact pads or conducting wires on chips or circuit boards. With the ever-increasing demand for more powerful computation devices, the desire to shrink electronic circuits and sensors is always growing. Vieu *et. al.* report a lower limit of 10 nm for isolated features and a pitch distance (center to center) of 30 nm for arrays of pillars in a laboratory setting with a conventional polymethylmethacrylate (PMMA) e-beam resist [2]. In fact, instead of the resolution of the exposing electron beam, the limiting factors are the resist itself and the development process. For example on edges or in recesses of the hardened resist, excess material can remain and broaden the resulting structure, which can be solved for example by ultrasonic agitation during development.
Additionally, the thickness or more accurately the aspect ratio of the developed structures plays a large role in the final resolution. Generally speaking, if the resist is used as a sputtering mask for a thin film, the resist needs to be significantly thicker than the deposited layer to be easily removable by the solvent during lift off. Conversely, extremely fine patterns can not be exposed in a thick resist layer, because tall, narrow structures become mechanically unstable, much like trying to balance a pencil on its tip. This imposes an upper limit on the deposited layer thickness if maximum lateral resolution is desired. The specific process parameters used in this work will be described in detail in the appropriate chapters. For a more detailed description of lithography processes in general, please refer to [3].

2.2 Dual beam microscopes

The second major nanopatterning technique explored in this work is the dual beam microscope, namely the Helios NanoLab 600i (Thermo Fisher Scientific, FEI) [4]. The machine combines a scanning electron microscope (SEM) and a focused ion beam microscope (FIB) with a single vacuum chamber to have the sample accessible to both beam modes. This alleviates the main disadvantage of conventional focused ion beam microscopes, which is their imaging capabilities. Due to the high kinetic energy of the ions on impact, high-resolution imaging quickly damages a sample's surface. In a dual beam system, the electron beam can be used to create high resolution images of the sample surface, while the ion beam can be used exclusively for high resolution milling. Additionally, a dual beam microscope offers applications that would be impossible to achieve with the individual devices by quickly alternating between both beam modes. This can be used for example in tomography [5].

Both columns in the dual beam system use in essence the same sources and accelerator columns as the respective single beam devices. One column is attached to the vacuum chamber at an angle and aligned so that both beams share a coincidence point at the so-called 'eucentric height'. Commonly the ion source is at a 45° to 52° angle to the electron column and the eucentric height lies a few millimeters away from the tip of the column. Working at the coincidence point allows for precise ion milling of the sample and simultaneous high resolution imaging of the same area with the SEM. A motorized stage is used to drive the sample to the coincidence point as well as to rotate and tilt the sample so that either beam is perpendicular to the substrate surface. This is illustrated in Fig. 2.2 with the dashed lines representing the plane perpendicular to the respective particle beam. Typical machines use step motors and gearboxes to precisely move the sample on five axes: x, y, z, rotation and tilt.

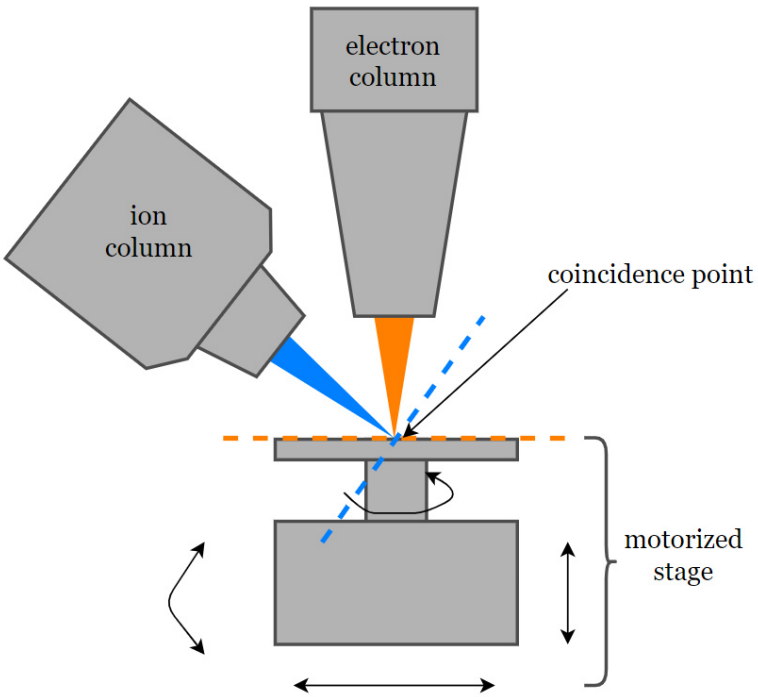

Figure 2.2: Sketch of a basic dual beam microscope. A motorized stage is used to move the specimen to the coincidence point where both beams overlap to allow milling and imaging at the same point. The stage can move in x, y and z, as well as rotate, and tilt.

2.2.1 Scanning electron microscope

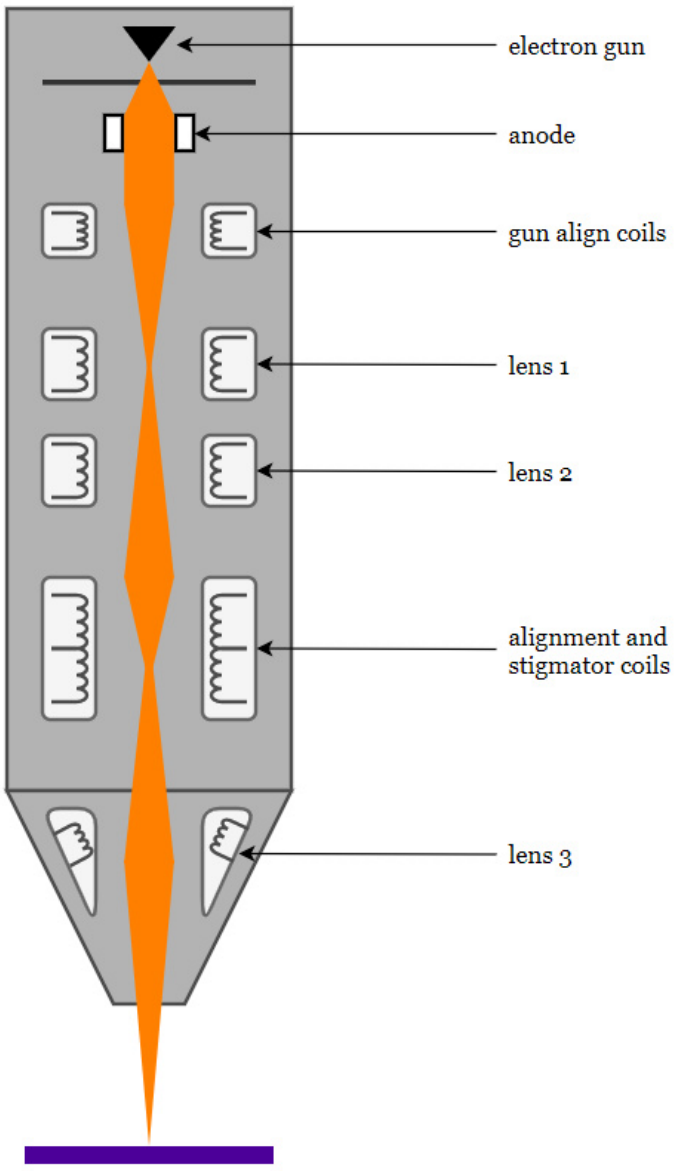

Figure 2.3: Schematic overview of a scanning electron microscope column.

A scanning electron microscope uses a highly focused electron beam to scan across the sample surface and generate an image. Free electrons generated in the gun are accelerated toward the sample leading to various interactions. These signals that contain information about the surface topology and chemistry are picked up by different detectors in the machine and matched to their respective beam position in order to generate an image. A typical scanning electron column consists of an electron gun, several electromagnetic lenses, alignment and scanning coils, and in some cases an additional so-called immersion lens. A sketch of a scanning electron microscope column can be seen in Fig. 2.3.
The electron gun produces free electrons which are accelerated toward the anode

to create the electron beam. In the Helios NanoLab 600i a Schottky thermal field emitter is used, but other gun designs exist as well [4, 6]. A field emitter electron gun (FEG) uses the field emission effect where electrons can leave a material surface if the electric field surpasses the work function of the surface, which is determined by the material and the surface properties. In thermally assisted field emission, a sharp tungsten tip is heated to near melting temperature and a strong electric field of multiple kV is applied to increase the electron yield. Additionally, the tip is coated with zirconium oxide (ZrO), which further decreases the work function of the tip.
The beam is focused by electromagnetic lenses, which consist of several coils to generate a magnetic field. By adjusting the lens current, the magnetic field and therefore the refractive power of the lens can be changed. The scanning and stigmator coils are used to alter the beam path in a way so that the sample surface can be scanned. Similar to old Braun's tube TVs a sawtooth pattern can be used to create the scanning beam motion. Stigmation coils are used to adjust the beam path through the lenses and are equally important as the focal length to obtain a sharp image.
In general, both the size of the focal point as well as the interaction volume of the electron beam depend on the acceleration voltage. While the beam resolution is finer at high acceleration voltages (1.0 nm at 15kV compared to 2.5 nm at 1kV [4]) the penetration depth of the beam and therefore the interaction volume also increases, making the SEM less surface sensitive at higher voltages. To counteract this, different approaches have been realized. Recently, machines can apply a negative bias to the stage to decelerate the beam while still maintaining a sharp focus point at landing voltages as low as 200 V leading to high surface sensitivity [7]. The Helios Nanolab 600i instead uses an additional immersion lens to decrease focus size and achieve a higher image resolution even at low acceleration voltages. This lens is placed at the tip of the gun and has pole shoes that immerse the normally field free sample region in a magnetic field. In order to optimally use this feature, additional alignment steps of the lenses to one another and concerning the source tilt are necessary.
The most common detector used for imaging with both beams is the secondary electron (SE) detector. Secondary electrons are generated when a high-energy particle (electron or ion) hits a material and ionizes an atom. A single high-energy particle can generate several secondary electrons. Since only secondary electrons from a certain depth can leave the sample and reach the detector, edges normally appear brighter as a larger fraction of the interaction volume is close to a surface area. A common type of secondary electron detector is the Everhardt-Thornley detector (ETD). It consists of a scintillator and photo multiplier covered by a faraday cage. The cage is kept on a positive bias of roughly 50V to attract low-energy secondary electrons. Inside the detector, the electrons are accelerated toward the scintillator by a voltage of several kV and produce light, which in turn is converted back into an (amplified) electron current by the photomultiplier cathode [8]. Secondary electron detectors can be placed inside the electron column as a through-the-lens (TLD) detector or outside the column in the vacuum chamber.
Most microscopes are additionally equipped with a backscattered electron (BSE) detector. These electrons are primary beam electrons that are elastically scattered by atomic cores in the sample. Since heavy atoms have a higher scattering cross section, they reflect more electrons and appear brighter in the resulting micrographs. This results in backscattered electron images having an element specific contrast.

However, the backscattered electron signal is typically much smaller than the secondary electron signal leading to longer image acquisition times.
Additionally, the Helios Nanolab 600i is equipped with an energy-resolved X-ray detector. Besides secondary electrons a high energy electron beam can also generate X-rays from the sample through deceleration and ionization, leading to element specific signals. This technique is called energy-dispersive X-ray spectroscopy (EDX/EDS) and is used to either collect spectra for composition analysis or element specific maps of the sample surface by matching the X-ray signal to the position of the scanning electron beam. EDS is a powerful tool to investigate nano-objects and can also be used in other microscope types like the transmission electron microscope (TEM) [6].

2.2.2 Focused ion beam

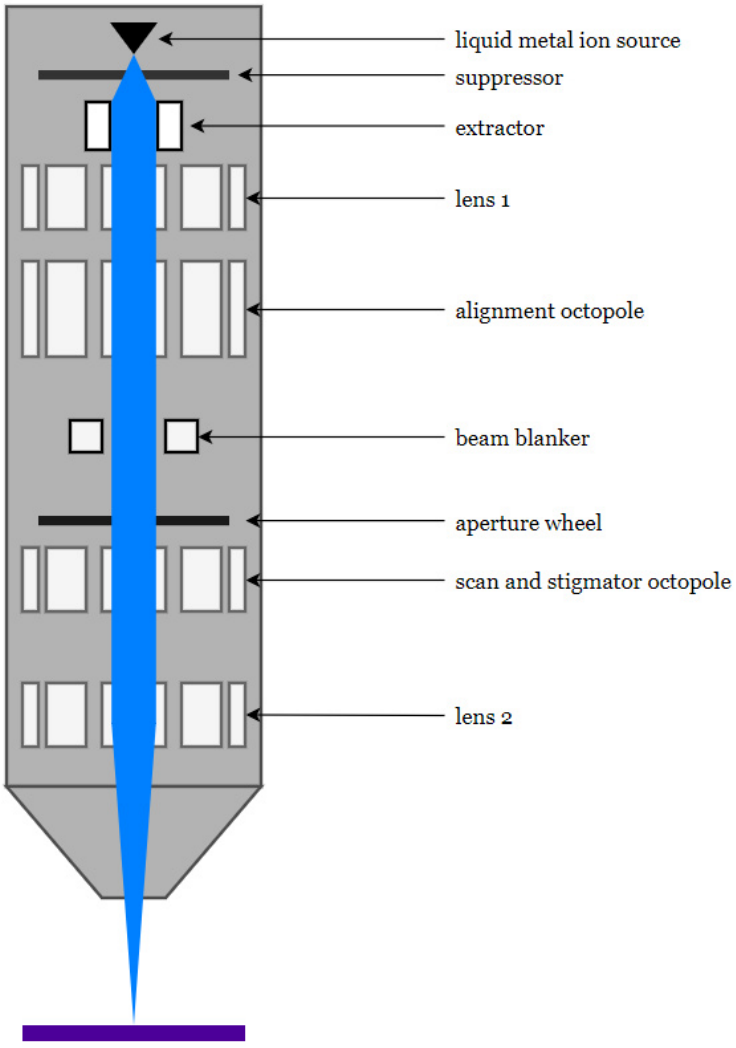

Figure 2.4: Schematic overview of a focused ion beam column.

Focused ion beam microscopes (FIB) utilize the same basic principle as scanning electron microscopes, where a focused beam of accelerated particles is used to scan the sample surface. Instead of electrons, different kinds of ions are used. Since ions are orders of magnitude heavier than electrons, they can modify the sample and sputter surface atoms. For simple imaging applications, this is undesirable, as the fundamental resolution limit depends on the competition between the sputter rate and the rate at which information (i.e. the secondary electron signal) can be acquired. The sputtering rate depends on both the primary ion species of the beam and the sputtering sensitivity of the sample. If all material parameters are known, the resolution limit can be calculated according to the considerations of Orloff *et. al.*, however in most cases the FIB will be used in a dual beam system where the imaging is done by the electron column [9]. On the other hand, the FIB can be used to precisely and selectively remove material. Most commonly, milling is used to create supporting features for other analytical or imaging applications such as cross

sections or TEM lamellae, that would be normally inaccessible to the electron beam or very tedious to produce by other means.
Newer dual beam systems use liquid metal ion sources (LMIS), as heavier atoms are more useful for milling applications. For imaging, helium ion sources are popular. The most common material used in liquid metal ion sources is gallium, since it has a low melting point and therefore does not need a lot of heating power to stay in the liquid phase. Gallium ions are heavy enough to mill most materials, while not instantly destroying softer materials. The low vapor pressure simplifies source construction. In essence, the concept of LMIS is similar to the Schottky field emitter electron gun. A tungsten tip is attached to a heated Ga reservoir. The extraction voltage of several kV between the tip and the extractor is high enough to evaporate and ionize gallium atoms at the tip and the evaporated atoms are constantly replaced by a flow of liquid gallium from the reservoir. At the tip, a combination of surface tension and electrostatic forces shapes the liquid metal to a sharp so-called 'Taylor cone' with an apex diameter of roughly 5 nm [10]. Typical emission currents are in the order of a few μA. Additional apertures and the suppressor can further reduce the ion current. Unlike electron optics, ion columns use almost exclusively electrostatic lenses in the form of octopoles, since the heavier particles require stronger fields to focus effectively. Lorentz-forces in a magnetic field are directly proportional to the particle velocity since $\boldsymbol{F} = q\boldsymbol{v} \times \boldsymbol{B}$. However, Coulomb forces are independent of the particles' velocity. This is important as a heavier particle will be only 0.0028 times as fast as an electron accelerated by the same potential, whereas it carries 370 times their momentum [10]. Similar to electron and light optics, concerns like aberrations and stigmatism also apply to ion optics, making the microscope controls very similar. Figure 2.4 shows a sketch of an ion column.
In the Helios NanoLab 600i an aperture dial with 15 different drill holes is used to adjust the ion current for the respective application. For milling, the typical acceleration voltage is 30 kV. However, when ion implantation or amorphization of the sample surface is of concern, the acceleration voltage can be reduced to 5 kV. At 5 kV the image quality is relatively poor and the beam shape is highly susceptible to stigmatism.

The following apertures see most frequent use:

9.7 pA	A low current with a small beam diameter used for imaging and high-resolution milling. Unless used at high magnifications, this setting is not damaging to most sample surfaces. An even lower current of 1.5 pA is available. However, because of poor image quality due to lack of signal, it is not commonly used.
28 pA	This setting can also be used for imaging at low magnification. Additionally, it is most commonly used in TEM lamella fabrication to deposit a protective Pt layer since it offers a high deposition yield. For details refer to chapter 2.2.3.
0.28 nA	A setting commonly used for high yield, yet reasonably precise milling, polishing, and cleaning cross sections.
2.8 nA	The most common setting for high yield milling. It is used for rough cuts and large cross sections, and can damage surrounding areas.
21 nA	The highest current available is rarely used, except for rough cutting on a large scale. The destructive potential is high when used for imaging.

For all apertures the beam's intensity profile can be approximated by a double Gaussian and a double exponential tail distribution [11]. The absolute beam radius depends on acceleration voltage and aperture, but for each setting the tail extends roughly three times as far as the central region, which needs to be considered during milling. Even when milling straight down, the resulting feature will always have a certain angle due to the beam's intensity profile. Similarly, a dense array for milled features will result in potential damages to the features due to the exponential tail of the beam profile. This needs to be considered especially for thin film samples, as damage to the surface can result in a loss of functionality of the device.

2.2.3 Gas injection systems

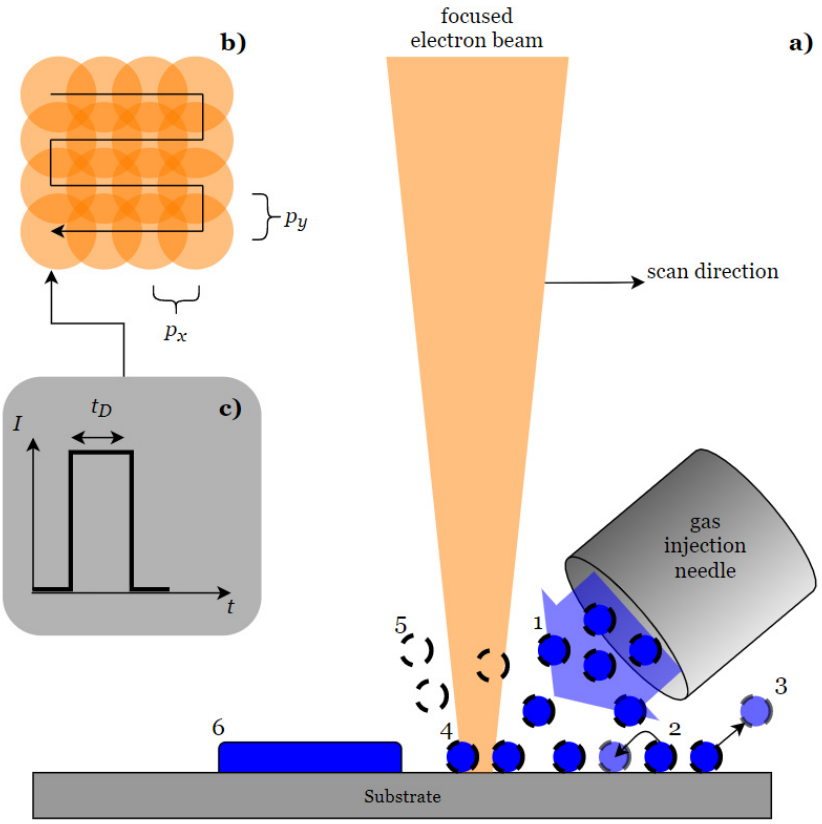

Figure 2.5: a) Sketch of the FEBID-process: (1) precursor molecules are evaporated inside the gas injection needle and injected close to the substrate surface where they physisorb. On the substrate surface these molecules either diffuse (2) or desorb (3). Physisorbed molecules that are hit by the focused electron beam or resulting secondary electrons (4) are dissociated into the metallic component (blue) and the volatile organic ligands that either desorb from the surface (5) or are incorporated into the deposited material (6). b) The desired pattern is split into pixels of point exposures with a pitch distance p_x and p_y between points. These points are scanned with a meandering beam path multiple times (loops). c) At each pixel the beam remains for a dwell time of t_D before moving to the next pixel.

Gas injection systems (GIS) are a common feature of dual beam microscopes and are based on a principle similar to atomic layer deposition (ALD), where adsorbed precursor molecules are dissociated by a current pulse to form an even thin film. While the used precursor molecules are often identical, the dissociation process in a dual beam microscope is initiated by electron or ion irradiation and therefore offers highly localized deposition. The most common application for this technique is the deposition of a protective layer to prevent surface damage during TEM lamella preparation. However, due to the process' flexibility, other applications for sample preparation like fast prototyping are available. Depending on the kind of particle used for activation, the deposition process is called focused electron beam induced

deposition (FEBID) or focused ion beam induced deposition (FIBID).
The general mechanism of FEBID is illustrated in Figure 2.5. A heated reservoir inside the gas injection column evaporates the precursor molecule at a set temperature for the respective precursor to build up pressure without destroying all of the precursor material inside the needle. The needle is brought close to the substrate surface in the order of a few microns before opening the valve and releasing the precursor molecule into the vacuum chamber. During this process, the pressure in the vacuum chamber rises by roughly one order of magnitude. Through Van-der-Waals forces (or other interactions depending on precursor and substrate) the organic molecules that typically contain metal atoms can adsorb to the sample surface. After adsorption, the precursor can either diffuse along the surface or desorb due to its vapor pressure. Because of the precursor molecules' metastable nature, the molecule dissociates when hit by the electron beam of the microscope. Ideally, the metal atoms stay behind on the substrate surface, while the hydrocarbon residues evaporate. Since the dissociation process is mostly triggered by low-energy electrons, i.e. by secondary electrons or backscattered electrons, the deposited structure can be wider than the actual beam diameter [12, 13]. In most cases, part of the carbon residue is incorporated into the material, giving FEBID/FIBID layers different properties than pure metal thin films prepared by sputter deposition.
A commonly used precursor for protective coatings and precise electrical contacts is trimethyl-cyclopentadienyl-platinum ($Me_3CpMePt(IV)$), which will from now on be refered to simply as Pt-precursor. It has a comparatively high deposition rate and can be stored in a vacuum at room temperature for a long time without degrading. Other available precursors include $Co_2(CO)_8$ and $Fe(CO)_5$ for magnetic materials as well as Gold, Tungsten, Silver, or Lead precursors for other metals [14]. Alloys like CoFe can be deposited by combining multiple gas injection systems or by using exotic alloy precursors [14].
To deposit larger structures, the desired shape is broken down to individual pixels with a pitch distance p_x and p_y, which are scanned in a meandering pattern by the electron beam. Each pixel is exposed by an electron pulse of the length $t_D$which is called dwell time. An illustration for this is found in Figure 2.5b) and c). The total number of pixels in a structure multiplied by the dwell time gives the so-called loop time t_L, which is the time needed for the electron beam to come back to a pixel that was already exposed. In order to build up enough material, sometimes several thousand passes of the electron beam are needed. t_L is a critical quantity for FEBID, because unlike sputter deposition, the precursor needs some time to re-adsorb to the surface after exposure to the electron beam. Similarly, extending t_D will not always lead to more deposition, since after some time all available molecules in a pixel are dissociated. This mechanism is thoroughly explored in chapters 4.2.1 and 4.2.2.
In some cases, it is possible to pre-condition the sample surface by electron beam irradiation, which activates the surface to auto-dissociate the precursor that is injected afterward [15]. Furthermore, different concepts of post-deposition purification have been introduced to remove residue impurities of the precursor molecule. Depending on the deposited material additional electron irradiation or exposure to different plasmas like H_2 and O_2 have been demonstrated to increase the metal content dramatically [16, 17, 18]. Ultimately, FEBID is limited by the availability of suitable precursor molecules, so further developing the technique is an interdisciplinary effort. However, many interesting applications and discoveries around FEBID materials have been made recently. This includes the deposition of polycrys-

talline ferromagnets as well as nano-granular strain sensors by exploiting the carbon residue in the material as tunnel barrier [19, 20]. More exotic applications include superconducting FEBID structures [21].

2.2.4 Direct-write lithography

A dual beam system offers a unique kind of lithography process, that does not need a resist like the conventional lithography process described in chapter 2.1. Whereas usually a resist mask would be needed to deposit or selectively mill a structure on a substrate, the dual beam system can do both in situ. The gas injection system described in the previous section can selectively deposit a limited selection of materials to for example form conductive channels. In contrast, the ion beam can be used to selectively mill material with high precision to create free-standing structures, like plasmonic Au particles or even complex shapes like bow ties, that would be hard to create with a resist mask [22, 5]. Additionally, accidental surface passivation or corrosion by any of the involved chemicals in resist-based lithography is completely avoided, offering unique possibilities in the dual beam system. Through simulation based beam control software, even free form 3D nanoprinting is possible with direct-write lithography [23, 24, 25]. This impressive technique, however, is limited by its deposition speed and low yield.

2.2.5 Helios Nanolab 600i

The Helios Nanolab 600i uses a 5 axes motorized stage, with a movement range of 150mm in the xy-direction and 10mm in the z-direction. Tilting the sample up to 60° toward the ion beam or 10° away from the ion beam is possible with an accuracy of 0.1° in the range of 50-54°. A tilt of 52° is perpendicular to the ion beam. The stage move repeatability in the xy-plane is roughly 1 μm, however, smaller move distances are possible. Stage movement is supported by the "compucentric rotation" feature, that centers the rotation and tilt axes on the center of the field of view independent of the actual motor position with reasonable accuracy.
In addition to the imaging column, the Helios is equipped with an ultra-fine etched needle by Omniprobe, which can be used to physically manipulate samples for example during TEM lamella fabrication. Furthermore, a total of three gas injection systems are available. Two of which are equipped with a Pt-precursor and a Si-based insulator. For the purpose of this work, the third GIS was filled with the Co-precursor $Co_2(CO)_8$, which has a high vapor pressure and auto-dissociates slightly above room temperature. Since this precursor is not part of the pre-installed material database, the otherwise unused software preset SCE (saturated calomel electrode, a mercury compound) was used for Co-deposition. Hence, the Co deposition parameters needed to be carefully tested and calibrated. The storage chamber in the GIS was heated to 25 °C, which is slightly above room temperature, since the precursor molecule is fragile [26]. Due to mechanical and software constraints, it is not possible to deposit from two gas injection systems simultaneously in this machine. To automate part of the deposition and milling process, the tools AutoFIB and RunScript are available.

3 Scripting - Automation of complex structures with the dual beam FIB

Due to a dual beam microscope's inherent flexibility in imaging and structuring samples, it is a highly sought-after tool for both quality control and small-scale prototyping. For that purpose, the automation and serialization of basic applications is desirable. The microscope control software for the Helios Nanolab 600i contains some predefined automation routines like cutting or polishing cross sections. However, most settings like defining complex structuring features, setting the correct beam parameters, and starting the milling process still require manual input. These basic features alone are not sufficient to support prototyping on a higher level or to efficiently produce a small series of similar samples without a considerable time investment of the operator.
Without an automation environment, dual beam microscopes lack the ability to reliably recreate copies of complicated structures. Some applications like the aforementioned routines for cross sections are used in TEM lamella preparation, which is one of the core uses of dual beam systems. They are based on an underlying scripting language, that essentially mimics a manual button press or change of settings. This scripting language provides access to many machine variables like beam parameters and offers good control of the patterning engine. While parts of it resemble commonly used programming languages, the scripting language of the Helios NanoLab 600i is a proprietary system language, that does not use an external compiler. Through the use of scripts, multiple iterations of a prototyping process are easy to track. Furthermore, a structure created by a script can be analyzed and the script can be altered based on the findings to improve the device. This workflow is essential for all kinds of lithography processes, be it resist-based or a direct-write approach. It is comparable to automatic image stitching routines used during large exposures. In a dual beam microscope, the entire prototyping and testing process can take place in a single machine without breaking vacuum. This reduces the process development time significantly. The following sections will outline the properties of the RunScript tool for the Helios NanoLab.

3.1 Basic commands and script structure

Scripts for the RunScript tool are stored as regular text files with specific file extensions so that the tool recognizes them as such. These file extensions provide no functionality and are just used for recognition and organization within the program. Processing and control scripts use the .psc file extension. Within a .psc parent script, several sub scripts with the .sps extension can by run by the "run *scriptfile.sps*" command. This can help to organize complex processes that consist of several smaller steps which are repeated a lot. The scripting language provides access to all basic machine functions. This includes all five stage axes, the gas injection system, beam currents, and accelerator voltages for both columns, and many patterning commands. Complex applications can be created using arithmetic functions and loops. In contrast to popular programming languages like Java or Python, the scripting environment on the Helios NanoLab does not use closed loops (e.g. for i<10{do...}), but instead uses waypoints. A waypoint is marked by a colon and is referenced using the "goto *waypoint*" command. This poses some unique challenges to ensure no infinite cycles are created in a script. To add documentation to a script, any line can be turned into a comment by starting it with the "#" character.

```
#------------------------------------------------------------
#clear previous milling pattern
clear

#select material
#number is depth in microns, SCE indicates beam mode, in this case Co-precursor
setpatinfo 50, SCE


#define milling pattern loop variables
#x and y dist use microns for pattern separation, r can be used as auxiliary variable depending on shape

#important note: pattern creation uses absolute coordinates.
# depending on magnification a shift is needed to centralize the pattern

xdist=0.500
ydist=0.500
r=0.050


#initialize counting variable and set maximum, in this case a 10 by 10 square
m=0
mmax=10
nmax=10


#by jumping back to a certain point in the script, everything below that point will be
# executed again unless there is another command to jump back

#choose one of the pattern shapes below, adjust variables and set the others as comment

loop2:
n=0
loop1:

circle (n*xdist),(m*ydist), 0, r
#box (n*xdist),(m*ydist),((n*xdist)+r),((m*ydist)-r)
#line (n*xdist),(m*ydist),((n*xdist)+r),(m*ydist)
#obox (n*xdist),(m*ydist),((n*xdist)+r),((m*ydist)-r)

n=n+1
if (n<nmax) goto loop1
m=m+1
if (m<mmax) goto loop2


#------------------------------------------------------------
#Pattern is created, move stage and mill
endScript:
```

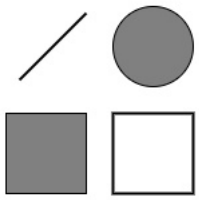

Figure 3.1: A script to create a grid of basic shapes on the screen. Independent counting loops and distance variables are used to create cubic or rectangular grids. In this case, all but the circle shape are commented out with the "#" symbol, so only circles are drawn. On the right side examples of the basic shapes are shown.

To change global machine variables, set commands are used. These can change beam current, accelerator voltage and stage position, and more. For example "setpatinfo 50, SCE" chooses the SCE application with a height of 50 μm for any patterning structures created after the command. Since SCE in this case refers to the Co source, the z-value is just an arbitrary number, as the software was not calibrated with the Co precursor in mind. Figure 3.1 shows a short script that can be used to create an array of basic shapes on the screen. Variables for distances and counting can be named freely with the exception of the coordinate axes x, y and z. These variables

are automatically assigned to the stage positions. In this example, a 10 by 10 grid of circles with a radius of 50 nm and a spacing of 500 nm is created. The counting variables for x and y positions are named “n” and “m” respectively. In general, the default unit of measurement for patterning commands is microns. Two interwoven loops are used to create the grid. The other available basic shapes “line”, “box” and “obox” (for a hollow box) are commented out. All shapes are illustrated on the right hand side of the code and are not part of the actual script. It is worth noting that any series of mathematical operations needs to be put in brackets or the software will not recognize it correctly. For the patterning engine, the origin point of the coordinate system is always in the respective image’s center. In order to center the pattern in the image, an offset needs to be considered. In this example the “mill” command to start the patterning is not included in the script, so it is possible to move the created pattern manually before milling. All patterns can be removed with the “clear” command.
To create exceptionally large structures, it can be necessary to move the stage after each individual milling process. This so-called stitching is also used in large-scale lithography where the write field is limited by the maximum beam deflection. Figure 3.2 shows part of such a stitching script that mills a 4 by 1 grid of any predefined pattern. This can be used to duplicate several instances of the 10 by 10 circle grid from Figure 3.1 for example. For patterns consisting of many smaller structures, stitching is necessary as the software has difficulties handling more than roughly 250 individual shapes due to insufficient cache memory. Because of the higher number of vertices, round shapes take up a lot more memory than simple rectangles or lines. While the basic structure of the stitching script uses loops and waypoints very similar to the one that sets the pattern, a few things need to be considered when stage movement is concerned. Unlike the patterning coordinate system, which is always centered on the current image, the stage uses absolute coordinates respective to the maximum and minimum motor position. It is therefore very important to set a new stage coordinate system by capturing the current absolute position with “getstagepos” and saving the result in new variables. All movements can then be given relative to this reference point. Furthermore the stage movement is measured in millimeters, so appropriately assigning pattern and movement variables requires extra care.
The script is designed to mill the sequence of write fields in a meandering pattern, always starting with movement to the right. In order to catch the exceptions that either of the “millmax” variables is 1, the script uses four loops instead of two like the patterning script. “loopRight” and “loopLeft” move the stage right and left respectively. For the downward move (y-direction), the routine was split into “movedownR” and “movedownL” depending on which horizontal movement pattern was performed last. Without this arrangement, offsets along the x-axis would occur. The “sleep” command pauses the script execution for a given number of milliseconds, as the RunScript tool does not wait for stage movements to finish by default. As no pattern is defined in the given example, the “mill” command will execute any pattern that is currently defined on screen without changing the application or the parameters. This means, that this stitching script can be used for both deposition and milling. For milling the “Si” application is used, where the z-depth is calibrated on a pure Si wafer. The deposition applications are “Pt e-dep” and “Pt dep” for platinum deposition with the electron and ion beam, respectively. As stated in the previous chapter, the SCE application preset was used for the Co-precursor, so the saved calibrations for this application are not used.

```
#-------------------------------------------------------------

#Pattern is created, move stage and mill

#initialize new variables, stageshift is in mm, so this shifts by 10 microns
millnmax=4
millmmax=1
nxc=0
nyc=0
stageshift=0.01

#read stage position to define relative coordinates
getstagepos
xnew=x
ynew=y

#start with first milling in top left corner
loopYmove:

mill
sleep 2000

nxc=1
#move to the right

loopRight:
if (nxc=millnmax) goto movedownR
xnew=xnew+stageshift

#move and mill (stagemove command uses absolute position)
stagemove x, xnew
sleep 2000

mill
sleep 2000

nxc=nxc+1
#counter is set up so that the number millnmax will be the number of patterns milled
if (nxc<millnmax) goto loopRight

movedownR:
#move down

ynew=ynew-stageshift
stagemove y, ynew
sleep 2000
nyc=nyc+1
if (nyc=millmmax) goto end
```

Figure 3.2: Part of a longer script to stitch together multiple milled patterns in a rectangular grid following a meandering pattern. The pattern has to be set by hand or by a different script. Independent counting variables are used for the x and y coordinates. Waypoints are used for movements to the right, left and down. Downward movement distinguishes between coming from the left or right since problems can occur when either of the counting limits “millnmax” or “millmmax” is set as 1.

When the gas injection needle is inserted, stage movement is restricted by interlocks, to not damage any components by accidentally driving the stage into them. To deposit extended structures with a stitching script, the GIS needs to be inserted and retracted for each deposition step. The commands in Figure 3.3 can be used to replace the simple "mill" command from the script in Fig. 3.2. "Insertbyname" and "retractbyname" can be used to insert and retract specific gas injection needles for the desired application. Since the script does not wait for the needle movement to finish by itself before starting the deposition, several "sleep" commands were added to make sure the needle has reached its final position before continuing the script. In the Helios NanoLab 600i, the movement of the GIS needles, as well as all valves, are controlled by pneumatic valves. This means that needle movement is comparatively slow, and long waiting times are needed.

```
insertbyname Pt dep
sleep 8000
mill
sleep 2000
retractbyname Pt dep
sleep 8000
```

Figure 3.3: A short script to deposit a Pt pattern. Waiting times are added to wait for needle movement to finish before starting deposition.

3.2 Software limits and fine tuning of gas deposition

Besides the examples given in the above section, other commands are also available. Similar to “setpatinfo”, additional beam parameters are accessible through scripts. In Figure 3.4 these commands are illustrated and could be used in any script header. “setpatbeam” expects either a ’0’ or a ’1’ as an argument, setting the ion or electron beam respectively. Similarly, “setparallel” mode expects either a ’1’ for “true” or a ’0’ for “false”. The parallel milling mode combines all on-screen patterns so that a loop does one pass over each pattern before coming back around. The default milling mode is “serial”, which finishes a complete pattern before moving on to the next. With “sethv”, “setmag”, and “setaperture”, the acceleration voltage, image magnification, and the beam current can be controlled. Since the apertures are just incrementally numbered, using the script command can feel clumsy compared to setting the beam parameters manually before running the script. Other commands that were not used in this work include “grabframe” for saving images automatically, “match” to compare the current image to an already saved image and identify features, and all commands involving detector settings. Usually, the imaging is manually optimized before any scripts are run to ensure the best possible quality. Especially during milling the focus and stigmator settings can impact the resulting pattern dramatically.

```
#Beam Parameters
#(not necessary here, manual settings will not be changed)

setpatbeam 1
sethv 30
#setaperture 3
#setmag 5000
#setparallelmode 1
# for serial milling change to 0
```

Figure 3.4: List of commands to change beam parameters within a script.

Some parameters like dwell time, the total number of loops, pitch distance, or rotation of a pattern are not accessible from a script. Since these values are critical to optimize the gas deposition process, most scripts were split into a drawing routine for the patterns and a milling routine that handles the actual deposition. After the first script had finished, one can manually select and adjust the pattern parameters like dwell time or pitch distance before starting the deposition process. Additionally, the application, i.e. “Si”, “Pt dep” or “SCE”, can only be changed manually after the pattern is drawn. In order to change the application in a script, the entire structure would need to be redrawn.
When deposition from different gas injection systems in the same structure is desired, a few additional considerations are necessary. Each needle is inserted from a different angle respective to the sample surface and carries its own electrostatic potential. This is usually a minor issue during imaging and focus or astigmatism rarely need to be adjusted when a needle is inserted. However, it leads to a slight offset in the deposited pattern. Hence, even though the same pattern is used with a different application and the stage has not been moved, the pattern needs to be adjusted manually, if an overlapping structure is desired. This is increasingly dif-

ficult the smaller the patterns become, as the offset is not always the same and thus can not be programmed into the script. Despite these limitations, the automation of patterning processes is an essential tool for creating highly ordered periodic structures. The methods described in this chapter can be used for any repeating patterning application in the FIB. A full set of commands and instructions can be found in the Helios Nanolab 600i user manual and the AutoScript technical notes provided by Thermo Fisher Scientific/FEI [27, 28].

4 Direct-write approach to highly ordered granular GMR sensors

After its discovery in 1988 by Peter Grünberg and Albert Fert, the giant magnetoresistance effect (GMR) has gathered considerable attention for various sensor applications [29, 30]. As the first read head sensors in hard drives (HDD), magnetoresistive sensors continued to be a highly researched topic until present day. However, because of rapid developments in tunnel magnetoresistive devices (TMR) with a high signal-to-noise ratio, GMR read heads vanished from the HDD market. They only recently re-emerged with advances in half-metallic fully epitaxial GMR sensors that promise high effect strength, good conductivity, and low noise [31]. These new GMR devices are based on half-metallic Heusler alloys like $Co_2FeGa_{0.5}Ge_{0.5}$ (CFGG) and require careful preparation and heat treatment for optimal results [32, 33].
Besides these high-performance sensors in magnetic recording, GMR devices of simpler design are used in various industrial applications, for example as sensors in anti-lock break systems (ABS) in the automotive industry. Therefore, not only absolute magnetoresistance ratio but also ease of manufacturing, price, and durability are of concern when designing novel magnetoresistive sensors.
Most GMR devices are prepared from thin film structures using lithography. The preparation of thin films with high purity requires elaborate CVD or PVD (sputtering) systems in an ultra high vacuum (UHV) [34, 35]. Arrangements of magnetic nanoparticles, which are easy to manufacture in large quantities, should exhibit similar GMR properties to thin film systems but are not as widely explored, because a large part of the research surrounding magnetoresistive devices is centered around the magnetic recording industry.
Several research projects involving granular magnetoresistive devices have been conducted in recent years. In her dissertation, Inga Ennen investigated monolayers of Co-nanoparticles on a silicon substrate, coated with a thin Cu-layer to form a conducting matrix [36]. Since most nanoparticles have a non-conducting organic shell, the particles needed to be treated with forming gas (95% N_2, 5% H_2) in a vacuum oven to remove the shell. In that study [36], only a few percent GMR were measured since the preparation process might have damaged or oxidized the particles and therefore most of the measurement current was shunted through the Cu-matrix. In 2013, Meyer *et. al.* found high MR ratios of up to 260% in granular GMR devices using agarose gel as matrix material [37]. The magnetic particles could move inside the matrix and self-assemble into wires, providing preferred conduction paths through the matrix and leading to the high GMR. Due to the low conductivity of the gel matrices themselves, the measurements had to be performed using AC currents. This effectively prevents the accumulation of static charge as a result of ion movement, as the ions can not follow the alternating electric field. Additionally, the sensor had to be stored in closed compartments and the liquid part of the gel medium would eventually evaporate, leading to a very limited lifetime of the sensor [1]. Given this great, albeit slightly impractical, result, a theoretical model to describe magnetoresistive transport through nanoparticles was developed by Teich *et. al.* in 2015 [38] and further developed by Daniel Kappe in his dissertation [39].
This chapter will explain the basic idea behind these simulations and explore two approaches to an experimental realization of the simulated structures. The first is a bottom-up approach that uses ferromagnetic Co-particles created by focused electron beam induced deposition from a $Co_2(CO)_8$ precursor. A dense array of particles

is then coated with a weakly conducting material to form a matrix. This creates a 2D representation of the gel matrix samples on a wafer without the need for air-proof compartments or AC measurements. In the second approach, a Py thin film is used as the base material for a top-down preparation of highly ordered nano-discs using FIB milling. By creating narrow trenches in the thin film with the ion beam a grid of rectangular particles can be created. Experimenting with particle shape and size is particularly easy in this approach. Similar to the bottom-up method, the gaps between the particles are filled with a non-magnetic conducting material as the matrix. At the end of the chapter, the results from both approaches will be assessed and compared.

4.1 Theoretical background

4.1.1 Giant magnetoresistance

The fundamental reason for all magnetoresistive effects is the spin dependence of charge transport in materials. This is especially true for ferromagnetic materials. Band structure calculations show exchange splitting between spin-up and spin-down electron bands and therefore also a spin-dependent density of states. The resulting patterns can be very complex, but to understand the basic phenomenon, a qualitative model is sufficient. In the Stoner model, free electron bands exhibit exchange splitting, leading to a different density of states and electron velocity at the Fermi level for spin-up and spin-down electrons [40]. Additionally, spin-dependent scattering as a result of a shift in the density of states can be considered. If for example the *d*-band for the minority spin electrons is close to the Fermi level, the scattering rate toward those states is higher, because of the high number of available states. As a result of these factors a current passing through a ferromagnetic material is spin-polarized and will experience spin-dependent scattering. Figure 4.1a) and b) illustrate the two basic measurement concepts for GMR in a ferromagnetic multilayer system. For the current-in-plane (CIP) measurement geometry, which was historically the first to be discovered, the current flows along the layers of the structure. In this geometry, the GMR effect occurs as a finite size effect through spin-dependent scattering at the interfaces. Only if the non-magnetic spacer is thin enough, i.e. if the mean free path for elastic scattering is longer than the layer thickness, the electrons from one ferromagnetic layer can easily travel to the other, where spin-dependent scattering or reflection can occur. The total conductance of the film can be calculated using the Fuchs-Sondheimer theory as well as the Boltzmann equation for thin films and is rather complex [41, 40]. In total, the conductance is equivalent to the conductance of the individual layers corrected by an interface term, which is responsible for the GMR effect.
In contrast, the GMR effect in the current-perpendicular-to-plane (CPP) geometry can be explained using a more intuitive model. As a first approximation, the layers can be seen as a series of spin dependent resistors. This leads to two parallel currents, one for the spin-up channel and one for the spin-down channel. For an antiparallel configuration of the magnetic layers, the scattering is strong in both channels, which gives a high resistance. In either parallel configuration, as illustrated in Figure 4.1c), there is one low and one high resistance channel which results in a lower total resistance in the parallel circuit. Ideally, the layers are aligned antiparallel without an external field and parallel only when an external field is applied. In CPP geometry, the so-called spin diffusion length takes up the role of the mean free path from the

CIP geometry. The spin diffusion length describes the characteristic length of the spin polarization, i.e. the distance that the current can travel in the non-magnetic spacer without losing the spin polarization from the ferromagnetic layer. If the spacer is thicker than the spin diffusion length, less spin-dependent scattering at the interface will occur. With a mathematical model derived by Valet and Fert, the resistance change between the parallel and the antiparallel state can be calculated as

$$\Delta RA \propto \{\beta \rho_{\mathrm{FM}} t_{\mathrm{FM}} + \gamma R_b A\}^2. \tag{4.1}$$

In that formula A is the interface area, R_b the interface resistance, t_{FM} the thickness of the ferromagnetic layer, and ρ_{FM} is the resistivity of the ferromagnet. β and γ are the bulk spin asymmetry and the interfacial spin asymmetry respectively and represent the intrinsic material parameters for spin dependent scattering in the bulk and at the interface [42]. This theory can be extended to multilayer systems, where the formula becomes more complex. Even though the description for both geometries is different, the qualitative behavior of the GMR device in an external field will be mostly identical.

With some additions, the two channel series resistor model used to describe CPP

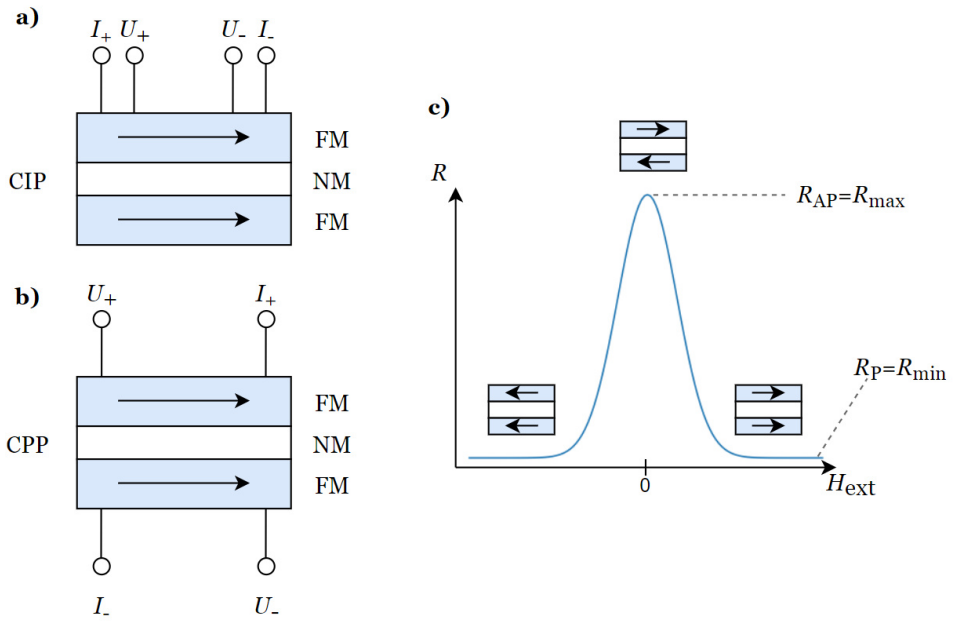

Figure 4.1: a) Sketch of a three-layer GMR system contacted in current-in-plane (CIP) geometry and b) in current-perpendicular-to-plane (CPP) geometry. c) A sample measurement curve of the resistance R of the GMR system as a function of the external field H_{ext}.

GMR can be adapted to describe granular systems. Figure 4.2a) shows a model system of two ferromagnetic nanoparticles indicated by grey boxes in a conducting matrix. Within each particle are two separate channels representing the majoritiy and minority spin electrons respectively. Similar to the model by Valet and Fert discussed earlier, each channel in a particle has a bulk resistivity $\rho_{\uparrow/\downarrow}$ and an interface resistance $r_{\uparrow/\downarrow}$ for each channel. Technically, the interface resistance depends on both the particle and the matrix, but for simplicity, the interface resistances in this model are attached to the particles. The non-magnetic conducting matrix resistivity

ρ_{NM} is spin-independent and represented by the green resistor between the particles. In this simple image, the resistors for the majority spin electrons are smaller, representing a lower resistivity. If both magnetic moments are aligned, the lower spin-up resistances $\rho_{\uparrow}$ and $r_{\uparrow}$ are connected in series. However, if the particles have alternating magnetic moments, a pair of low and high resistances each are connected in series. Given that the total resistance in a parallel circuit is $R_{\mathrm{tot}} = \sum 1/R_i$ for multiple conduction channels with a resistance of R_i, the configuration in Figure 4.2a) has a lower total resistance than the antiparallel configuration following the same model in Figure 4.2b). This description can be used for an arbitrary number of particles that form a chain.
In order to create a model that predicts real systems more accurately, a few additional considerations need to be made. For a CPP GMR device with only one magnetic domain and a defined easy magnetization axis, considering only the parallel and the antiparallel state is a valid description. While thin film systems can be structured into small pillars to achieve that, systems consisting of magnetic nanoparticles are harder to describe. The magnetization of adjacent particles can generally be at an arbitrary angle θ to one another. In such a case, there is a probability for a spin-up electron to become a spin-down electron and vice versa. The series resistor model can accommodate this by adding cross-connections (a current splitter) between the channels with a resistivity proportional to the likelihood of the electron changing channels. Mathematically this is represented by a transformation Matrix $\mathbf{D}$ that projects the spin currents on the rotated plane

$$\overrightarrow{J'} = \begin{pmatrix} J'_{\uparrow} \\ J'_{\downarrow} \end{pmatrix} = \begin{pmatrix} \cos(\theta/2)^2 & \sin(\theta/2)^2 \\ \sin(\theta/2)^2 & \cos(\theta/2)^2 \end{pmatrix} \begin{pmatrix} J_{\uparrow} \\ J_{\downarrow} \end{pmatrix} = \mathbf{D}(\theta)\overrightarrow{J}. \tag{4.2}$$

Additionally, the basic model did not consider the spin diffusion length yet. A big factor in the spin diffusion length is the occurrence of spin-flip scattering events. These can for example happen at lattice defects or in inelastic scattering events with phonons or magnons. Large atoms with large spin-orbit coupling are more likely to cause spin-flip scattering as well. This means that even with perfect alignment of adjacent particles, there is a chance that the electron will lose its spin and change channels. Hence an additional channel with a resistivity of ρ_{mix} between the spin-up and spin-down channel is necessary to complete the series resistor model. The refined model is illustrated in Figure 4.2.

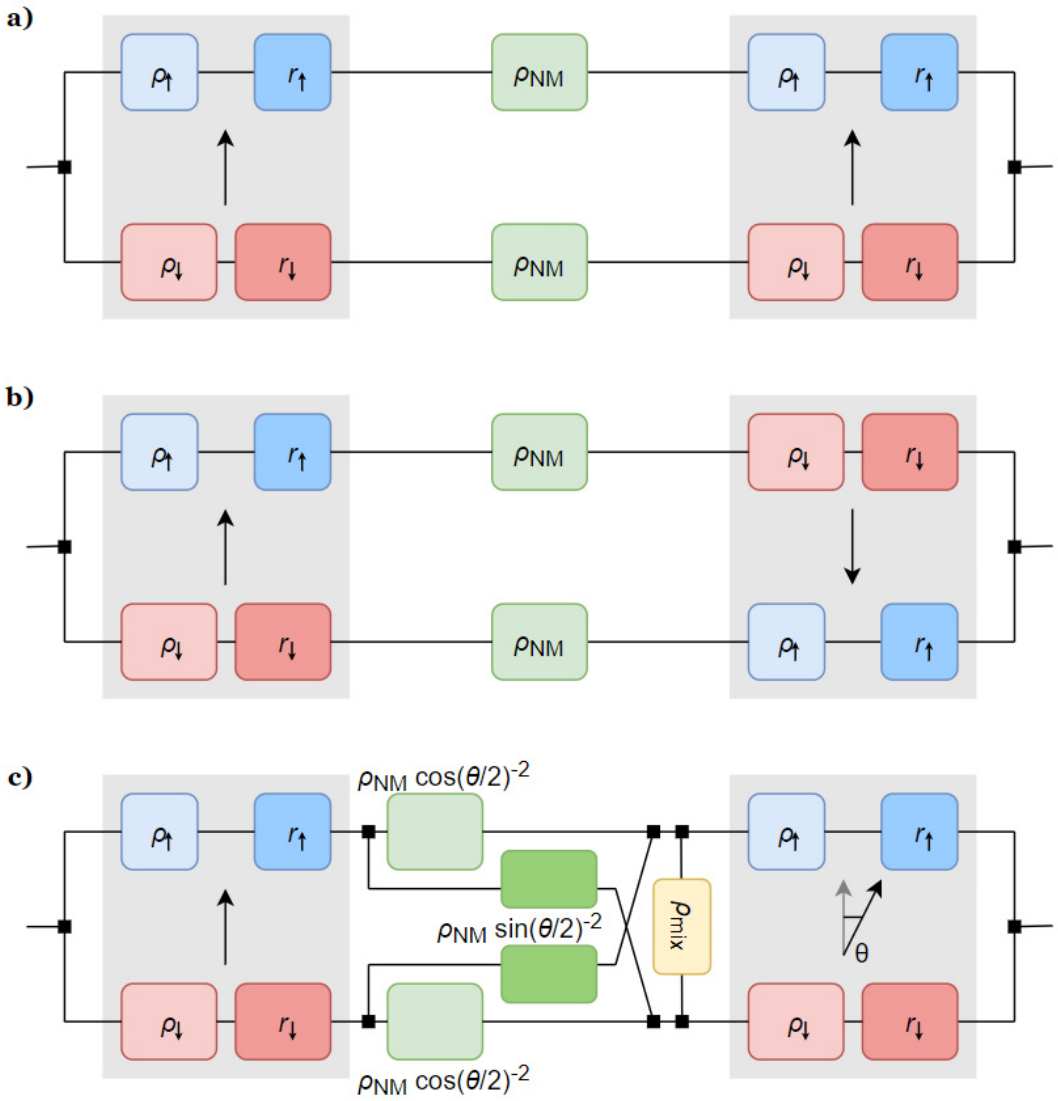

Figure 4.2: a) Schematic sketch of a current perpendicular to plane GMR system as a series resistor network in parallel configuration, with the magnetization indicated by the black arrows. Each grey rectangle represents a nanoparticle, while resistor box size corresponds to absolute resistance, indicating a low total resistance in this configuration. b) The same network in antiparallel configuration with a higher total resistance. c) The network is expanded to account for the possibility of spin flip scattering in the non-magnetic material with ρ_{mix}. Additionally, connections between the spin channels were added to consider arbitrary angles θ between to adjacent particles instead of just a parallel and an antiparallel configuration. This description closely follows the model used for simulations of granular GMR systems in [39].

4.1.2 Simulations of complex resistor networks

With the given two channel series resistor model, it is now possible to build a simulation that is able to reduce complex arrangements of nanoparticles into a resistor network and determine the expected GMR ratio of such a system. The following description closely follows [39]. In order to create a resistor network from an arrangement of particles, first the correct way to link the particles needs to be determined. Finding the optimal path between a number of locations without any boundary conditions is known as the 'travelling merchant problem' and can be very demanding in computation power. By adding a few assumptions, the problem can be greatly simplified. First, since the problem concerns traveling electrons in an electric field, all paths leading "backward" can be ignored. The electrons will take the path of least resistance which is unlikely to contain detours barring exceptionally exotic particle arrangements. Furthermore, to facilitate the GMR effect, it is a good assumption that the matrix material has significantly lower conductivity than the particles. Otherwise, the current would just shunt through the matrix without ever passing through the magnetic regions. Thus, looking at nearest neighbor connections reduces the problem's difficulty dramatically without sacrificing physical accuracy, as densely packed nanoparticles are desired, as seen in [37].
To obtain a GMR curve from the resistor network, the magnetic configuration of the particle arrangement must be defined for all applied external fields H. This is calculated independently using the CINOLA software package by Christian Schröder from the Bielefeld University of Applied Sciences, also used in [38]. For each step in the external field loop, the resulting magnetic configuration of the particles is then put into the resistor network to calculate the conductance and the expected GMR ratio. A few of the resulting curves for highly ordered and symmetric particle arrangements from [39] are shown in Figure 4.3. The results show sharp GMR curves and therefore high sensitivities with MR ratios of up to 27%. Since the effect is expected to scale with the number of particles and therefore the lateral size of the structure, exploring the experimental realization of large ordered granular structures is promising. However, some experimental challenges arise trying to translate the simulations into the laboratory. For example, the spin diffusion length for real systems is hard to measure and finding a material system that matches a long spin diffusion length with a low enough resistivity so that the particles are the main conduction channel can be hard. Therefore a limiting factor in the experiments is going to be densely packing the magnetic nanostructures and finding a suitable matrix material.

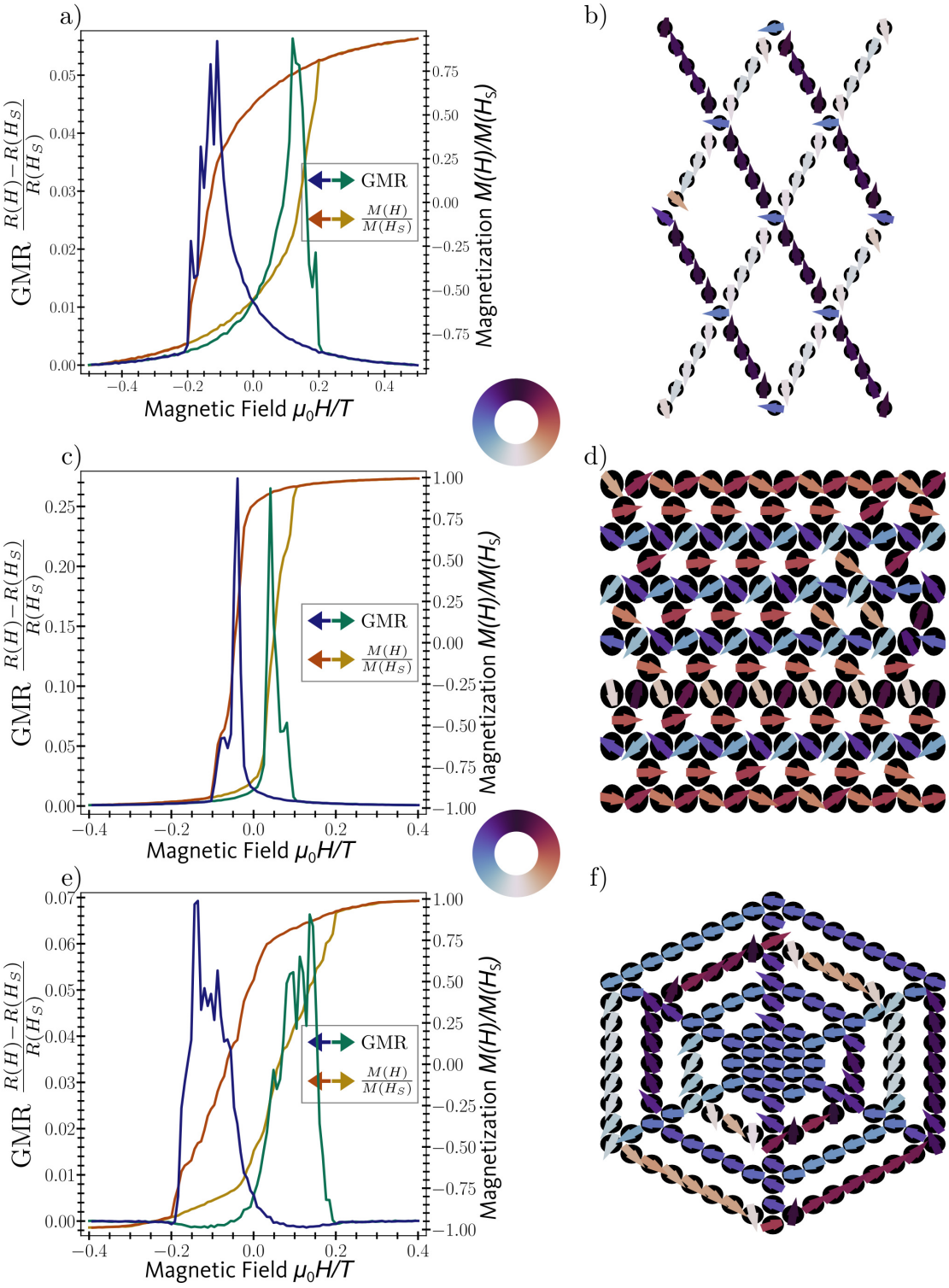

Figure 4.3: a), b) and c) Simulation of the GMR and expected hysteresis curves for different particle structures using a lattice parameter of $a = 10\,nm$. d), e) and f) show the respective magnetic configurations for the nano particles at the highest GMR. GMR was calculated from the series resistor network in each magnetic configuration. Figure reprinted with permission from the author from [39].

4.2 Characterization of focused electron beam induced deposition (FEBID) Co structures

This section will focus on the experimental realization and characterization of bottom-up nanostructures using the dual beam microscope. As discussed in chapter 2.2.3 the SCE source of the Helios NanoLab 600i was filled with the $Co_2(CO)_8$ precursor to deposit magnetic Co structures. Because the machine was not pre-calibrated with suitable parameters to deposit Co, different deposition parameters like beam energy, beam current, dwell time, and loop time had to be investigated. The quality of the results was determined by deposition efficiency and the resulting material properties. In the Helios NanoLab 600i changing the beam current also changes the total number of passes, as the machine is calibrated to believe that a higher electron dose will deposit more material. Since a large part of the deposition is facilitated by low energy secondary electrons and considering that the deposition is limited by how many precursor molecules can adsorb at any given time, depositing with a high current may not always be beneficial. For the same reason, changing the acceleration voltage will not significantly alter the deposition rate. As a consequence, an acceleration voltage of 3 kV and an intermediate beam current of 0.34 nA were chosen. These parameters provide surface-sensitive imaging at high resolution and a current about twice as high as for regular imaging. Above 0.34 nA, no significant increase in deposition rate from the Co-precursor was observed. It is worth noting however, that the deposition rate from the Pt-precursor scales well with the beam current up to several nanoamperes. Thus, ideal deposition parameters are highly material dependent.

4.2.1 Variation of dwell time

The dwell time is the time spent on a single spot by the electron beam. Along with the pitch distance of the pixels, it is possible to calculate the area dose. In order to optimize the dwell time, the irradiation time needed to dissociate all precursor molecules present in the pixel needs to be determined. Since fresh precursor atoms need time to re-adsorb to the sample surface, increasing the dwell time beyond that point will only increase the loop time without depositing much additional material. In that case, the efficiency of the process in terms of deposited material volume per time decreases. It is also well known, that electron beam irradiation can deposit residual carbon from the vacuum chamber.
As FEBID is not suitable to cover large areas with a homogeneous film, typical techniques to determine the deposition rate like X-ray reflectometry (XRR) are not applicable. Instead, the experimental setup is illustrated in Figure 4.4. Nanowires with varying dwell times were fabricated in an array so that the other important factor for the deposition efficiency, the loop time, stays constant. Subsequently, the wires were covered with a protective Pt coating, seen in Fig. 4.4 a). The covered area is then used, to fabricate a TEM lamella to determine the cross section of the deposited nanowires, which can be seen in Fig. 4.4 b). The cross section area and height of the wires can be measured using ImageJ and appropriate scaling. Along with the length of the wires and the deposition time from the dual beam microscope, the deposition rate in nm^3/s can be calculated.

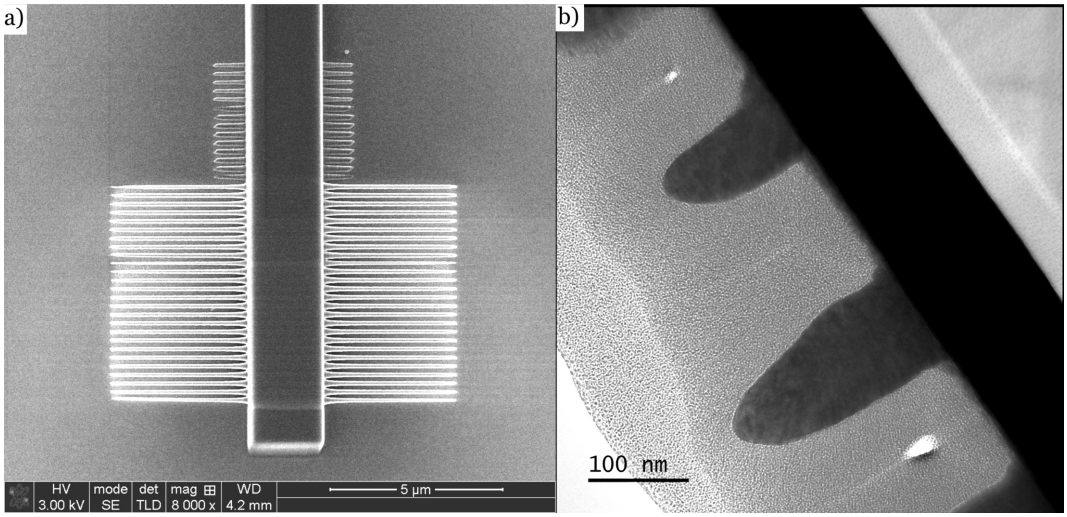

Figure 4.4: a) Co-nanowires have been prepared by FEBID using different dwell times t_D while keeping the loop time t_L and the total number of loops constant. A protective Pt-layer was deposited across the wires to protect them during the fabrication of a TEM lamella. b) TEM image of the nanowire cross section to investigate the influence of different parameters on the deposition rate and shape of the deposited object.

The resulting data can be found in Figure 4.5 for a) a loop time of 196 ms and b) a loop time of 10 ms. The experiment had to be performed twice to cover a wide range of possible dwell times. In order to keep the loop time constant, the size of the deposited wires had to be increased as the dwell time went down leading to deposition times in the order of hours for dwell times below 5 μs at a loop time of 196 ms. Therefore smaller dwell times were investigated in a second experiment with smaller structures at a loop time of 10 ms to keep total deposition times and structures small. This leads to the discontinuity in the deposition rate, as the loop time can influence the deposition rate. The data for both dwell time ranges clearly indicates, that shorter dwell times increase the deposition efficiency dramatically. As a result, the dwell time should be as low as possible to achieve maximum yield from the process. The error bars represent an estimated 10% uncertainty in the deposited volume because slight differences in focus and astigmatism or a slight drift of the stage can alter the shape of the deposited wire, leading to possible artifacts. Within the margin of error, the exponential fit agrees well with the measured data.
Practical tests show, that choosing a dwell time of 1 μs has the highest efficiency of all tested parameters. However, the loop time of smaller patterns can be so short, that the scanning frequency of the beam cannot follow. To avoid this problem, a dwell time of 2 μs has been chosen for all following experiments to keep results uniform. This trend was expected because the Co-precursor is a relatively unstable molecule, so low energies are already sufficient to dissociate it. Thus, the dissociation should happen almost instantly upon electron beam irradiation. These results also agree qualitatively with the findings of Lipp *et. al.* in [43].

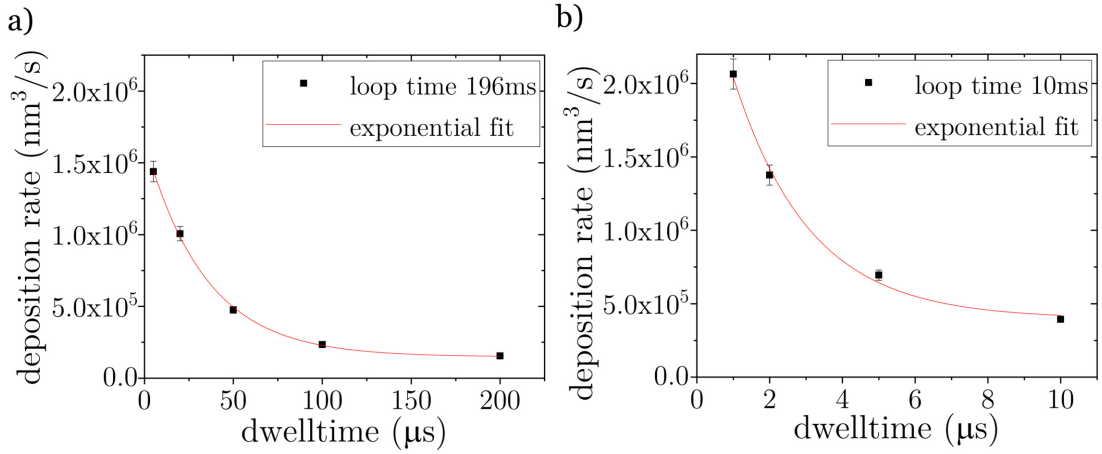

Figure 4.5: Influence of the dwell time on the volume deposition rate defined as nm^3/s in order to investigate the dissociation time of the precursor a) in a range from 5 μs to 200 μs with a loop time of 196 ms. b) in a range from 1 μs to 20 μs with a loop time of 10 ms, since the structures were too large for a TEM lamella at 196 ms.

4.2.2 Variation of loop time

Unlike the dwell time that can be set to arbitrary values, the loop time is a direct result of the dwell time and the size of the deposition pattern. In a realistic setting, where a specific structure is desired, the options to influence the loop time are therefore limited. However, as the precursor gas needs time to re-adsorb to the substrate after each pass of the beam, it is valuable to determine the adsorption saturation time for the precursor, so that the other parameters can be adjusted accordingly. Ideally, the loop time is always longer than the adsorption time of the precursor so that the deposition is efficient. Experiments with different dwell times have shown that extremely short loop times can cause additional artifacts because the scanning coils for the beam cannot operate at the needed frequency.
The preparation of the test samples is identical to the dwell time experiments. First, a series of nanowires with different loop times was deposited using a dwell time of 2 μs for all wires. Then a TEM lamella of the wire cross sections was prepared so that the amount of deposited material could be determined. Unlike the previous experiment, the deposition rate was calculated as wire height per loop. This is because the adsorption saturation time of the precursor can be found by looking at the added layer thickness per electron beam pass. If instead the added volume was measured, the results would skew to larger structures with higher loop times just by virtue of the experimental setup. Again, a 10% error for the height of the deposited wire was estimated, since slight variations in focus and astigmatism or a small stage drift can influence the shape of the nanowire cross section. This can be observed in the results in Figure 4.6 for the data points at a loop time of 1.3 ms and 2.1 ms. Qualitatively the data shows the expected result, that the deposition rate saturates at a certain point. To guide the eye the data was fitted using a Michaelis-Menten function, which appears to agree well with the data. This type of function is normally used to describe enzyme reactions, where an enzyme binds reversibly to a substrate, which is then processed by the enzyme. The equation suggests that the maximum reaction rate of the system saturates when the substrate is available in

abundance. The FEBID process satisfies a similar assumption about the reaction. Thus, the fit is viable to qualitatively describe the process.
From the given data, the saturation time can be estimated to be around 10 μs. It is difficult to estimate an error in this case, as the region of interest contains two outliers that are not well represented by the fit. For practical purposes however, this result is satisfactory. Compared to the Pt-precursor the saturation time of Co is extremely long, since with platinum even continuous irradiation of a single spot results in a reasonable deposition rate. This is important in the design of the nanoparticle pattern for the granular GMR. In theory, two pattern designs for the nanoparticles are possible. The first is based on drawing an array of individual circle shapes that can be patterned either in parallel or serial mode. Since each circle consists of several densely packed pixels, the efficiency of such a process, given the long readsorption time of the Co-precursor, would be very low. Hence the second deposition strategy, where a closed rectangle shape with a high pitch distance to form individual particles is drawn, is the better choice. In this way, each particle is only exposed for a single dwell time each cycle. Since the dissociation time is short and the readsorption time comparatively long, this process maximizes the deposition efficiency of the particles. However, the possible particle patterns are limited to square or rectangle lattices. If more elaborate patterns like the diamond pattern from chapter 4.1.2 are desired, the same trick can be applied to line patterns by changing the pitch distance. To fabricate the first test samples, square particle grids were chosen, because of their high deposition efficiency.

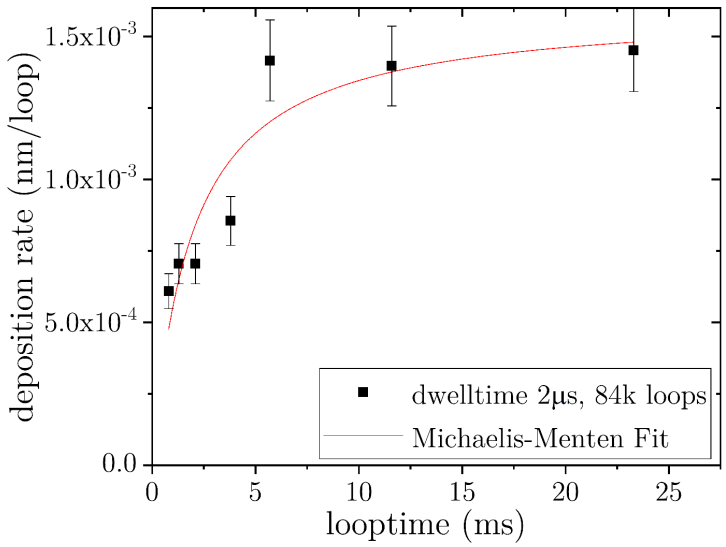

Figure 4.6: Influence of the loop time on the deposition rate defined as nm / loop to investigate the readsorption time of precursor molecules on the substrate surface. Data was analyzed using a Michaelis-Menten fit, which is used for dissociative enzyme processes on surfaces and proved to be a suitable model for this problem. The dwell time was kept at $t_D = 2\,\mu$s, because for small structures artifacts would occur at lower dwell times, as the machine could not keep up with the needed beam deflection frequencies.

4.2.3 Microstructure analysis using transmission electron microscopy

Similar to the experiments on the deposition rate of FEBID-Co, commonly used thin film methods like X-ray diffraction (XRD) are not applicable, because of the small sample volume. Instead, the nanoparticles were deposited on a TEM grid with a graphene membrane to investigate the microstructure. Because of the graphene layer's low interaction volume, far fewer secondary electrons are generated from the graphene substrate, which results in a lower deposition rate on the TEM grid. The most stable Co phase has a hexagonal lattice with an in plane lattice parameter of $a = 2.501\,\text{Å}$ and a magnetic moment of $1.607\,\mu_\text{B}$ per unit cell [44]. Other Co phases can have cubic or trigonal lattices and carry a slightly higher magnetic moment. However, these phases have formation energies of 0.01 eV up to 0.199 eV and therefore require special conditions to occur.

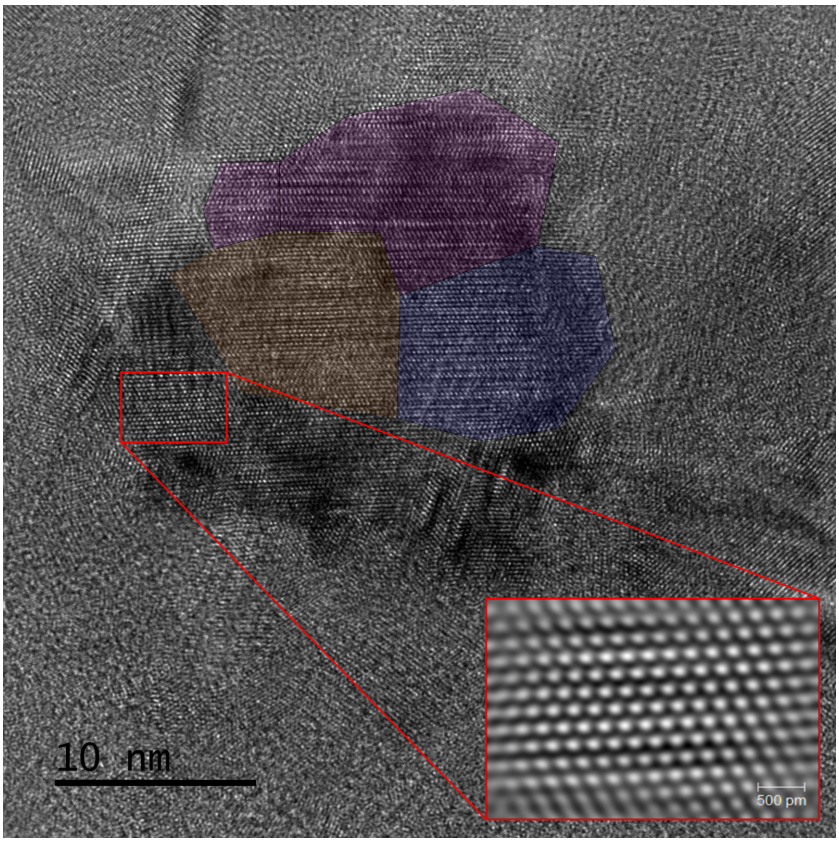

Figure 4.7: TEM image of a Co-particle deposited on a graphene TEM grid. The zoomed-in area (red box) has been corrected using Fourier transformation filtering and clearly shows a hexagonal lattice structure. Some grains have been colored as a guide to the eye to estimate the grain size.

In order to investigate the influence of the substrate, Co-nanoparticles were deposited on three different graphene grids. One grid had a 5 nm V seed layer, one grid had a 5 nm Pt seed layer and the third grid had no seed layer as a reference. Vanadium has a bcc lattice with a lattice constant of 2.592 Å, Platinum has a fcc lattice with a lattice constant of 2.812 Å and graphene is hexagonal with a lattice constant of 2.465 Å [45, 44]. Since the mismatch between graphene and Co is small,

the nanoparticles are expected to be in the stable hexagonal phase on graphene, but deposition on a seed layer could change the growth conditions. Additionally, all samples were heated in the TEM to up to 350 °C after observing the as-deposited microstructure. In materials with many impurities such as FEBID-Co, post growth annealing can promote atomic ordering, evaporate foreign atoms or change the phase of the material.
Figure 4.7 shows a high magnification TEM image of the as deposited Co-particles on the graphene membrane without a seed layer. To guide the eye, some visible grains have been colored to give an estimate of the average grain size. The magnified inset was Fourier corrected to make gauging the lattice parameter easier. In the highlighted area, the lattice structure was hexagonal with a lattice parameter a between 2.468 Å and 2.506 Å, which matches well with the expected hexagonal phase. The out-of-plane lattice parameter c was not observed. Due to many impurities in the Co-particles and a highly non-uniform thickness of the particles a statistical analysis of the grain size was not possible. However, the average grain size in the as deposited state is estimated to be between 5 nm and 10 nm. In the samples with a V and Pt seed layer, the Co-particles were also grown in the hexagonal phase with the same lattice parameter and roughly the same grain size.
After heating the samples to 350 °C, shown in Figure 4.8 for the sample with a V seed layer, the average grain size had grown considerably and is estimated to be larger than 20 nm. Some grains have been colored to guide the eye. It can be seen from the magnified and Fourier corrected inset, that the lattice is still hexagonal with a lattice parameter between 2.468 Å and 2.506 Å. The same result could be observed for the graphene membrane without a seed layer. In the case of the third sample with a Pt seed layer, the Co-particles were absorbed into the seed layer and vanished, since Pt and Co mix quite well. In conclusion, the hexagonal Co phase seems to be stable and mostly independent from the tested seed layers. Annealing of the particles increases the average grain size, however, even in the as deposited state the particles are polycrystalline and should therefore be ferromagnetic. In some cases, a few particles merged due to surface tension during heating. Thus, annealing should be avoided when creating densely packed nanoparticle arrangements for GMR sensors.
Energy dispersive X-ray spectroscopy (EDX/EDS) measurements performed in the TEM on the as deposited particles reveals a Co content of 46.46 at.% in the particles with the remaining 53.54 at.% being carbon. It is worth noting, that light elements like C, O, and N are difficult to reliably quantify with EDS since their characteristic X-rays have low energy. In this energy band, there is a large amount of background due to brake radiation, which makes quantitative measurements unreliable. Additionally, the graphene membrane can be responsible for a higher C signal. Serrano-Ramón *et. al.* have reported as deposited Co-contents of 60 at.% to 80 at.% dependent on the precursor gas flux. Therefore 46.46 at.% Co is likely a low estimate for the true Co-content of the particles. Since light elements like C do not provide much contrast in the TEM, it is not possible to derive the distribution of residual carbon impurities from the TEM images.

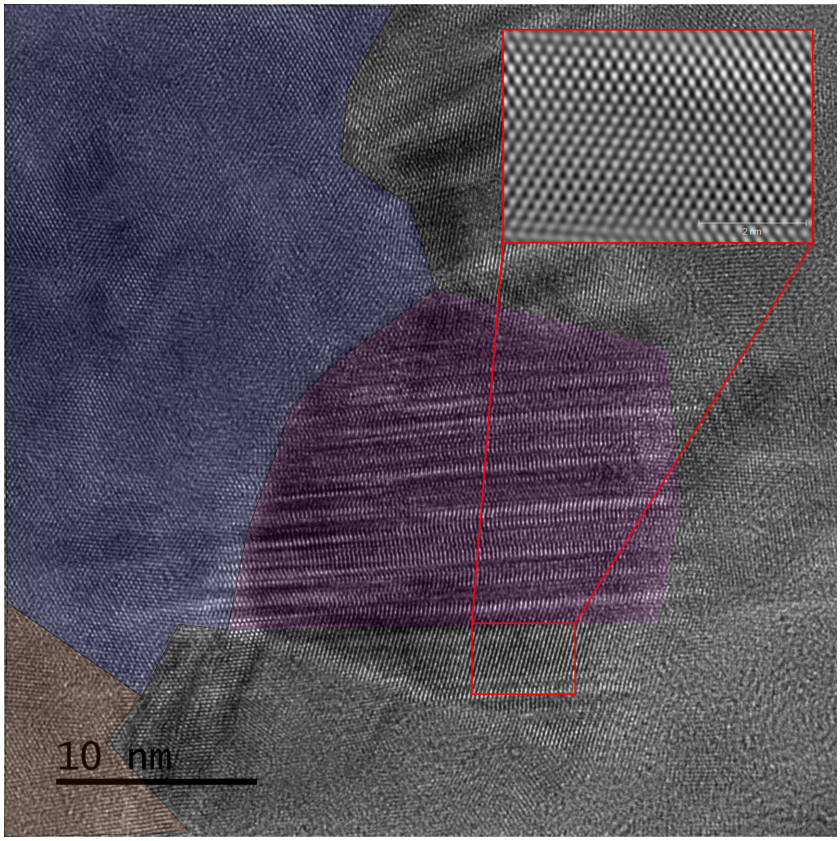

Figure 4.8: TEM image of a Co-particle deposited on a graphene TEM grid after heating in situ at 350°C. The zoomed in area (red box) has been corrected using Fourier transformation filtering. The sample shows no difference in crystal structure but overall larger grain size.

4.2.4 Magnetic characterization

In order to measure the magnetic moment of the FEBID nanoparticles, a large array of nanoparticles was prepared on a silicon wafer with an amorphous 50 nm silicon oxide layer. The particles were created by patterning a set of 2 μm squares with a pitch distance of 100 nm. In total, more than $4 \cdot 10^6$ particles were deposited over the course of more than 10 hours. Figure 4.9 a) shows a SEM image of the resulting particles at a tilt of 52° to estimate the height with the tilt corrected integrated measurement tool of the Helios Nanolab 600i. Most particles are cylinder-shaped with a width of about 50 nm to 55 nm and a height of 40 nm to 42 nm. For a rough estimation, the particles are assumed to be cubes with an edge length of 50 nm, which gives a volume of $1.25 \cdot 10^{-16}\text{cm}^3$. The magnetic moment was measured in a Micromag 2900 alternating gradient magnetometer (AGM). In an AGM the sample is mounted to the end of a rod, that is suspended in such a way that it can move freely in the xz-plane. The sample is magnetized by a DC field of variable magnitude and simultaneously exposed to a small alternating field gradient, which exerts a force on the magnetic sample. This force is proportional to the magnitude of the magnetic moment of the sample. By operating near the mechanical resonance frequency of the rod, the output signal is immensely amplified [46]. The resulting graph for the FEBID-Co particles is shown in Figure 4.9 b).

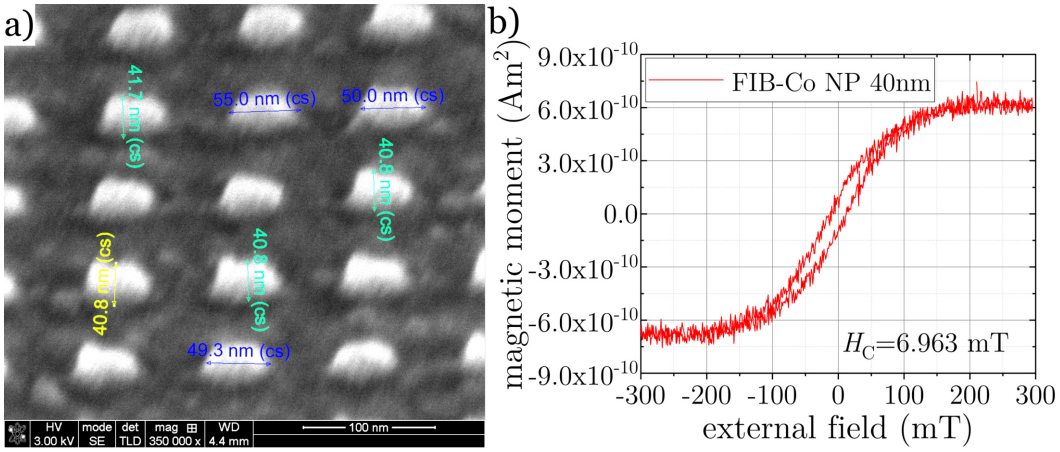

Figure 4.9: a) SEM image with measurements of Co particles deposited using 3kV acceleration voltage 0.34 nA beam current and a dwell time of 2 μs on a Si wafer. b) AGM measurement for Co-particles using the same conditions deposited on a Si wafer with V underlayer, corrected for diamagnetism of the substrate by linear regression.

Since the silicon substrate is diamagnetic, the measured data was corrected by subtracting the diamagnetic response, which is a simple linear function. With the characteristic hysteresis shape of the curve, the data clearly indicates a ferromagnetic behavior for the nanoparticles. The coercive field, which is the intercept of the curve with the field-axis, is at 6.963 mT in the same range that one would expect to find in a Co thin film. As the actual total volume of the deposited Co is hard to gauge, the total magnetization of the FEBID-Co can not be calculated. To put the saturated magnetic moment of $7.5 \cdot 10^{-12}$ Am^2 into context, a few estimations can be made. Waddell *et. al.* found a saturation magnetization of roughly $9 \cdot 10^5$ A/m for a dispersion of ϵ-Co nanodiscs, which for the sake of this argument shall be 10^6 A/m [47].
The measured saturation moment from a material with this magnetization corresponds to $7.5 \cdot 10^{-10}$ cm^3 worth of magnetic material, which is equivalent to $6 \cdot 10^6$ Co cubes with a size of 50 nm. Thus, the measured moment for the prepared test-sample is about 1.5 times larger than expected even when the generous estimate of the magnetization is not considered. Due to the carbon impurities in the particles, the real magnetization should actually be smaller. A possible explanation is the high uncertainty of the real amount of deposited material. Since the dissociation process of the precursor is mainly caused by slow secondary electrons, FEBID structures often have a "halo" of additional material around the exposed area, as secondary electrons from the substrate can be scattered outside of the directly exposed area. Additionally, there is a certain margin of error in the AGM measurement itself, because the total magnetic moment of the sample is very low. Most thin film systems, which the machine was designed for, exhibit moments that are orders of magnitude higher. In conclusion, while a clear ferromagnetic behavior can be seen, it is not possible to calculate a convincing magnetization for FEBID-Co.

4.2.5 Lateral resolution limit and scaling issues

For the purpose of building reliable magnetoresistive devices, two main factors are of interest. First, the spatial resolution needs to be high enough, so that particles

can be densely packed on the substrate. Since the spin diffusion length is hard to measure and depends greatly on the properties of the matrix material, as discussed in chapter 4.1, the minimum distance, that the fabrication technique can achieve is desired. Second, the fabrication method needs to be scalable to cover large sensor areas. Unlike epitaxial sensors, which optimize the transport properties by minimizing defects, a nanoparticle sensor consisting of polycrystalline particles needs as many interfaces for spin dependent scattering as possible to alleviate the losses incurred by the worse crystal structure.

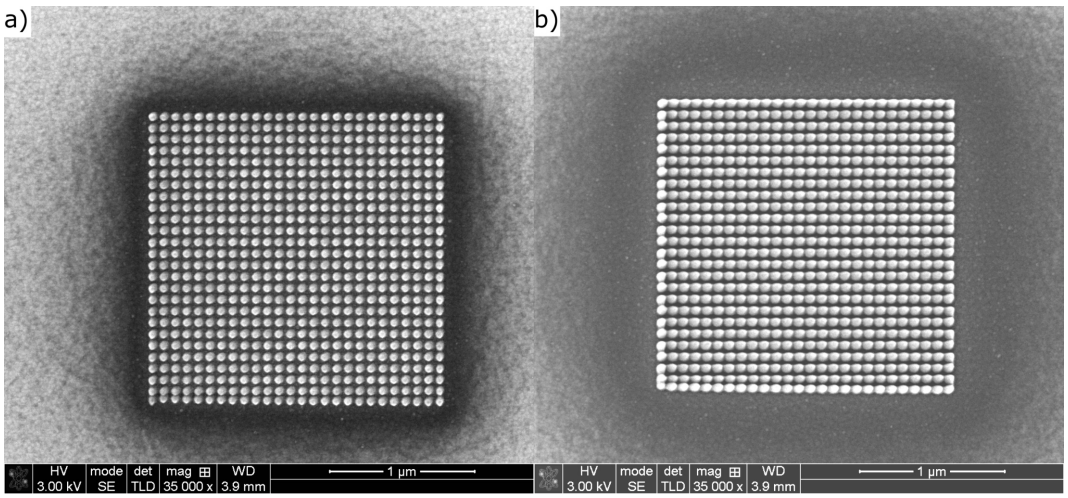

Figure 4.10: SEM image of a 2μm x 2μm grid of Co particles with $p_{\mathrm{x/y}} = 80\,nm$ deposited with optimized conditions at 3kV using a beam current of 0.34 nA and $t_{\mathrm{D}} = 2\,\mu$s. The z-size for the pattern was set to a) 50 μm which corresponds to 86350 loops and b) 100 μm which corresponds to 172700 loops. Even at higher thickness, the particles still appear to be well separated.

Figure 4.10 shows a 2 μm by 2 μm square of test particles with a pitch distance of 80 nm in both x- and y-direction for a) a z-size of 50 μm and b) a z-size of 100 μm. These are arbitrary units because of the missing software calibration for the Co-precursor and correspond to 86350 and 172700 loops respectively. For pitch distances below 80 nm, the particles were not well separated anymore and began to fuse, similar to the thicker particles in Fig. 4.10 b). While this resolution is worse than the resolution limit of electron beam lithography reported in [2], the referenced work refers to thin film structures of less than 10 nm in height. For particles with a height of about 40 nm, the given resolution is remarkable. All test squares were deposited with the previously determined conditions of 3 kV acceleration voltage and 0.34 nA beam current in the SEM immersion mode of the Helios Nanolab. These test particles are densely packed with a distance of only about 14 nm and well separated so that no continuous films form. Since the particle shape is strongly dependent on the focus and astigmatism of the electron beam, these settings need to be carefully checked before deposition. Because the electron beam takes a meandering path, asymmetries of the x- and y-spacing can occur when residue Co is deposited between pixels. This is easy to spot in Fig. 4.10 b), where the x-spacing is much smaller than the y-spacing and the particles are not ideal cylinders.

To investigate how increasing the pattern size affects the deposited material, three approaches to scale the 2 μm test patterns to at least 40 μm were tested. It is possible to either increase the size of the drawn pattern or to stitch together several smaller patterns. For the latter option, a script can be used to either draw an array of small particle squares or to move the stage below a single pattern that is repeatedly exposed, similar to large structures in e-beam lithography.

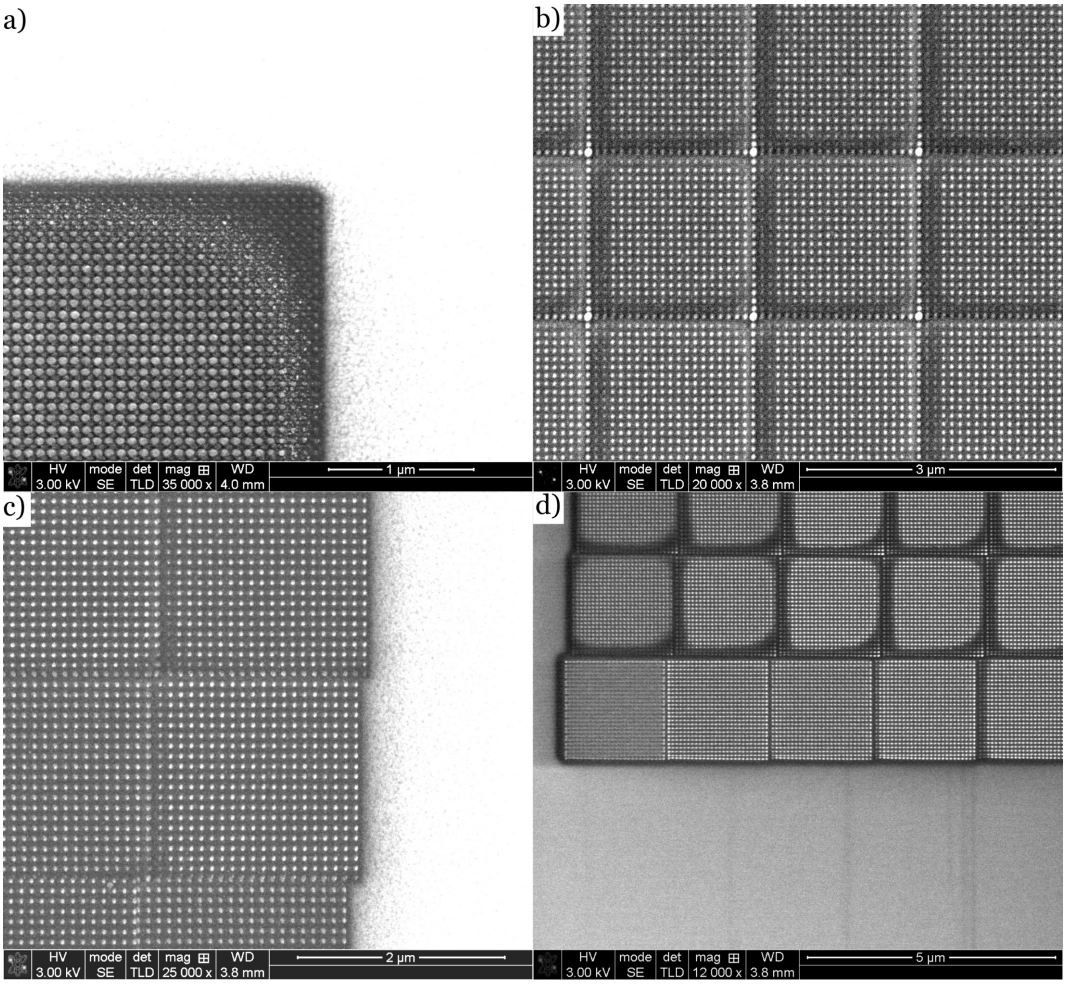

Figure 4.11: SEM images of different deposition artifacts: a) incomplete deposition at edges on larger structures than 8 μm b) reduced deposition rate at overlapping edges c) error in stitch pattern placement after stage movement d) reduced deposition rate at edges for long consecutive deposition processes.

Figure 4.11 shows the unexpected artifacts in the deposited patterns, that occurred for the different scaling methods. The artifact in Fig. 4.11 a) occurs for single patterns that are larger than about 8 μm in any direction. In this case, the edges and corners have heavily deteriorated and the outer lines of particles can only be seen faintly on the background material. Tilting the sample revealed, that indeed only small amounts of material were deposited near the pattern boundaries. As the size of the deteriorated area increased with the pattern size, a possible explanation for the damage is inhomogeneous precursor flux along the sample.

The precursor gas is injected from a needle only a few microns away from the substrate surface and therefore highly inhomogeneous. Since the amount of adsorbed precursor gas on the substrate is expected to saturate, this is not a problem for depositions close to the needle, as the precursor is available in abundance. In areas farther away from the tip of the needle, the flux decreases to the point, where adsorption does not saturate anymore, explaining the diminished effectiveness of the deposition. To address this problem, the pattern was changed to an array of 2 μm by 2 μm squares with the same total size. If the assumption is true, the artifact would still occur when the array is exposed at once, but not when only a single small pattern at a time is exposed and the stage is moved between exposures.
However, other artifacts occured in both structures, which are depicted in Fig. 4.11 b) and c). Beside a small overlap increasing the total exposure time for the corner particles and therefore their size, the same deteriorated boundaries can be seen in the individual small squares, which previously did not exhibit any artifacts at all. Additionally, in the case of Fig. 4.11 c), where the stage was moved below the pattern, a random offset of the stage movement occurs. Unlike an interferometer stage, that is commonly used in e-beam lithography and can be positioned accurately with an error of only a few nanometers, the step motors driving the 5 axes of the motorized stage in the Helios Nanolab have a repeatability of 1 μm. This means that, while smaller movements than 1 μm are possible, a repeated movement of a certain distance can incur an error of up to 1 μm. To alleviate this problem, the pattern can be programmed with a small overlap. An overlap of the patterns would lead to larger or oddly shaped particles in some areas, but too large gaps between particles would be worse for the GMR output of the sensor.
Figure 4.11 d) offers a hint to the origin of the deteriorated edges in the 2 μm squares. The image shows a second array of squares, that was deposited on a different day. This process also used a script to move the stage, which explains the random offsets and small overlaps. It is worth noting however, that individual squares were deposited in a meandering pattern from bottom to top. Thus, the defect-free squares were deposited first and the deterioration build up over time. At a certain point the defect size seems to have saturated, i.e. a steady state was reached. A possible explanation for this beavior is, that the maximum precursor flux from the needle is limited and insufficient to continuously expose large areas. Before starting the exposure process, the GIS is pre-heated, which allows some precursor gas to build up in the storage chamber. This results in a high gas flux and thus defect-free patterns until the reservoir is used up. At that point, the flux becomes limited by the evaporation rate. Since the Co-precursor is extremely sensitive to temperature, increasing the flux by setting a higher heating temperature is not possible.
As a result, FEBID-Co particles are an interesting material for small-scale applications, but larger sensors or serialization of sensor arrays is limited by the scalability of the deposition process. For the Pt-precursor, none of these artifacts could be observed. Therefore, the origin of the fabrication challenges likely stems from the different chemical properties of the Co-precursor.

4.3 Top-down fabrication of nanoparticles using focused ion beam milling

In contrast to the presented direct-write approach, several options are available to create nanoparticles from sputter-deposited thin films in a top-down process. Since conventional e-beam lithography is limited by the resist and desired film thickness, it is not suitable for creating densely packed arrays of particles of the desired size. Nanosphere Lithography is a process that uses polystyrene nanobeads as a hard mask for thin film deposition or etching [48]. If the beads can be applied in an even monolayer, the resulting structures are highly ordered and the particles have a low variance in size. The achievable particle distance is limited by the bead size, which makes the technique undesirable for the granular GMR sensors as well. It is, however, a useful method to create plasmonic structures.
In this work, the magnetic thin films are patterned with the focused ion beam in a dual beam microscope. Therefore, Py thin films were cut into squares and rectangles using a grid of line patterns that was created by a script. This idea was inspired by a work on plasmonic nanoparticles by Chen *et. al.*, who used a focused ion beam to draw the outlines of the desired particles in a gold film [49]. Instead of using the ion beam to etch the material between the particles, tape was used to remove the material. Due to the redeposition of sputtered atoms in the FIB-milled trenches, the particles remained firmly attached to the substrate, but with a larger surface area the spaces in between were removed. By using the milled trenches as the gaps between nanoparticles, the particle density for granular GMR sensors can be maximized.
This technique offers a few options for the particle design that was not possible in the bottom-up approach using FEBID. For example, the particle size can be freely adjusted without a drastic increase in fabrication time, making it easy to cover large areas. Sputter deposited thin films also do not contain carbon impurities, which negatively influence the conductive and magnetic properties of the particles. Additionally, the patterning grid can be adjusted to create any particle shape, which brings about interesting symmetry options. By patterning rectangles instead of circles or squares, it is possible to introduce a shape anisotropy that gives the particles a preferred magnetization axis for example. It is also possible to pattern grids in which particles of different sizes are present.

4.3.1 Focused ion beam milling parameters

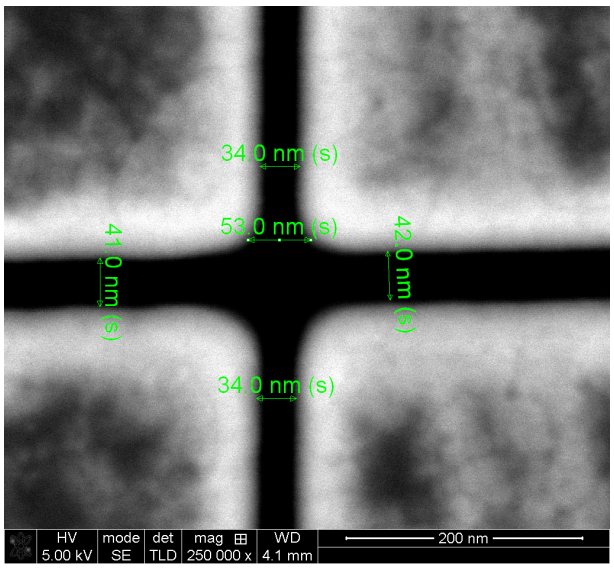

Figure 4.12: SEM image of trenches generated by milling a line grid of 30 nm depth on a Au surface. The ion beam used 30kV acceleration voltage and a 9.7 pA beam current.

To fabricate large patterned sensor areas, the beam parameters for the focused ion beam need to be carefully considered. For high imaging resolution and milling yield, the typical acceleration voltage for the Ga-ions is 30 kV. At lower acceleration voltages, the beam is less damaging to the areas surrounding the patterned area. During the fabrication of a TEM lamella, the fine polishing steps are usually done at 5 kV. However, the beam is very sensitive to focus and stigmation settings and the milling rate is orders of magnitude smaller than for 30 kV. Therefore, an acceleration voltage of 30 kV is the preferred setting for milling the trench grid. The smallest possible beam diameter in the Helios Nanolab is achieved with the 1.5 pA aperture. Since the milling speed with this aperture is quite slow, the next highest setting of 9.7 pA, which is also commonly used for imaging, is chosen. These settings were tested by patterning a square grid in a 100 nm Au-film that was sputter deposited on a Si substrate. Figure 4.12 shows a SEM image of the resulting trenches. The depth of the trenches was set to 30 nm, but since the milling depth is calibrated for silicon and gold sputters easily, the structures are likely much deeper. In this example, the horizontal lines with a width of 41 nm and the vertical lines with a width of 34 nm are not the same size, even though both were defined as line patterns in the script. As the grid was set to parallel milling mode to avoid redeposition at the intersection of horizontal and vertical lines, the patterns are combined. Thus, the beam scans the pattern in horizontal meandering lines and “hops” for the vertical lines, whereas horizontal lines are directly scanned. Changing the milling mode to serial means that each line is finished before the next one is started. The redeposition of milled material, which could shunt the probing current in the finished sensor, was found to be negligible.

4.3.2 Experimental challenges

Similar to the bottom-up fabrication of FEBID nanoparticles, the resolution limit and possible artifacts for the top-down milling process need to be considered. In order to produce comparable results a sputtered Co film of 30 nm thickness was considered for the trench structures at first. However, unlike the Au test sample, the milling efficiency of Co was low. Additionally, by increasing the mill time the trench width also increased. Therefore, a softer Py film was chosen for these samples. As Py does not mill as easily as Au, the milling depth was increased to 70 nm to ensure that the particles are isolated. The minimum trench width for Py with the given settings of 30 kV acceleration voltage and a beam current of 9.7 pA was between 35 nm and 45 nm. For these samples, the correct choice of matrix materials to fill the gaps is critical. Because the gaps between particles are quite large, a material with a long spin diffusion length is desired. Bass and Pratt reviewed experimental and theoretical findings for the spin diffusion length of various materials and found that especially good conductors like Au and Ag can have spin diffusion lengths $l_{\mathrm{sf}} \geq 100\,\mathrm{nm}$ [50]. However, most reports were made for epitaxial samples. In polycrystalline samples with worse conductivity and more scattering centers, l_{sf} is likely much shorter. In addition to the minimum trench size, the particle size has a lower limit due to the high energy of the beam. For particle sizes $l \leq 180\,\mathrm{nm}$, the beam partly melted the particle and resulted in undesirable artifacts. Lastly, the ion beam can slightly defocus during long milling processes that last for a few hours. To avoid broadening of the trenches, it is necessary to split large patterns into several parts and adjust the focus between each milling.

4.4 Granular GMR device prototyping

4.4.1 Design and measurement geometry

The base samples for the top-down granular GMR samples were prepared using two lithography steps. First, an array of paired contact pads was exposed on a Si wafer with 500 nm of amorphous silicon oxide as the top layer using AR-P 617.08 positive electron beam resist [51]. Most commonly used Si wafers only have an oxide layer of about 50 nm, but in order to make sure the ion beam does not mill through the oxide accidentally, the thicker oxide variant was chosen. If the oxide layer was damaged, the measurement current could shunt through the doped semiconductor and cause measurement artifacts. The Au contact pads with a thickness of 120 nm were sputtered onto a seed layer of 2 nm Ta, as Au has poor adhesion to the Si substrate without it. Additionally, cross marks were placed in the corners during this first lithography step, in order to align the second step. In the second step, a 60 μm square was added at the center of each contact pad pair to bridge the gap. The same positive resist was used to create the sputtering mask for the magnetic Py layer. The Py films were subsequently patterned with different trench grids to create a lattice of ordered magnetic particles. To create the base samples for the bottom-up granular GMR using FEBID, the same design was chosen and the second lithography step was simply omitted. Furthermore, the gap between the contact pads was shrunk to 40 μm, since the FEBID process is very time-consuming. For the direct write nanoparticles a pattern of stitched squares, as described in chapter 4.2.5, was used and a small overlap was added to avoid most artifacts.

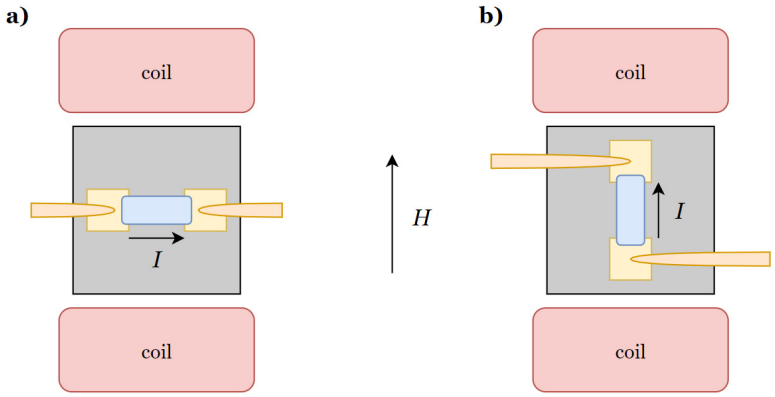

Figure 4.13: Sketch of the measurement geometry for GMR samples between a pair of Helmholtz coils providing the external magnetic field H_{ext} a) with the current perpendicular to H_{ext} and b) with the current parallel to H_{ext}. Rotating the sample helps to identify AMR and an easy magnetic axis induced by the anisotropic pattern. Since the intrinsic resistance is expected to be high, a two-point measurement is sufficient.

Figure 4.13 shows the two general measurement geometries for GMR samples a) current perpendicular to the field and b) current parallel to the applied field H_{ext}. In thin film samples, the GMR is independent of the measurement geometry, however when anisotropies are concerned, measuring both geometries can be useful. As an example, the coercive field of rectangular particles is expected to be different for the

long and the short axis. Additionally, it is possible to identify the anisotropic magnetoresistance effect (AMR) by rotating the sample. The AMR effect occurs mostly in bulk or thin film samples, but could also appear in the top-down granular samples if the spacing between the milled trenches is large enough. In a ferromagnetic sample the electrical resistance depends on the angle between the current and the direction of the magnetization. AMR originates from an interaction of localized spins (the magnetization) and the spin of the conduction electrons (the current) and is often attributed to spin-orbit-coupling in literature [52]. As a result, the AMR peak in GMR measurements, that occurs around $H_{\text{ext}} = 0$ when the magnetization of the material is reversed, changes its sign when the sample is rotated by 90°. Figure 4.13 also contains a sketch of the sample design with Au contact pads and needles in yellow and the area with magnetic particles in light blue. Since the total resistance of the devices will be higher than in metallic thin film samples due to the patterning, a four-point measurement is not necessary in this case. A four-point measurement can be used to eliminate the contact resistance of the probing needles and the resistance of the wires which is assumed to be negligible for the given samples.

4.4.2 Exploring filling materials

In a previous work by Inga Ennen, chemically prepared nanoparticles were spread on a substrate and subsequently covered with a Cu coating of a few nanometers. While the experiment was successful in creating a measurable GMR from the nanoparticle device, the observed MR ratio was in the order of 1 %. A possible explanation for the low effect is shunting of the current through the Cu layer instead of the particles, bypassing most of the FM-NM interfaces (c.f. chapter 4.1.2)[36].

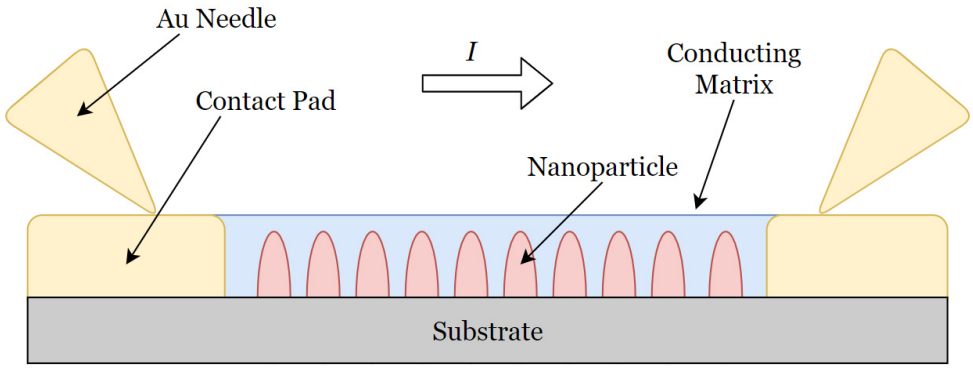

Figure 4.14: Sketch of the cross section of a GMR sample in the measurement setup. The gaps between the particles are filled by a conducting non-magnetic matrix, which acts as the spacer layer in the thin film equivalent. To avoid shorting the nanoparticles the conductivity of the matrix should be lower than the particles'.

Figure 4.14 shows a cross section of the sample structure, which is in essence identical to the granular GMR devices prepared in this work. If the matrix is a good conductor, the path of least resistance goes around the particles and only a fraction of the current will pass through the particles. Since this approach to GMR

sensors is to force the current to pass a large number of interfaces, a few conditions to a good matrix material can be deducted. First, the matrix material can not be a better conductor than the particles, since this would promote shunting of the particles. Second, the matrix has to be as thin as possible, as increasing the matrix cross section reduces the overall resistance and thus shunts the particles as well. Finally, the matrix material has to protect the particles from corrosion and should not react with the particle surface in any way.
Given these criteria, a few materials can be examined with regard to their suitability as a matrix material. The first candidate is the "Protective Coating PMMA Electra 92 (AR-PC 5090)" by AllResist, which is a conductive PMMA based lacquer that contains dispersed carbon particles [53]. It is commonly used to facilitate e-beam lithography on poorly conducting substrates like MgO or glass. To apply the lacquer a generous amount is applied to the substrate, which is then spun at 2000 rpm for 60 s to apply an even coating of 60 nm. According to the manufacturer, the lacquer layer has a specific resistivity of about $8.33 \cdot 10^5\,\Omega\mathrm{mm}^2/\mathrm{m}$. In first experiments with the lacquer Joule heating from the applied current quickly destroyed the layer, making the material not suitable as a matrix material.
A second possible candidate is a silver-based electrically conducting adhesive. These compounds consist of organic solvents and 30-60 % dispersed Ag-particles. Some conductive adhesives contain epoxy-based adhesives since they can be used to mend broken connections on circuit boards. Depending on the manufacturer and the added epoxy, silver-based adhesives have a specific resistivity in the order of $10\,\Omega\mathrm{mm}^2/\mathrm{m}$, which is five orders of magnitude smaller than the carbon based lacquer [54]. Unfortunately, it was not possible to design a repeatable process to apply small amounts of conductive adhesive to the sensor area due to the high viscosity of the medium and the fast evaporation of the solvent. In all experiments, the conductive adhesive layer shunted the underlying nanostructures. Thus, conductive adhesives were discarded as a matrix material.
The last candidate as matrix material is a Pt layer deposited by FEBID, which can be done in situ. Unlike the other presented materials neither the FEBID-Co particles nor the interfaces of the milled Py particles can oxidize before the matrix is applied using this method. The main downside of FEBID-Pt is the required deposition time of several hours for a film of 60 μm size.
To probe the suitability of FEBID-Pt, a series of test bars was fabricated to measure the resistivity of the deposited films. Since materials deposited by focused ion beam induced deposition can contain a large amount of residue carbon, the resistivity of FEBID-Pt is expected to be much higher than the resistivity of metallic Pt, which is in the order of $10^{-1}\Omega\mathrm{mm}^2/\mathrm{m}$. The test bars were deposited with the electron beam at an acceleration voltage of 5 kV and a beam current of 2.7 nA and had a width of 5μm, 10μm, and 15μm. To investigate the option of decreasing the deposition time, the bars were deposited with both a pitch distance of 7.12 nm and 22 nm. The former is the default setting for a 0% beam overlap between pixels while the latter is artifically increased to speed up the process. From just SEM observation, both settings produce closed thin films. For a pitch distance of 7.12 nm the film height was measured as 250 nm, whereas the film with a pitch distance of 22 nm was only 85 nm high for the same z-size setting. Thus, it is beneficial to use the larger pitch distance of 22 nm to cover large areas with a thin Pt layer, as the deposition time compared to the setting with a pitch of 7.12 nm is 9 times shorter. For a 60 μm square area, the process still takes several hours even at 22 nm pitch distance.

The resistivity was calculated from the measured I-U-curves and the dimensions measured with the SEM. For a pitch distance of 7.12 nm the resistivity is $\rho_{7.12} = 762.5\,\Omega\text{mm}^2/\text{m}$, but with a pitch distance of 22 nm the resistivity increases to $\rho_{22} = 18370.6\,\Omega\text{mm}^2/\text{m}$. These values are three to five orders of magnitude larger than for metallic Pt films, but even ρ_{22} is still an order of magnitude smaller than the resistivity of the conductive lacquer. Since one of the main concerns with the lacquer was the thermal stability, FEBID-Pt with a pitch distance of 22 nm could be a suitable matrix material. While the value of $\rho_{7.12}$ is also suitable, and possibly better, the former setting was chosen for time efficiency reasons. It is worth noting, that for consecutive measurements of the resistivity over the course of two weeks, the conductivity of the FEBID-Pt layer with a pitch of 7.12 nm actually increased. This is most likely due to partial melting of the Pt grains because of Joule heating and thus the formation of a more homogeneous Pt layer. As Pt thin films tend to grow in islands, the density of Pt in the films with a pitch of 22 nm was probably not sufficient to form a continuous film and therefore an improved conductivity over time was not observed.

4.4.3 Results for FEBID-Co particles

For the bottom-up devices made of Co nanoparticles that were directly written onto the substrate by focused electron beam induced deposition a series of samples was prepared as explained in chapter 4.4.1. The particles were patterned with an acceleration voltage of 3 kV, a beam current of 0.34 nA, and a pitch distance of 80 nm. After unsuccessful samples with conductive PMMA lacquer (AR-PC 5090) and conductive Ag adhesive, several samples were prepared using FEBID-Pt as a matrix layer, since it was the most promising of the tested materials. Even when the device size was shrunk to 5 μm to reduce the total resistance, no magnetoresistive effect above the noise level could be measured.
Given the measurements for FEBID-Pt, the Co particles likely have a specific resistivity in the order of $\rho = 10^3\,\Omega\text{mm}^2/\text{m}$ to $\rho = 10^5\,\Omega\text{mm}^2/\text{m}$. Combined with the bad conductance of the matrix material, any resistance change caused by spin-dependent scattering at the particle interfaces is likely negligible compared to the total device resistance. It is also not possible to solve this problem by using a better conductor as the matrix material since the particles would be shunted. Furthermore, the magnetic moment of the FEBID-Co particles is probably relatively low and the particles contain many carbon impurities. This might lead to an overall lower spin polarization than in a comparable thin film. Lastly, because of deposition artifacts, the distance between particles is probably larger than the spin diffusion length l_{sf}. Although the value of l_{sf} for FEBID-Pt is not known, it is a reasonable assumption that a low conductance material can only preserve spins over a relatively short distance. Thus, the viability of ordered granular GMR devices that are fabricated with direct write FEBID nanoparticles could not be proven.

4.4.4 Results for nanopatterned Py thin films

The top-down granular GMR devices were prepared by using the FIB to mill trenches into a 30 nm Py film to create isolated particles. In order to investigate the influence of the particle shape on the GMR response, rectangular grids with different aspect ratios of 2:1, 3:1, 5:1, 7:1, and 9:1 were fabricated. The short side of the rectangle was kept at 250 nm to prevent the melting of particles as described in chapter

4.3.2. Additionally, grids with a mix of two different aspect ratios were fabricated, by shifting every second horizontal line by a small distance. The idea was to obtain different particles with different coercive fields in one structure to create a more stable antiparallel state of the GMR. Figure 4.15 shows a patterned Py film with a rectangular 9:1 grid between gold contact pads before the FEBID-Pt layer was deposited on top as the matrix material. The pattern was chosen larger than the film to ensure fully isolated particles and no shunting through the sides of the device.

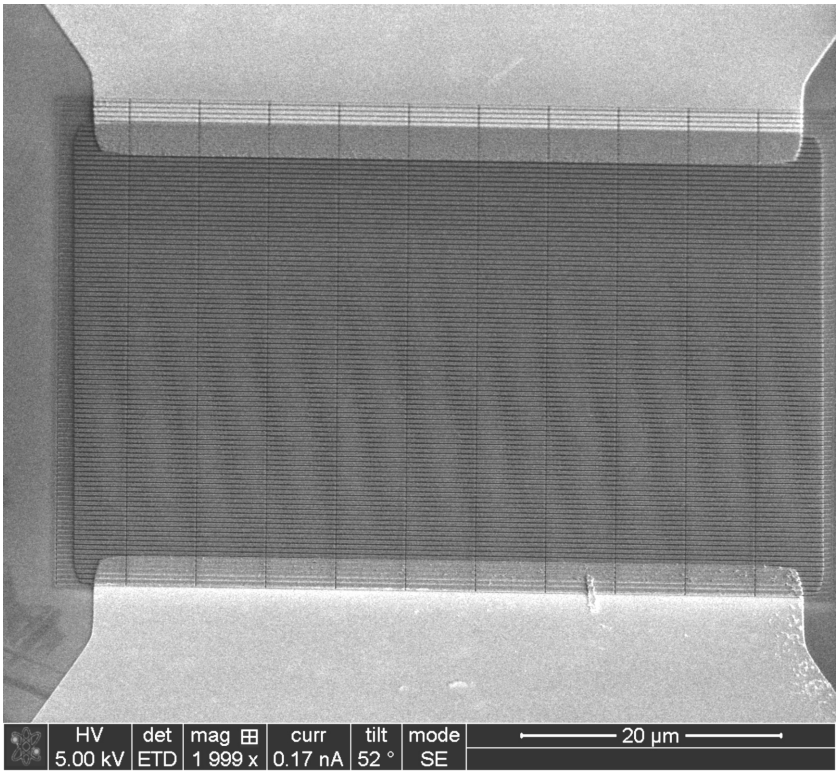

Figure 4.15: SEM image of a nanopatterned rectangular 60 μm x 60 μm Py grid with Au contact pads at the top and bottom at a tilt of 52 ° with regard to the SEM column. The Py thickness was 30 nm and the milling depth was set to 70 nm to ensure isolated structures.

Before the transport measurements, a thin Pt film with a thickness of roughly 50 nm was deposited on top of the grid with a pitch distance of 22 nm. Similar to the experiments with FEBID-Co particles, transport measurements showed no GMR above noise level for any of the prepared samples. In case of the samples with larger particles however, a small AMR could be measured. Since AMR is a bulk phenomenon this originates from transport through the larger particles, but no effect of spin dependent scattering at the interfaces that is large enough to measure a GMR could be found. The reasons for this are likely similar to the problems with the FEBID-Co structures, except that the particles here have a much better conductivity as they are created from a sputtered metallic thin film. Through observation of AMR in the measurements, it can be confirmed though, that the current does indeed travel through the particles instead of being shunted by the matrix material. The total device resistance is still in the kΩ range since the matrix material is a bad conductor. Additionally, the distance between particles is quite

large due to the limitations of the ion beam milling resolution. This means that even if the conductivity was higher, a large GMR would likely not be measured as the gap between the particles is larger than the expected spin diffusion length in FEBID-Co. As it was discussed previously, the choice of the right matrix material is critically important for this kind of device. A lower conductivity than the particle material and a selective application of the material in just the gaps between the particles would be desirable, but difficult to achieve from a process engineering point of view. Additionally, a relatively high spin diffusion length is needed, which is not a well-explored field of research for compound materials like FEBID-Co or -Pt.

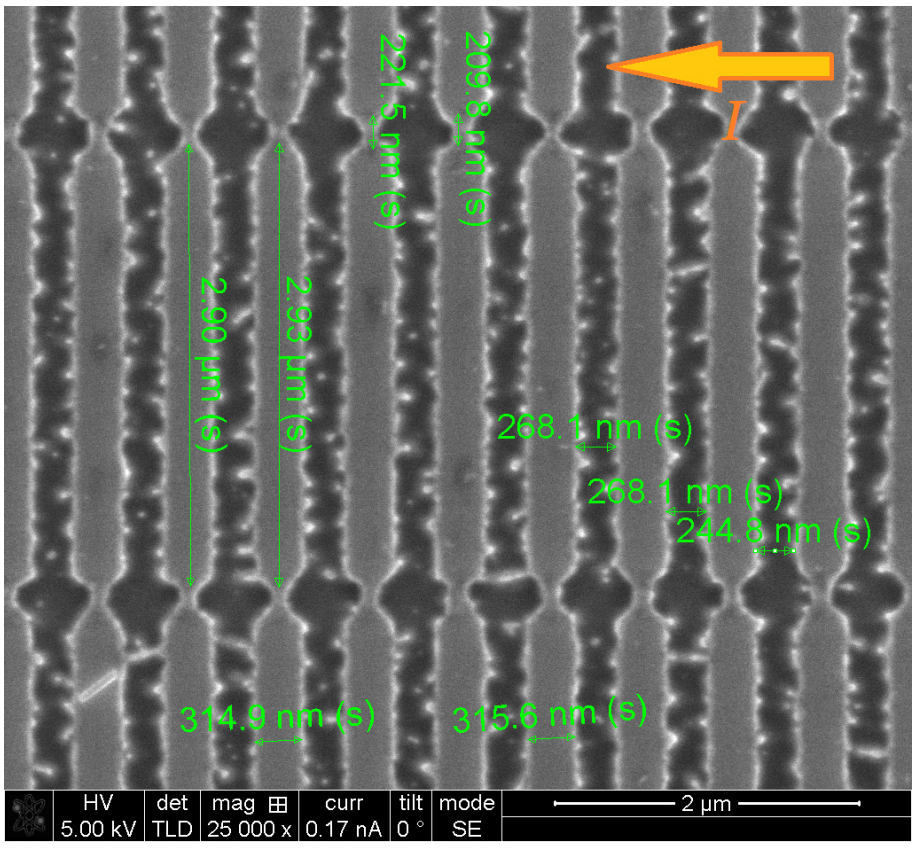

Figure 4.16: SEM image of a line grid with many artifacts created by a stage drift. The large gaps were supposed to be patterned as two individual lines, but being too close to each other the material between the lines partly melted.

During the preparation process with the focused ion beam a lot of energy is transferred to the thin film. Especially for small structures, the heat conduction through the substrate can be insufficient and the local film temperature rises drastically during milling. Figure 4.16 shows an example of such artifacts that are introduced when the distance between adjacent lines in the grid falls below roughly $d_{\mathrm{grid}} = 180\,\mathrm{nm}$. In this sample, the objective was to create a rectangular grid of $3\,\mu\mathrm{m}$ particle width and two different heights of 350 nm and 150 nm with regard to the current. As the line spacing for the latter was too narrow, the material between the lines completely melted and redeposited itself on the larger particle or in the gaps. This results in many small granules and little antennae of material in the now far too large ver-

tical gaps. The horizontal gaps between the particles were in most cases closed completely. While this structure looks broken and highly undesirable for a GMR application because of the large gaps at first glance, the small granules of melted material in the gaps offer an interesting possibility. Because all samples with cleanly cut trenches did not produce a GMR and a limiting factor is the milling resolution of the ion beam, the particles can be used to bridge the gap. As the thin film consisted mostly of Py with a small Ru capping layer, the particles are assumed to still be ferromagnetic. Although the redeposited material is distributed randomly, over a large enough sample these artifacts shorten the effective gap between the particles. Thus, the small granules as a result of a local overheating of the thin film make these structures interesting for a possible GMR application, as they solve one of the fundamental problems of the other samples.

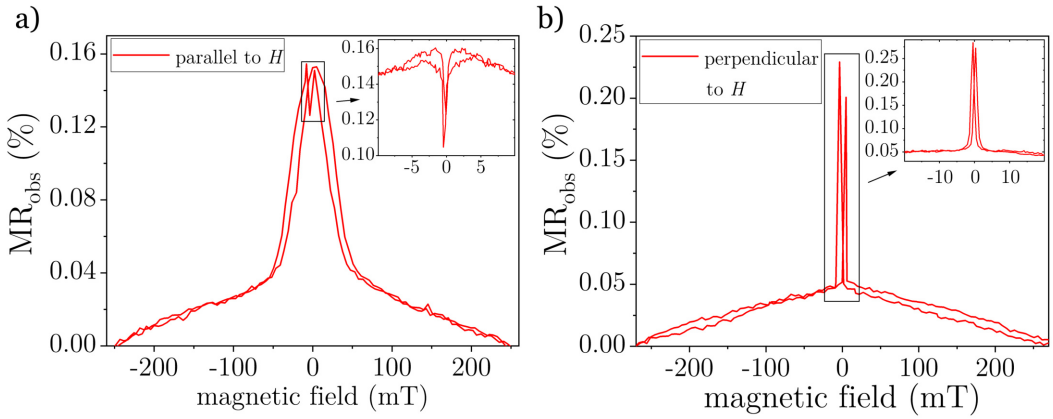

Figure 4.17: GMR measurements in two-point geometry performed on a structure with a strong occurrence of artifacts as seen in 4.16. a) Observed MR ratio with the current parallel to the external field and b) with the current perpendicular to the external field. Insets in each graph zoom in on the zero field region marked by the black box to show that AMR is superimposed on the GMR curve.

Figure 4.17 shows transport measurements from a sample with this magnetic "gravel" in the gaps between the larger particles for both a) current parallel to the external field H and b) current perpendicular to the external field H. In the parallel measurement (Fig. 4.17 a)) the characteristic Gaussian-like shape of the GMR curve is clearly visible against the background and the switching field is at around 25 mT. Although the amplitude of the effect is very low at 0.16 %, the noise is relatively low. At such small MR ratios, the GMR can be easily confused with the AMR, but a second measurement around $H = 0$ reveals that the AMR is in fact superimposed with the GMR curve and produces a small dip in the MR ratio around $H = 0$. The perpendicular measurement (Fig. 4.17 b)) for these samples is far more narrow than the perpendicular measurement even when measured at a higher resolution in the inset. In fact, without the parallel measurement to confirm the existence of GMR, this measurement could be easily mistaken for a simple AMR signal because of the low amplitude. Upon closer inspection though, the amplitude in the perpendicular measurement at 0.23 % is actually higher than the peak of the GMR curve in the parallel configuration at 0.16 %. The difference in MR ratio can be explained by

considering the dependence of the AMR on the angle between the current and the magnetization. Since the AMR changes its sign when the field direction is turned by 90°, the dip from the parallel measurement is actually added to the peak GMR in the perpendicular measurement geometry. This explains the difference in MR ratio of 0.12 % , when the more accurate values from the insets are considered, to a large extent.
The width of both curves, i.e. the different switching fields for the particles, can be explained by taking a close look at the particle geometry from Figure 4.16. As the structures are mostly continuous albeit not particularly smooth bars instead of particles, the individual structures have a high aspect ratio. This leads to a high shape anisotropy in the bars and thus an easy magnetization axis along the length of the bars [55]. A continuous thin film does not have a preferred axis of magnetization as long as no other anisotropy like magnetocrystalline anisotropy or a peculiar ordered microstructure is considered. Therefore, the demagnetization field along the easy axis of the observed bar structures should closely resemble that of a thin film, whereas the demagnetization field along the hard, i.e. short, axis of the bar will be higher. This behavior is qualitatively visible in the measured data. The typical coercive field for thin continuous thin films of Py is between $H_{\mathrm{C,Py}} = 0.5{-}2\,\mathrm{mT}$ which agrees well with the measured data of about 1-1.5 mT [56]. Along the hard axis the switching occurs at around 25 mT, which is a large difference owed to the high aspect ratio of the patterned bar structure. In theory, the small magnetic granules, which include a few rod-shaped structures perpendicular to the larger bars, could have their own easy axis in the current parallel to the external field configuration. However, since these smaller particles make up only a small fraction of the total magnetic volume, this is not reflected in the actual data. To put the comparatively low MR ratio between 0.16 % and 0.27 % into context it is worth looking at the absolute device resistance, which is quite high at $3583.81\,\Omega$. The total resistance change $\Delta R = 8.61\,\Omega$ would be enormous, if it occurred in a metallic GMR device with a total resistance of only a few Ohm. Thus, the idea of ordered granular GMR structures is viable in principle, but hard to implement with the presented methods due to manufacturing limitations.

4.5 Summary and Outlook

As part of this work, the flexibility of dual beam techniques and direct write lithography could be demonstrated. While the preparation of large quantities of samples is quite time-consuming, especially in the case of focused electron beam induced deposition of Co and Pt, on a small scale these methods can provide unique results. With a particle size of 40-50 nm and a particle spacing of less than 20 nm with the appropriate deposition conditions, FEBID exceeds the resolution of most conventional lithography processes and is only beaten by specialized development techniques for extremely thin films or large scale industrial machines used for example for CPU production. Additionally, the sample can be directly observed, which offers immense flexibility and precision in a laboratory setting. Similarly, high resolution milling with the focused ion beam can produce densely packed nanostructures with a minimal milling width of about 30-40 nm.
Using the developed scripting and stitching routines it was possible to create nanotextured sensor devices on Py thin films with high precision over a large area, as well as large arrays of several hundred thousand Co nanoparticles. While this work is focused on nanoparticle arrays, the basic framework of the used scripts can be easily

adapted to other applications and designs. Since the quality of these structures is highly dependent on good focus and astigmatism settings for the patterning beam, the machine cannot work fully autonomous though. As a preliminary work to the actual sensor project, it was shown that materials prepared by focused ion beam induced deposition had unique microstructure and electrical transport properties. At the same time, it was possible to create ferromagnetic nanostructures in spite of the high amount of carbon residue from the precursor molecule. Therefore, while the production of nanotextured materials is still challenging and expensive in terms of machine time and work hours, the benefits offered by nanostructured materials are not yet fully explored and deserve some attention. For prototyping and small scale serialization, the focused ion beam device offers great utility, as structures can be modified on the spot and the samples can be directly characterized using the SEM and energy dispersive X-ray spectroscopy (EDX) in the machine. This accelerates the work flow compared to resist based lithography. Additionally, the powerful analytical tools in a dual beam microscope can be highly desirable for quality assurance purposes in industrial applications.

With regard to the preparation of highly ordered granular GMR sensors, not all of the proposed designs could be successfully implemented. Due to conductivity and patterning resolution limitations, the Co nanoparticles deposited by FEBID could not successfully be integrated into a GMR sensor. However, by top-down fabrication of magnetic particles from a Py thin film by focused ion beam milling, a working GMR device could be realized. The main difficulties in this approach were the limited milling resolution and the targeted application of viable matrix materials. As a result, only devices with milling artifacts that partly narrowed the gap between individual particles showed a small GMR. Additionally, while the resistance chance $\Delta R = 8.61\,\Omega$ was quite remarkable, the low conductivity of the matrix material meant that the observed MR ratio was below 1 %. In general, these devices offer no advantage over similar thin film GMR sensors that are also easier to manufacture. In order to improve the given sensors a better filling material and a higher patterning resolution are required. The latter could be achieved by using a sputtered hard mask to etch the trenches more precisely.

Given the promising simulations from [39] and the results from nanoparticle based GMR sensors in gel matrices from [1], I believe that the approach to create ordered granular magnetoresistive sensors presented in this work can be improved upon. The present findings on nanopatterned Py GMR sensors, while limited in viable applications for commercial use, act as a proof of concept for future sensor projects. As an alternative, densely packed structures of chemically prepared nanoparticles could be used, since free particles can be stacked directly on top of one another without any limitations by the fabrication process. The thin organic shell of such particles would act as a tunnel barrier so that instead of a GMR the tunnel magnetoresistance effect TMR is measured. Yakushiji *et. al.* reported spin-dependent tunneling in tunnel junctions with a single ferromagnetic nanoparticle, which act like magnetic single electron transistors [57]. Thus, the abstraction to larger tunneling sensors based on ferromagnetic nanoparticles seems viable. As particles with an organic shell can also be functionalized to selectively bind to other molecules or materials, the option to create highly ordered dense structures of ferromagnetic particles for sensor applications in this way is worth exploring.

5 Preparation of high-precision optical components for super-resolution microscopy

When Abbe published his famous considerations on the resolution limit of light microscopes, which have been a staple work horse in all fields of science for centuries, he could only dream about the tremendous advances beyond that limit that would happen in the 150 years after his discovery [58]. Even though electron microscopes have long since surpassed light microscopes in terms of maximum resolution, making it possible to observe even single atoms, light microscopy is still an essential tool, especially when observing biological samples. As electron microscopes require a vacuum to operate, it is impossible to observe specimens in vivo, which is one of the biggest advantages of light microscopy. In recent years, several laser fluorescence microscopy techniques for biological samples have been developed that break Abbe's diffraction barrier by a considerable margin.
In stimulated emission depletion (STED) microscopy for example, the exciting beam is superimposed with a second ring-shaped quenching beam that depletes the excited fluorophore states, which results in a smaller focal volume and thus more precise imaging. A different approach is to statistically switch off certain fluorophores so only a low amount of emitters, that can be well separated, is active at a time. Combining several images taken over a period of time then also yields a super resolution image. This technique is either called photoactivated localization microscopy (PALM) or stochastic optical reconstruction microscopy (STORM) and both discoveries were awarded a joint Nobel prize in chemistry in 2014 to Eric Betzig, Stefan Hell, and William E. Moerner [59]. A third, more computationally intensive, super-resolution microscopy technique is structured illumination microscopy (SIM), where the specimen is illuminated by a grid and a combination of several images is used to reconstruct a super-resolved micrograph of the specimen by deconvolution.
All of these techniques require careful calibration and can yet be improved by correcting systematic errors like lense aberrations. This chapter will outline the development and production of a nanoscale optical device by dual beam and lithography methods that was specifically designed to improve the emitter localization of STORM. However, the device can in principle also be used as a calibration sample for other microscopy techniques.

5.1 Challenges in super resolution STORM microscopy

One of the main challenges in conventional fluorescence microscopy is to distinguish densely packed emitters in a specimen due to the Abbe limit, which means that even a point light source appears as an object with finite size because of diffraction in the microscope optics [58]. The intensity profile of such a spot defines the point spread function (PSF) of the microscope. Given a typical microscope with circular aperture, the point spread function would take the shape of a so-called Airy disc, which in a 2D projection is a circular central spot with concentric rings around it. Unlike lens aberrations like chromatic aberration due to light dispersion or spherical aberration, even an ideal lens produces these Airy discs. The minimum distance to clearly separate two emitters is usually considered to be the full width half maximum (FWHM) of the central peak of the PSF, which is approximated by $\Delta x = \lambda/(2\mathrm{NA})$ where λ is the wavelength of the light and $\mathrm{NA} = n\sin(\alpha)$ is the numerical aperture with the refractive index of the material n and the opening angle of the lens α [60]. For visible light of roughly $\lambda \approx 510\,\mathrm{nm}$, which corresponds to the emission of the

popular fluorescence marker GFP (green fluorescent protein), even using high NA lenses with an NA of about 1.4, the resolution is limited by the size of the PSF to about 200 nm laterally.
If a fluorophore is well isolated from other emitters though, it is possible to determine its location with far higher accuracy than the diffraction limit by finding the center point of the PSFs peak. This is done by fitting the image to find the peak centroid and is only limited by the number of photons collected, with more photons yielding a more precise result as the signal becomes smoother. For single fluorophore molecules under ambient conditions Yildiz *et. al.* were able to determine the emitters location with a precision of up to $\sim 1.5\,\mathrm{nm}$ [61]. Such precision can only be translated into better imaging resolution however, when fluorophores are spread out. As soon as the point spread functions of adjacent fluorescent molecules overlap, determining the location precisely becomes difficult. In the case of biological samples a single diffraction limited region can contain hundreds of fluorophores [62]. In stochastic optical reconstruction microscopy (STORM) optically switchable fluorophores are used so that the number of active emitters at any given time is low enough to precisely determine the fluorescent molecules' location. By combining several such images, all fluorophores will be active and detected at some point and a super-resolution image with the centroids of the respective PSFs can be reconstructed. This concept is illustrated by a sketch in Figure 5.1.

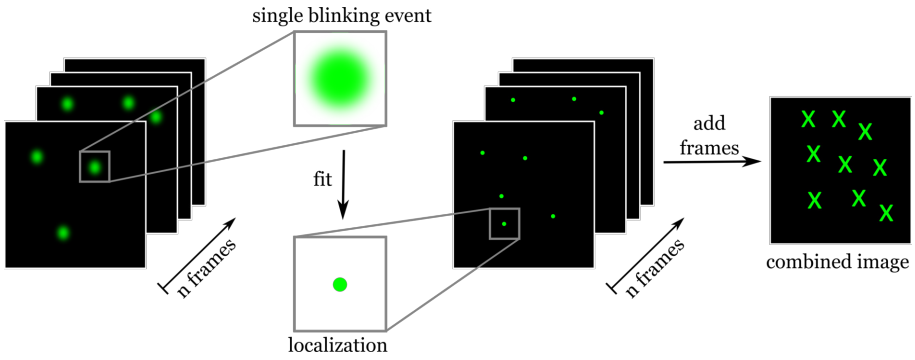

Figure 5.1: Sketch illustrating the working principle of STORM microscopy. A stack of n diffraction limited wide field images will be recorded. STORM uses switchable fluorophores that do not emit light at all times so that single fluorophores are easy to identify. The blinking events are fitted with a function appropriate for the used point spread function, in this example a 2D Gaussian function, to estimate the center of the emitter. Multiple images are superimposed to create a single superresolution image. Here the x-shaped structures are only revealed in the combined image. The total number of frames n can be greater than ten thousand.

Since not all fluorescent molecules can be switched to and from an inactive state, the selection of usable fluorescent markers in STORM is limited. However, in recent years many research groups have found ways to create photoswitchable or photoactivatable proteins and synthetic dyes [62]. A prominent example of photoswitchable dye is the Cyanine dye, which has several variants with emission and absorption at different wavelengths. The red cyanine dye Cy5 can be reversibly converted between a fluorescent and an inactive state by irradiation with an external light source. When

a Cy5 molecule is exposed to red light (649 nm) it is fluorescent before switching to a stable dark state. In an ensemble, a significant fraction of dark state Cy5 can be reactivated and return to the fluorescent state by UV irradiation. The details of this reactivation process such as the activation wavelength are dependent on the presence of other chemicals or the proximity of other fluorophores such as Cy3 [63].

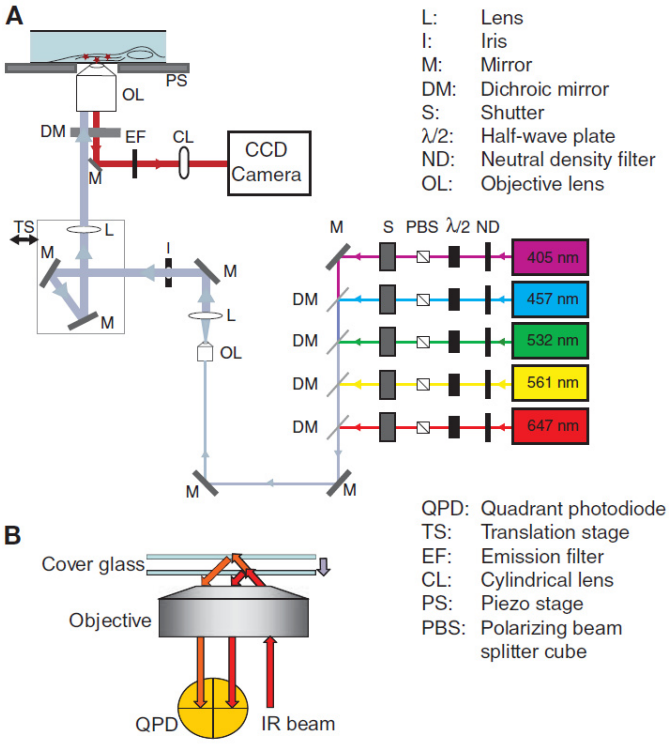

Figure 5.2: A) Schematic sketch of a STORM microscope based on an inverted fluorescence microscope. The laser sources are combined into a single beam, which is expanded and focused to the back focal plane of the microscope objective. A translation stage allows for adjustment of the incident angle. The detected light passes through an emission filter and is imaged onto a CCD camera. The wavelengths shown are just an example of activation and imaging wavelengths and are adjusted for the specific application. The cylindrical lens (CL) is only used for astigmatic imaging in 3D STORM applications. B) The geometry of the focus lock system. An infrared (IR) laser is projected through the objective lens from a second dichroic mirror (not shown in A). The beam reflects off the sample-cover-glass interface and detected on a quadrant photodiode (QPD) to detect the position. Reprinted with permission from Cold Spring Harbor Laboratory Press from [62].

The image acquisition for STORM is comparatively simple and, broadly speaking, uses a conventional wide-field fluorescence microscope as a base. To produce convincing results, a few modifications need to be made. Though it is not a necessity, it is convenient to use an inverted fluorescence microscope frame that is commercially available, since they provide a stable mount for the sample and any additional components that might be added to the setup. A sketch of such a setup is found

in Figure 5.2 A. Additionally, many such microscopes already have built-in mechanisms for stage stabilization, vibration compensation or drift corrections. This is particularly important because STORM requires a series of images that are gathered over a period of time and only combined in post-production. Thus, drift needs to be minimized during image acquisition, as it can be troublesome to completely correct for mechanical and/or thermal drift in post production.
Good thermal insulation can also help to mitigate drift during a measurement. A reliable way to detect relative movement between the sample and objective lens is the focus-lock technique illustrated in Figure 5.2 B, where a weak infrared laser irradiates the sample through a dichroic mirror and reflects off the sample-cover-glass interface. The reflected beam is then projected back through the objective lens onto a quadrant photo diode (QPD) to detect its position. Any change in the position can be detected and automatically adjusted by piezoelectric actuators [63]. Immobile fluorescent elements such as fixated nanoparticles, so-called "fiducial markers", can also be used as anchors to reliably track and correct for drift [64, 65]. The same technique can also be used to record and follow movements of specific fluorescent molecules like diffusion processes or to monitor processes in living cells. For cell imaging, a through-the-objective illumination geometry is convenient, as the cell can be imaged from underneath directly through the culture plate and therefore remain in solution [62].
Different light sources for the used fluorescent dyes and their activation are combined into a single beam through dichroic mirrors. The emitted fluorescence signal from the sample also passes a dichroic mirror and an emission filter before being detected on a CCD camera. Since single fluorophores need to be detected, the CCD must be suitable for low-light fluorescence imaging. To increase the efficiency of the image collection, the laser exposure times for activation and exposure of the fluorophores are timed to be synchronous to the frame rate of the camera. In a multi-color application, as shown in Figure 5.2, the individual colors are activated in sequence using the activation wavelength to distinguish different photoswitchable fluorophores. Any unintentional activation of a fluorophore results in cross-talk between the color channels and artifacts in the final image. This can occur, for example, when the imaging laser frequency band overlaps with the activation laser emission band of another dye. An incorrectly activated fluorophore can be identified if the switching event was detected in a frame that does not immediately follow an activation pulse. Typical cross-talk levels are in the order of 10-30 % and can be corrected statistically in the image processing stage [62].

5.1.1 Alignment procedures in multi-color fluorescence imaging

Besides the general considerations on STORM in the previous chapter, multi-color imaging methods require additional corrections to those dealing with drift for example. For different color channels, there is a static but spatially dependent chromatic offset that results in unreliable localization of the fluorophores and thus potential misinterpretations of the measured data. Although the chromatic offset in well-corrected optics is small ($\sim 50\,\mathrm{nm}$) compared to the optical wavelength and therefore negligible in diffraction limited microscopy, it can lead to significant errors when the high precision of single fluorophore localization is considered. To measure this chromatic offset, Erdelyi *et. al.* imaged multicolored fluorescent beads with a concentration sufficiently low to detect single beads [66]. For a given single bead, a stack of 800 images was captured with 200 frames each at excitation wavelengths of

641, 561, 491, and 641 nm. The first and last images were captured using the same wavelength to estimate and correct for mechanical drift that is superimposed on the chromatic offset. Since the beads emit a bright fluorescence signal, the localization precision of these measurements was 3-4 nm, which ensures a precise calibration, as real localization microscopy data has a precision of about 10-30 nm. Using the 641 nm excitation as a reference, the displacement of the 561 nm and 491 nm excitations can be determined.

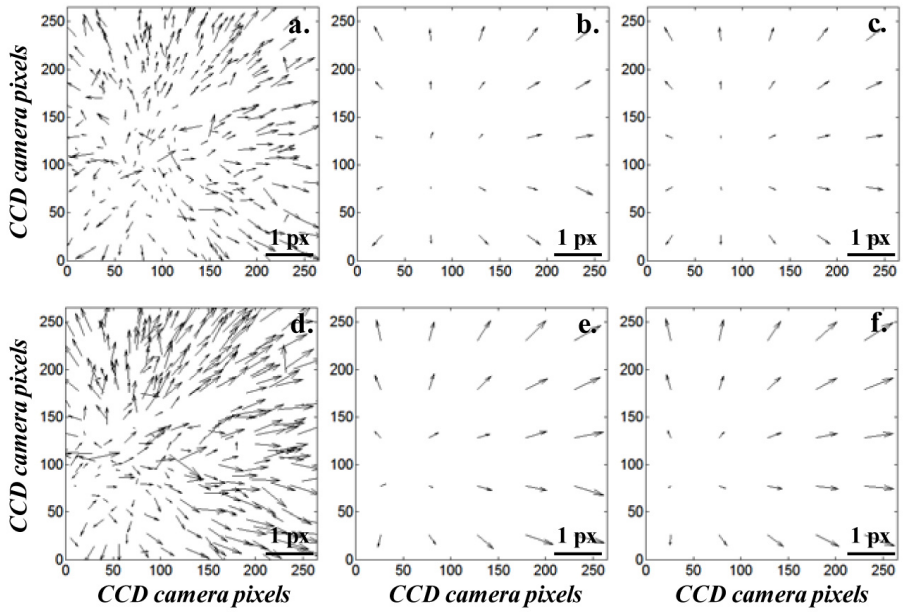

Figure 5.3: Spatial dependence of optical offset between channels using excitation wavelengths of 641 nm/561 nm (a,b,c) and 641 nm/491 nm (d,e,f). (a,d) show raw data, which is averaged over four sequential frames in (b,e). A polynomial fit was used in (c,f) to achieve a smooth distribution of the optical offset at an arbitrary point on the CCD detector. The scale bar represents optical offset in camera pixels. Reprinted with permission from [66] (Open Access).

Figure 5.3 shows the measured offsets of the 641 nm/ 561 nm pair (a) and the 641 nm/ 491 nm pair (d) as a function of the position in the field of view (FOV) on the camera's CCD chip. The scale bar represents a displacement of one pixel with the arrows indicating both direction and magnitude of the displacement. Figure 5.3 (b,e) show the respective dataset averaged of four sequential frames to eliminate statistical errors and (c,f) additionally used a polynomial fit to smoothen the displacement map. These displacements correspond to an error of about 30-45 nm, which is a large error considering small vesicles in a cell can be of similar size [66]. Other works using a similar experimental setup measured displacements of up to 100 nm before correction [67]. Based on this measure displacement map, a transformation matrix can be generated that corrects the offset for each voxel in the FOV. Such a correction protocol can significantly increase the localization precision in post-production.

5.1.2 The point spread function and 3D-imaging

As discussed in chapter 5.1, the point spread function (PSF) is the typical response of an imaging system to a point light source. This means that the imaged object will not appear point-like, but instead as an extended object with a geometry dependent on the optical components like lenses between the emitter and the detector. For typical lenses with round apertures the point spread function in two dimensions takes the shape of an Airy disc, which is essentially a circular center point surrounded by concentric rings. When the emitter is perfectly in focus, the Airy disc is quite small and the intensity of the rings is low. If the emitter is above or below the focal plane however, the shape of the PSF changes, and the rings become wider and more clearly visible. In three dimensions this standard PSF is almost dumbbell-shaped. For 3D STORM imaging, the shape of the PSF can be used to not only determine the center of the emitter but also obtain information on the depth of the object by considering the extent of the defocusing. With a standard PSF, the depth of field is relatively shallow at about 500 nm and the fact, that the Airy function is symmetrical complicates the determination of the fluorophores position in the axial direction. Early 3D systems involved a cylindrical lens that creates slightly different focal planes for the x- and y-direction, so that the emitter can be located by the ellipticity of the PSF [62]. Ideally, a high asymmetry in the axial direction and a large depth of field are desired to achieve high precision localization of single fluorophoes in all directions.

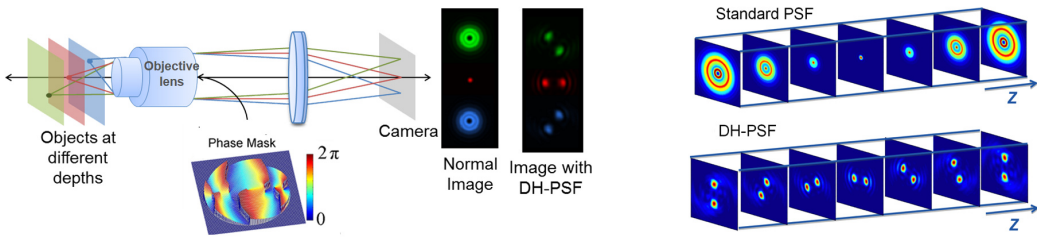

Figure 5.4: Illustration of point spread function (PSF) engineering using tailored phase masks to alter the beam shape. The standard Airy-function PSF changes symmetrically for objects above and below the focal plane while the double helix PSF rotates in different directions. Image provided courtesy of Double Helix Optics LLC.

By using a 4f-relay, it is possible to place a phase mask in the Fourier plane between the two lenses in the detection path and alter the shape of the point spread function. The fabrication of a phase mask is done by a multi-level lithography process to etch the desired pattern into a glass slide. Since light propagation inside a medium is dependent on the refractive index, different glass thicknesses along the beam path will retard parts of the beam. Thus, the beam takes the desired shape. The difficult part is determining which pattern is needed to achieve the right PSF shape. Wang *et. al.* used a Gauss-Newton algorithm to reverse engineer the phase mask for a previously reported point spread function and fabricated proof of concept phase masks to verify the results [68]. Figure 5.4 illustrates the benefit of using a phase mask by comparing the point spread functions with and without a mask in different axial planes. In this example the commercially available double helix phase

mask is used to create a double helix PSF with two lobes that rotate clockwise or counterclockwise depending on their position relative to the focal plane. These lobes stay sharp even with a high degree of defocus and allow for precise localization of an emitter in the axial direction with a depth of field of several microns[68, 69].
In principle, any asymmetric PSF can be used for 3D STORM imaging. However, the localization in the xy-plane still needs to be considered for optimal results. Normally, a computer would for example determine the center of the Airy disc, by fitting a two-dimensional Gaussian to the signal and calculating the center point. With a double Helix PSF however, that script needs to be changed to essentially calculate the center of gravity between the two lobes. The real algorithm of course, is a lot more complicated. To maximize the localization precision a depth-variant approach for 3D phase retrieval (PR) was chosen. The obtained information about the optical system from experiments and the PR process is then utilized in the 3D maximum likelihood localization estimation. Using its knowledge about the PSF, the estimator program compares the experimental images to find the most likely PSF match. A detailed explanation of the process can be found in the work of Quirin *et. al.* [70] and its supplementary information. In their work, they managed to localize a single fluorophore in a $17\,\mathrm{nm} \times 10\,\mathrm{nm} \times 19\,\mathrm{nm}$ volume. With these techniques in mind, it is now possible to examine the requirements to a calibration sample that can be used, among other things, for multi-color alignment in 3D STORM.

5.1.3 Nanotextured calibration samples

The alignment procedures using multi-fluorescent beads used for multi-color alignment in [66] and [67] are very effective, but still have a few systematic problems. Since only the relative offset to a reference fluorescence signal (641 nm in the given example) is considered, the possibility of a warped image in the reference is unaccounted for. Since all color channels are subject to aberrations, it is reasonable to assume that the reference signal itself has errors depending on the position of the emitter in the field of view. Using fluorescent beads, this is impossible to correct, since the beads are randomly distributed on the microscope slide, so the ground truth of the bead spacing can not be measured. Furthermore, due to the intrinsic randomness of the bead distribution, it can be challenging to find a field of view that is actually suitable for the calibration process. Clusters of beads, which are likely to form at high bead concentrations, produce a fluorescence signal that is too broad and can lead to errors. Ideally, a field of view with evenly spaced single beads is desired for this process. Alternatively, a single isolated bead can be moved across the field of view. The accuracy of the calibration is then limited by the accuracy of the movement.
To solve these problems, an evenly spaced grid of immobilized single emitters is desirable. These emitters should be placed on a perfectly flat surface so that any rotation in the double helix PSF can be attributed to a tilt or warp in the cover slide. Such a 2D grid can not help to correct aberrations in the axial direction, which could be caused by an index of refraction mismatch of the glass slide, immersion oil, and for example the buffer solution of any biological sample on the microscope. However, since the size, shape, and spacing of the emitters in the grid is always well known and can be verified by other means like electron microscopy, a multi-color calibration done in this manner can be more precise than the bead approach and correct aberrations in the reference signal on top of that.

5.2 Nano hole aperture (NHA) prototyping and production

With the above considerations in mind, an alignment grid can be manufactured from metallic thin films on a precision glass slide by either FIB milling or lithography. The most important criteria are reproducible aperture size and precise spacing of the apertures. Additionally, the holes should have a low ellipticity to affect the shape of the PSF as little as possible. This is especially critical for 3D STORM since the axial position is determined from the rotation of the PSF. This chapter will explore both FIB and lithography methods for manufacturing precise nano hole aperture grids and focus on the optimization of the fabrication work flow to achieve consistently high-quality results.

5.2.1 NHA Design

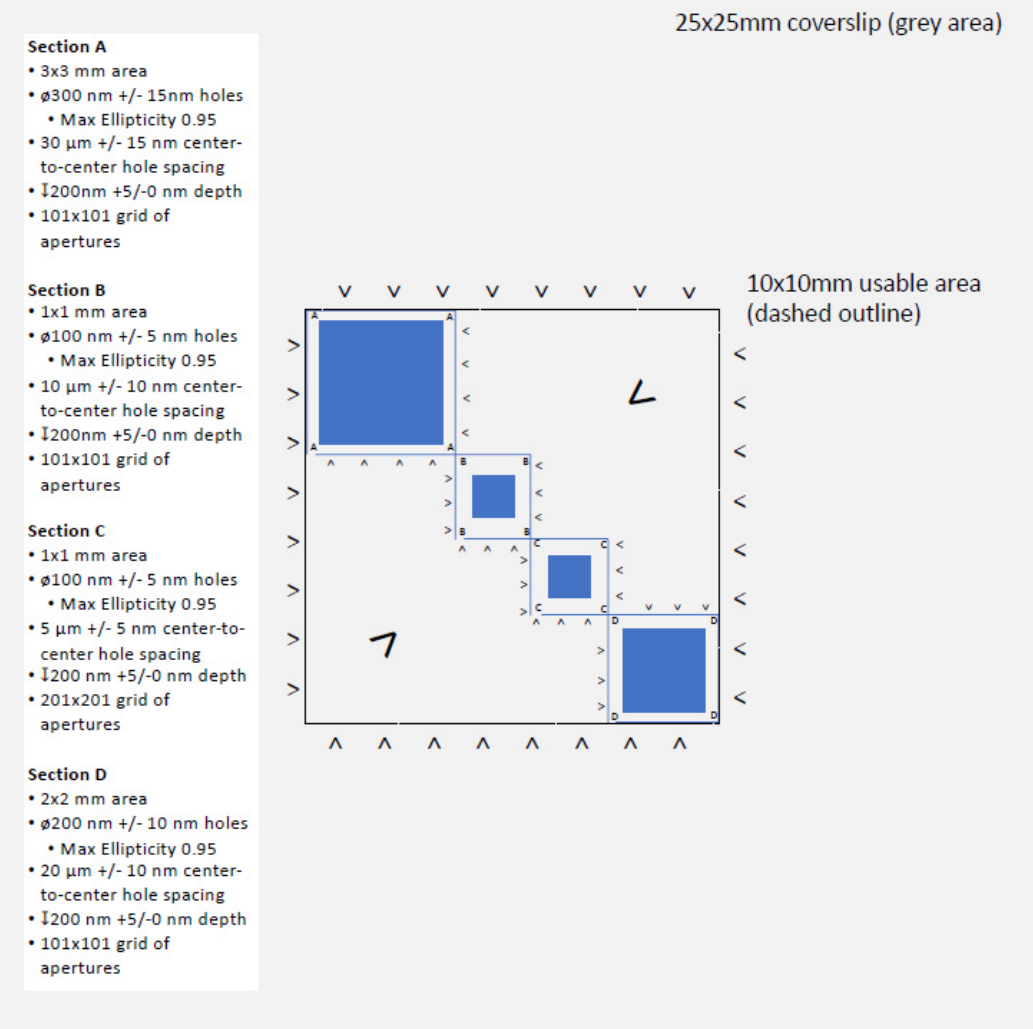

Figure 5.5: Overview of the NHA design. Frames and arrows around each hole grid are 5 μm wide. Hole sizes and spacing vary across the diagonal in order to accommodate varying NA and magnification. Image provided courtesy of Double Helix Optics LLC.

From a pure functionality point of view, it would be sufficient to prepare a microscope slide with an opaque metal coating and a regular cubic grid of apertures at the center. Even for a large grid consisting of several thousand holes, it can be quite hard to locate on a 22 mm x 22 mm microscope slide inside a fluorescence microscope with a limited field of view. Therefore, it is helpful to also add a set of finding lines or frames around the grid to provide an easier user experience. These lines should be far enough from the actual holes, so that no stray light from the lines is collected during imaging of the grid. While the initial design included little more than a square "crosshair"-like structure around a single square grid of 100 nm holes, the final design provided by Double Helix Optics LLC that is presented in Figure 5.5 is much more elaborate.
The nanohole aperture (NHA) slide consists of four main working areas on the main diagonal of the microscope slide that is each framed by an individual box and a letter designating the grid type. Section A contains 300 nm spherical holes with a 30 μm spacing. The two central grids B and C both consist of 100 nm holes at a 10 μm and 5 μm spacing respectively. The final area D has holes of 200 nm size at a 20 μm spacing. All grids are surrounded by a large box and around the outside of each frame, a set of V-shaped arrows points to the sample center to make navigation easier. The empty off diagonals each contain a large arrow for navigation. The different hole sizes and spacings accommodate for a wide range of magnifications and NAs of the used apertures. The spacing between the grids and inner frames was chosen as 375 μm and the width of the frame lines and arrows was set to 5 μm. Including the arrows, the entire pattern measures roughly 12 mm x 12 mm.

5.2.2 Comparison of lithography to focused ion beam milled apertures

Before the fabrication of NHA samples as per the final design presented in chapter 5.2.1, it is useful to first evaluate the available preparation methods of electron beam lithography and FIB milling with regard to maximum patterning resolution, reproducibility, speed, and possible artifacts in the finished product. This was done on test samples with a simplified design and examined in the SEM in Bielefeld as well as the fluorescence setup available to Double Helix Optics LLC. Both samples used the same type of high precision microscope slide with a thickness of 170 ± 5 μm and a sputtered Au coating of 100 nm on a Ta seed layer of 3 nm.
Figure 5.6 shows a comparison of 200 nm sized holes created by a) FIB milling and b) e-beam lithography. The images were taken in the Helios NanoLab 600i dual beam FIB. It can be clearly seen that the milled hole on the left is almost perfectly circular, albeit slightly too wide. The surrounding material shows a second wider circle, indicating that the hole is actually cone-shaped due to the ion beam's intensity profile (c.f. chapter 2.2.2). Since this sample was milled with an acceleration voltage of 30 kV and a beam current of 28 pA, the size of this cone can be reduced by reducing the beam current which in turn increases the milling time. Beside the hole profile, the surrounding thin film was not damaged by the ion beam in any way. The hole that was prepared by electron beam lithography using the AR-N 7520.18 negative resist in Figure 5.6 b) also shows a low ellipticity and matches the desired measurement precisely. However, around the hole is a ridge of excess metal from the thin film deposition that could not be removed in the lift-off process. This artifact is expected for thin films of this thickness since part of the resist pillar's sides is also coated with stray metal atoms during the sputter deposition process. If the film is thick enough, part of it remains after the resist is dissolved and removed. For

the application in the NHA, however, this is not a problem since the holes will be imaged through the glass slide from below.
Both holes show no residual material inside the hole, so a fluorescent dye can be added for use in the fluorescence microscope. From only considering the aperture quality in the SEM, both techniques seem to provide good results. However, milling with the FIB is many times faster than the e-beam lithography process as precise exposure takes a lot of time and the additional steps of development and lift-off are not needed in the FIB. It is worth noting, that cutting finding structures of several millimeters size with the FIB would take hours if not days and is therefore not advisable. This means that even using the FIB for creating the apertures themselves, a lithography step to create the frames would be needed.

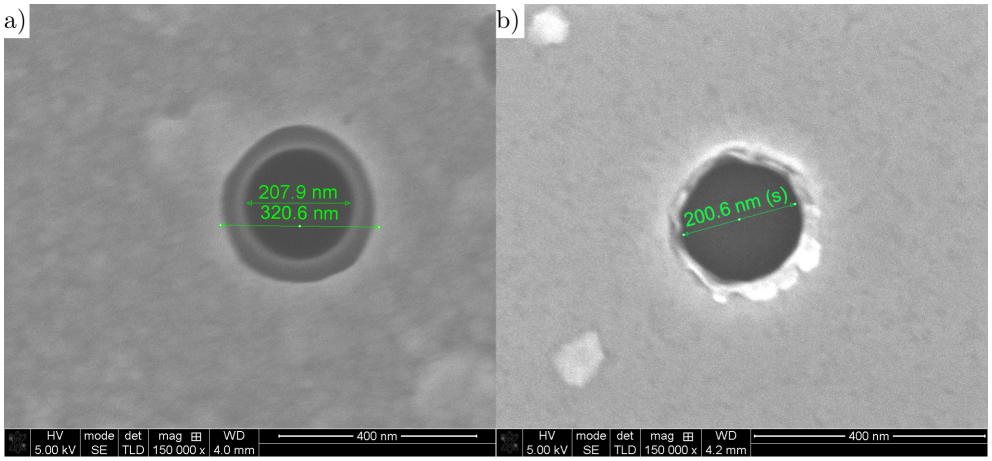

Figure 5.6: a) SEM image of a 200nm hole in a Au film on a Si substrate etched with a focused ion beam at 30kV acceleration voltage and 28pA beam current. b) SEM image of a 200nm hole in a Ru film on glass substrate created by using e-beam lithography and AR-N 7520 negative resist. Au films were not used after the initial test samples, since the Au film's granularity caused opacity issues in the fluorescence microscope.

A major disadvantage of using the FIB milled holes was found, once the samples were inspected in the wide field of view of the fluorescence microscope. First, the milled grids showed some irregularities in the hole spacing that could be attributed to random stage movement inaccuracies (c.f. chapter 4.2.5). Second, some holes randomly appeared brighter and larger than others, even though the SEM showed a narrow size distribution. A possible explanation for this is a lack of depth control combined with the optical properties of the used materials. The milling depth of the ion beam was set to 100 nm, which is roughly the same as the film thickness. However, the milling depth in the machine software is calibrated for silicone, which is a relatively hard material. Thus, the real depth of the holes is likely more than 100 nm. The variance in brightness can then be attributed to a variance in depth since there are a few random parameters that can have a minor influence on the milling process. Given the high localization precision of the fluorescence microscope using the double-helix PSF, even small variations in the milling beam current could lead to a detectable difference in depth. Additionally, milling along grain boundaries is faster than through a single crystal, thus random variations in the crystal structure

could also lead to minor differences in the perceived hole depth.
By penetrating into the glass slide, the ion beam creates a cavity inside the glass for the fluorophore. Since the fluorescent light is emitted in all directions, sources from within the glass also get reflected on the metal coating on top of the glass slide, which makes the aperture appear larger than it actually is. On top of that, the variation in depth can be detected through the rotation of the PSF, as the focal plane is at the interface between the glass slide and coating. This is visualized in a sketch in Figure 5.7. For applications where this level of precision is not important, milling apertures with a focused ion beam is a fast and easy way to manufacture apertures [5]. In this case, however, the disadvantages of the technique are too obvious to ignore. Hence, the full-size NHAs will be fabricated by an optimized lithography process to provide perfect depth control on top of a good lateral resolution.

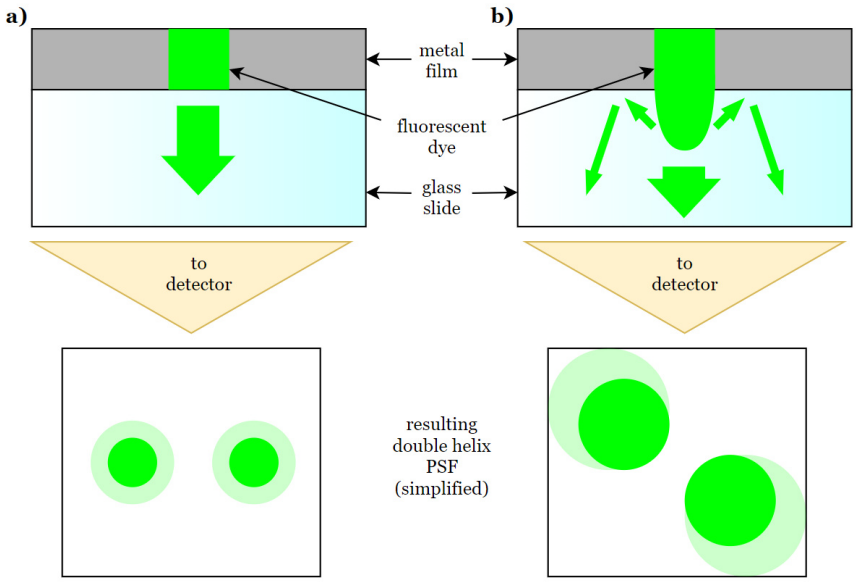

Figure 5.7: Impact of missing depth control on the fluorescence signal of the NHA grid. a) Holes created by lithography do not damage the glass substrate and therefore have perfect depth control leading to a clean fluorescence signal when in focus. b) Holes created by FIB lack precise depth control resulting in the signal appearing closer to the surface and wider due to additional light being reflected back from the metal film. This broadens and rotates the double helix PSF.

5.2.3 Materials and substrate preparation

In order to match the finished NHA to the focal length of commonly used objective lenses, 'high precision microscope slides No. 1.5H' made from 'borosilicate glass D 263® M' by Marienfeld Superior with a thickness of $170 \pm 5\,\mu$m and a refractive index of $n_D = 1.523$ are used as the base material for the apertures. As a first step each slide is individually cleaned in an ultrasonic bath of acetone and ethanol for five minutes each. To avoid scratches, the slides are suspended by a PTFE tweezer inside the beaker so that no flat surface touches the bottom of the glass. After each step excess fluid or dust is blown off with a nitrogen gun.
The clean samples can then be taken to the cleanroom for lithography prepara-

tion. With the given limitations to the size and shape of the holes, the only viable lithography option is using an electron beam for exposure, since the considerably faster UV-lithography is diffraction limited. Electron beam lithography on glass poses some unique experimental challenges, as glass is not conducting. Without any additional medium to make the glass slide more conductive, it would just accumulate static charge and disperse the electron beam so no exposure could occur. The used negative e-beam resist AR-N 7520.18 [71] is a weak conductor, but with an additional coating of the protective PMMA Electra 92 (AR-PC 5090) [53] the conductivity of the microscope slide improves enough so that e-beam lithography becomes possible. This protective coating contains small carbon particles that help to dissipate charges, which are also responsible for the characteristic black color. The lacquer is applied with a spin coater at 2000 rpm for 60 s which results in a thin 60 nm layer that does not negatively influence the possible resolution of the e-beam resist underneath. After baking the AR-N 7520.18 layer at 85 °C for 2 minutes, the AR-PC 5090 coating is applied directly on top and baked again at 50 °C for 2 minutes.
After exposure in the Zeiss LEO 1530, the conductive coating can be easily removed in deionized water for a few seconds until the brown tint on the glass is no longer visible. This does not damage the still undeveloped e-beam resist underneath. AR-N 7520.18 is developed in AR 300-47 developer by Allresist for 9 minutes and then cleaned for 30 s in deionized water. At this point, both the finding lines and the apertures are masked by pillars of hardened resist. The opaque metal coating is deposited by sputter deposition in a T11600 system by Leybold with 8 targets. Experiments with early prototypes have shown that Au coatings are easily scratched and can be accidentally removed with tape. Ta coatings, while a lot more mechanically resilient proved to be partly translucent even at a thickness of 100 nm. As a consequence the NHAs are coated with a layer of 80-100 nm Ru on top of a 3 nm Ta seed layer that increases the adhesion of the Ru film to the glass surface. Ru has good mechanical properties, does not corrode easily in ambient conditions and has an absorption coefficient of $\alpha = 6.0987 \cdot 10^5\,\mathrm{cm}^{-1}$ which means that as a rough estimate at 100 nm thickness only 0.22 % of light is transmitted [72]. After sputtering the resist mask is removed in an ultrasonic bath with N-methyl-pyrrolidine (NMP), a strong solvent, for one hour and subsequently cleaned in ethanol for another 5-10 minutes.
The quality of the finished NHA can be checked with a SEM. For use in a fluorescence microscope a few additional steps are necessary, which will be explained in chapter 5.2.6.

5.2.4 Optimization of the lithography process

On typical Si substrates, AR-N 7520.18 resist needs an area dose of $S = 400\,\mu\mathrm{As/cm^2}$ to be exposed properly. Depending on the desired pattern, for example when small isolated features in an otherwise homogeneously exposed area are desired, it can be necessary to adjust the area dose. This prevents over- or underexposing the details and can be used to fine-tune the size of individual features. Since scattered electrons from the substrate also contribute to the exposure of the resist, the real size of the exposed features is typically a few nanometers larger than the set pattern. For electron beam lithography on glass, a few additional considerations need to be made. First, above a certain beam current the protective coating of AR-PC 5090 becomes unable to dissipate the incident charge. The substrate would then deflect the beam and make exposure of the resist impossible. Thus, only small beam currents can be used, which increases the total exposure time. Second, glass has different scattering properties for electrons than typical Si substrates. It is expected, that far fewer electrons are scattered back to the resist, which increases the necessary dose of primary electrons and therefore the exposure time. Lastly, in spite of the protective coating increasing the conductivity of the glass enough to make electron beam lithography possible, a small amount of beam widening can be expected even for small currents due to a localized accumulation of static charge at the incidence point. Hence the maximum resolution on glass may be smaller than for lithography on semiconductor samples.

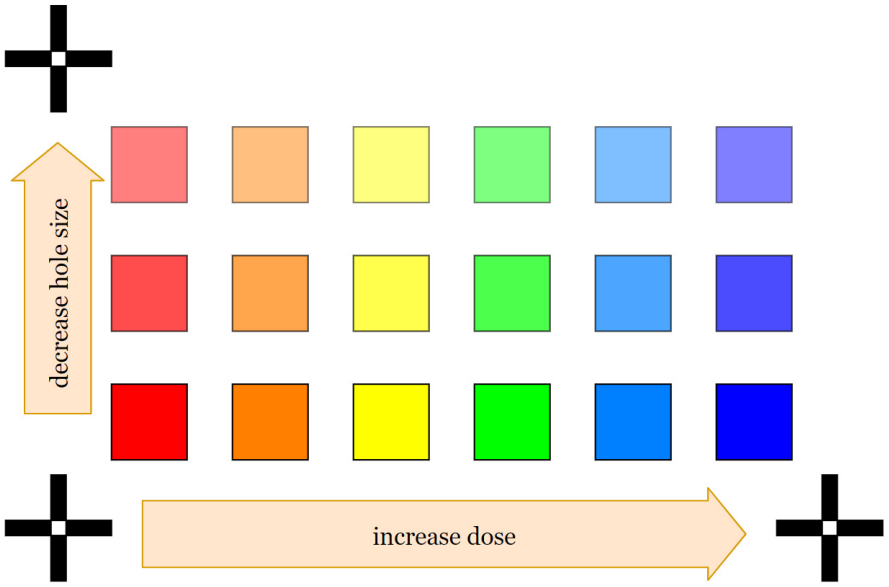

Figure 5.8: Schematic sketch of the dose test pattern used for the NHAs. Each square represents a 100 μm x 100 μm grid of apertures of a certain size and dose. Moving to the right the dose increases incrementally. Moving up decreases hole size (i.e. 300 nm, 200 nm, and 100 nm). Cross marks are used to find the area on the glass slide.

With these considerations in mind, several dose test samples were prepared to investigate the optimal exposure parameters for glass substrates. A sketch of the pattern used for these samples is shown in Figure 5.8. Each square in the sketch

represents a write field of 100 μm x 100 μm with apertures of a certain size and dose. The base area dose was set to the standard value of $S = 400\,\mu\mathrm{As/cm^2}$ and a scaling factor F was used to set the final dose of each square. Crosses on three of the four corners make the structure easily identifiable from a low magnification image. They additionally mark the orientation of the structure so that each square can be matched to its dose factor without fail. Moving to the right within a row increases the dose factor F incrementally by 0.2, whereas moving up a row will decrease the aperture size, i.e. 300 nm, 200 nm, and 100 nm. In the real structure, each row contains 14 squares and two rows are dedicated to 100 nm apertures instead of one since smaller structures are more difficult to expose and require more attention.

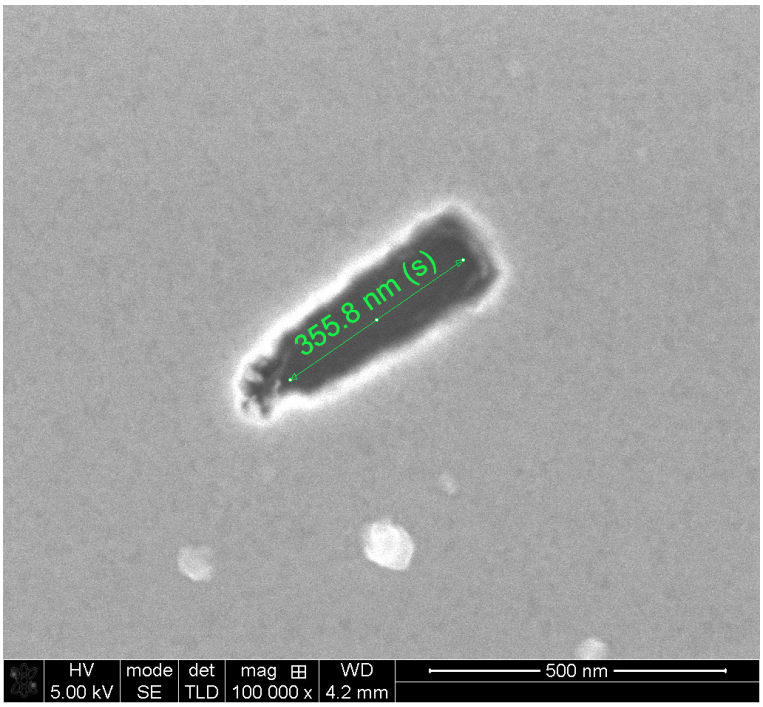

Figure 5.9: SEM image of a 100 nm resist pillar that was exposed with a dose factor of $F = 7.7$. The pillar fell over before the metal film was deposited, so that after the lift-off a rectangular hole remains.

A separate dose test for the finding structure using bars revealed that for large continuous structures a dose factor of $F = 2.2$ is necessary. In larger structures adjacent pixels contribute to the exposure, thus for isolated features the required dose is higher. Therefore, the 300 nm holes were tested with dose factors from 2.4 to 5.0, the 200 nm holes were tested from 3.0 to 5.6, and the 100 nm holes were tested from 4.5 to 9.9. For too high doses, the resist gets overexposed and can carbonize, which can reduce the solubility to the point where the resist can not be removed with NMP. For larger features with a diameter of 300 nm and 200 nm, the ideal dose factor was found to be 3.0 and 3.2, respectively. However, the 100 nm apertures proved difficult to realize. With a dose factor of 7.5, the apertures could be developed and lifted without artifacts, but the diameter of the holes was between 100 nm and 125 nm due to overexposure.
At smaller dose factors however, most of the 100 nm apertures (90 % or more) could either not be lifted at all or the pillars fell over before the Ru layer could be deposited

on top, which resulted in a rectangular defect of a few hundred nanometers in size. This form of defect is shown in Figure 5.9. Given the relative success for the slightly too large apertures with a higher dose, the problems with the lift-off most likely result from underexposure and therefore a too thin layer of resist that is completely covered by the sputtered metal thin film. A proper lift-off is only possible when the edges of the resist are undercut so that no continuous layer can form on top. The toppled pillars result from a problem that is a bit more difficult to deal with. Using the standard conditions for the AR-N 7520.18 resist, i.e. application through spin coating at 5000 rpm for 30 s, the resist layer is between 350 nm and 400 nm thick. With narrow features like the 100 nm apertures, the resist pillars have an aspect ratio of about 1:4, which can be imagined similar to balancing a pen on its end. Thus, the mechanical stability of the resist pillars in the developer solution suffers and the features can not be realized properly.
To solve this problem, the resist layer needs to become thinner. This can be done by either spinning it faster or longer, or by adding a thinning agent to the resist so that it becomes less viscous. If the resist is too thin, however, the sputtered metal layer will be continuous and the lift-off is impossible. Hence, the thickest possible resist layer that produces reliable 100 nm apertures is desired. A series of dose tests for the spinning speed and thinning ratio revealed the best conditions for the resist application to be a 3:2 ratio of Allresist AR-N 7520.18 negative e-beam resist to Allresist 300-12 thinner for e-beam resists [73] spun at 5000 rpm for 60 s. These conditions ensured a clean lift-off for all aperture sizes and prevented the resist pillars from falling due to an unfavorable aspect ratio. Through another series of dose tests, the aperture sizes were fine tuned, as the aforementioned electron scattering typically leads to structures wider than their set value. The final dose scaling factors and pattern sizes is found in Table 5.1.

desired aperture size [nm]	set pattern size [nm]	dose factor
lines	5000	2.2
100	92	8.1
200	190	3.8
300	290	3.2

Table 5.1: Summary of ideal exposure conditions and pattern sizes for nanohole apertures.

5.2.5 Process runtime improvements

For the fabrication of the nanohole apertures (NHAs) the largest bottleneck is the exposure time in the e-beam lithography process. The effective dwell time of the beam for each pixel can be calculated as $t_{\text{eff}} = F \cdot S \cdot x^2/I$ with the dose factor F, the standard area dose S, the step size x, and the beam current I which is measured with the Faraday cup inside the Zeiss LEO 1530 before each exposure. The resulting beam velocity is given by $v_{\text{B}} = x/t_{\text{eff}}$ and is typically in the order of a millimeter per second. Using the standard 30 μm aperture of the Zeiss LEO 1530, which produces a beam current of roughly 0.02 nA the exposure of the NHA apertures takes two hours. With the same conditions, the exposure of the finding structures, however, takes more than 24 hours, because of the large surface area that needs to be exposed. For typical exposures of large structures like the finding lines around the NHA the

largest aperture in the Zeiss LEO 1530 with a diameter of 120 μm is used. As even with the conductive coating or AR-PC 5090 the conductivity of the glass slide is low in the order of $\sigma = 1\,\mathrm{S/m}$, the largest aperture that can be used has a diameter of 60 μm and provides a current of roughly 0.4 nA. During the exposure process, the aperture can be automatically changed with a script, so that the sensitive apertures are exposed with a low current for maximum resolution, whereas the broad finding structures are exposed at a higher current to reduce the total exposure time. When using an automatic aperture change in the LEO 1530, it is important to do the finer exposure (i.e. the apertures) first, as there is always a slight focus and astigmatism error when the apertures are changed. Additionally, the apertures in the machine are on a dial wheel, so there is an offset of several microns from the 30 μm aperture to the 60 μm aperture. This has to be corrected manually before each exposure by creating two separate alignment calibrations that are saved to their respective aperture. Within these alignments, the coordinate system of the interferometer stage and the electron beam including the offset are matched precisely. Using the automatic aperture change the total exposure time is reduced to 8.5 hours.

5.2.6 Dye application and final assembly

To use the finished NHAs for multicolor alignment in fluorescence microscopy, the fluorophores need to be applied into the apertures. Ideally, the fluorescent dye is concentrated in the pores and as little dye as possible remains on the metal coating to avoid background signals. Even though the Ru film of 100 nm only transmits 0.22 % of light (c.f. chapter 5.2.3), this is important to increase the signal to noise ratio. For early test samples the Reference Dye Sampler Kit R-14782 from Thermo Fisher Scientific was used [74]. It contains the five individual fluorophores quinine sulfate, fluorescein, carboxy-tetramethylrhodamine, sulforhodamine 101, and nile blue. After mixing the dyes in a 1:1:1:1:1 ratio, different application methods were tried. While just placing a droplet of the dye mix on the apertures and leaving it to dry does yield usable results, the background is quite high and the dye distribution uneven. Spin coating the dye mix requires a wetting agent like polysorbate 20, as the dye's surface tension is high. Even with a wetting agent, the dye distribution remains relatively uneven. Hence, Double Helix Optics LLC is developing a method to apply fluorescent quantum dots instead, as they are easier to spin coat with an appropriate wetting agent.
Since the NHAs are quite fragile with a thickness of 170 μm, the apertures are fixated to standardized 73 mm × 26 mm microscope slides with a thickness of 2 mm by Marienfeld Superior after the dye is applied. These microscope slides fit into most commercially available microscopes, but as only the thickness of the coated NHA slide is important for the measurement, a different carrier slide format could be used. Once the aperture slide is glued to the carrier slide using transparent UV glue, it can not be removed. Because the specific dye used in these experiments is comparatively resistant to bleaching, Double Helix LLC estimates the NHAs to last a few years if they are stored in a dark place. The actual lifetime of the device will also heavily depend on the frequency of use.

5.3 Results

The finished NHAs were characterized using the Helios Nanolab 600i in Bielefeld and the STORM setup at BioFrontiers Institute of the University of Colorado in Boulder, Colorado, in cooperation with Double Helix Optics LLC. A Nikon Eclipse Ti2-E motorized inverted microscope [75]serves as the base of the super resolution microscopy setup at the laboratory in Boulder. With the Nikon N-STORM system, the setup supports 2D and 3D imaging in multiple colors and is equipped with a vibration isolated stage that can be precisely adjusted by piezo actuators [76]. The system is augmented by a Double Helix 'Spindle^2', a high precision splitter/combiner for 3D multi-color imaging and the option of adding different phase masks to the two available channels. In addition to the Spindle^2's four operation modes, the system comes with 3DTRAX, a FIJI plugin for high precision emitter localization, particle tracking, image reconstruction, extended depth of field imaging, and comprehensive plotting options [77]. The localization precision given by the manufacturer is 20 nm in the lateral and 55 nm in the axial dimension.

5.3.1 Structuring results

Before the dye is applied, each NHA is checked in the SEM to ensure the correct measurements of the apertures and to find possible defects. Since the apertures can only be seen in the SEM at good focus and stigmation settings while at a magnification of 2500x or higher, the field of view for these quality checks is quite narrow. To measure the exact dimension of single apertures, the magnification needs to be in the order of 10^5x. Thus, only random sample surveys can be performed in a reasonable time on each aperture slide.

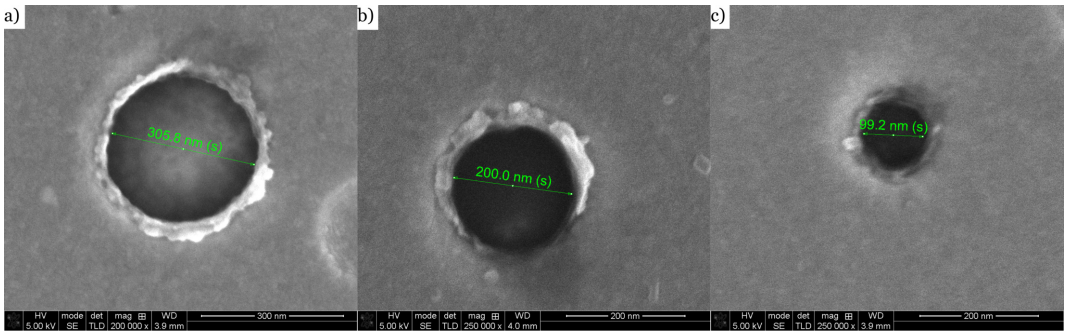

Figure 5.10: SEM image of finished apertures in an 80 nm thick Ru film on a glass slide: a) 300 nm size for section A. b) 200 nm size for section D. c) 100 nm size for sections B and C. Images were taken with an acceleration voltage of 5 kV, a beam current of 0.17 nA and a magnification of 200,000x (a) and 250,000x (b, c). The measured sizes are 305.8 nm, 200.0 nm, and 99.2 nm, respectively.

For the same reason, it can be hard to spot defects in the metal coating unless they are close to an aperture. Any defects in the Ru film can cause problems during fluorescence microscopy experiments, since especially large defects act as strong emitters that can overexpose adjacent areas of the image. For small defects contrast and brightness settings can be adjusted to save the overexposed areas, but if the defect is too large, the field of view has to be moved so that the defect is not in the

image. This obviously reduces the usable area of the NHA dramatically, so ideally the aperture coatings should be as close to defect-free as possible.
Figure 5.10 shows examples of finished apertures and their measurements for a) 300 nm apertures in section A, b) 200 nm apertures in section D and c) 100 nm apertures in sections B and C. The desired tolerances for the measurement are 5 nm per 100 nm aperture size, i.e. 300 ± 15 nm for apertures in section A, 200 ± 10 nm for apertures in section D and 100 ± 5 nm for apertures in sections B and C with ellipticities of 0.95 or better. Ellipticity in the apertures occurs during the exposure process when the beam focus or astigmatism is not properly calibrated. Otherwise the deviation of the aperture width in the x- or y-direction is less than 5 nm for all aperture sizes.
From a statistical point of view, it is useful to look at the deviation from the desired hole size as well as the standard deviation of the measured hole size beside the average hole size. For a randomly selected sample NHA, the results of the statistical analysis can be found in Table 5.2. It is worth noting, that the standard deviation in all cases is well below the given tolerance, however, especially for the smallest apertures, individual holes can be slightly outside the desired specifications. Since the image resolution and the precision of marking the hole diameter in the Helios Nanolab 600i is a limiting factor to the accuracy of the measurement, the apertures in this case are within an acceptable margin. Furthermore, since the standard deviation is well below 4 nm in all cases, all apertures in any given section are roughly the same size and have only a small deviation from the mean size. Thus, their function as point-like diffraction limited emitters is assured. The mean aperture size can vary from slide to slide due to small random variations in resist thickness or current during the e-beam lithography process. For the 100 nm apertures, the average size could be as low as 97 nm or as high as 103 nm. However, within a section, the deviation from this average was always well below 5 nm. Qualitatively, the same is true for the larger 200 nm and 300 nm apertures, but since their size tolerance is higher, the variations are negligible.

section	des. size [nm]	Ø size [nm]	std. deviation [nm]	max. deviation [nm]
A	300	298.29	3.83	5.0
D	200	198.70	1.93	8.1
B/C	100	102.21	2.84	6.4

Table 5.2: Summary of the statistical analysis for size measurement on randomly selected NHAs. The max. deviation [nm] marks the largest individual difference of a single aperture with regard to the desired size.

Figure 5.11 shows a) a sample image of the finished finding structure and b) a sample measurement for the spacing of the apertures in section C. The dark contrast of the finding structure implies that this area does not produce any secondary electrons for the detector to see and is therefore empty. Thus, the lines will be transparent for the fluorescence microscope and facilitate easy navigation around the sample. For the hole spacing, the tolerances are the same as for the respective holes in each section. Since the measurement is limited by the detector resolution and the ability to correctly mark the distance pixel by pixel, the accuracy of the measurement is not sufficient to reliably calculate a standard deviation. However, the hole spacings are accurate within the measurement error.

Similar to the FEBID particles in chapter 4.2.5, the accuracy of the spacing is limited by the precision of the stitching in the Zeiss LEO 1530 during the lithography process. Since an interferometer stage is used, the stage position is far more precise than a step motor could achieve. The manufacturer Raith Nanofabrication lists a maximum resolution of the interferometer as 0.15 nm [78], however, even generously estimating a ten times lower actual resolution in the used system, the fabricated aperture spacing is well within the tolerance limit.

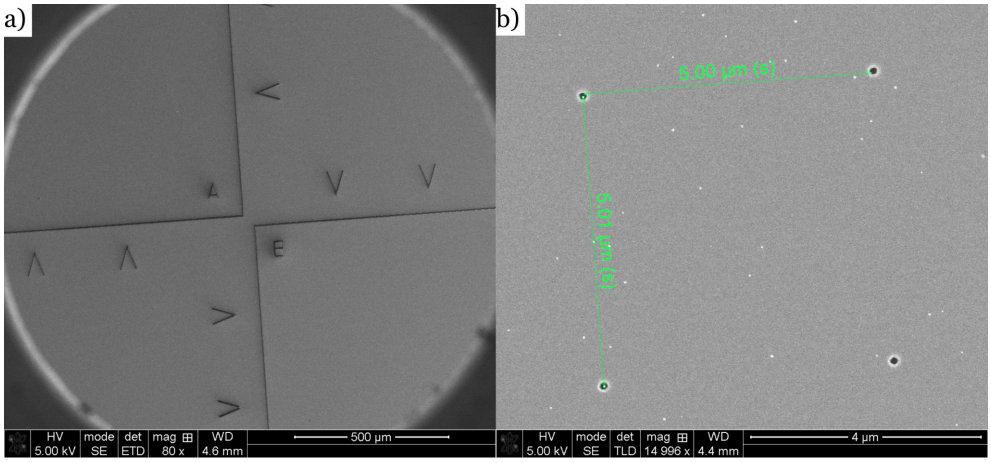

Figure 5.11: SEM image of a) frames surrounding the NHA grids to make them easy to find and identify and b) measured hole spacing in section C. Measurement accuracy (center to center) is limited by image resolution, but is assumed to be below 10 nm.

As discussed in the introductory paragraph to this section, defects in the aperture slide surface can lead to problems during imaging. Figure 5.12 summarizes four kinds of defects that can occur in the fabrication process. These errors can be divided into process-related and random errors. In Figure 5.12 a) a hole left by a toppled resist pillar in one of the 100 nm aperture sections is shown, whereas b) shows an image from section C (100 nm apertures, 5 μm spacing) with an incomplete lift-off due to overexposure. An incomplete lift-off can also occur as a result of a too thick metal film (c.f. chapter 5.2.4). The washed-out edge of the 100 nm aperture that can be seen in Figure 5.12 c) can occur as a result of an underdeveloped resist pillar, when residual unexposed resist remains beside a developed resist pillar. These kinds of defect are all process-related and can be avoided by proper design of the lithography process as shown in chapter 5.2.4. Using the optimized fabrication method, these defects occur only in extremely rare cases.
Random holes in the metal film like in Figure 5.12 d) are harder to eliminate. They can originate from stray dust particles or other nano-sized impurities that can reach the substrate surface in the laboratory before the metal film is deposited. During the lift-off process in the ultrasonic bath, these particles can also be removed and leave a hole in the coating. The impact of these can be limited by working in a cleanroom environment with high air purity for most of the production process so that no dust can settle on the substrate. However, since the SEM and the sputtering machine for the metal film deposition are located in laboratories with lower air purity, this kind of defect can not be completely eliminated. To reduce the defect

density, the sample boxes were vacuum sealed for all transports between laboratories. Reducing the defect density even further would require the full production path to move to a cleanroom environment. Nonetheless the defect density in the optimized samples should be low enough, that the functionality of the nanohole apertures is not impaired.

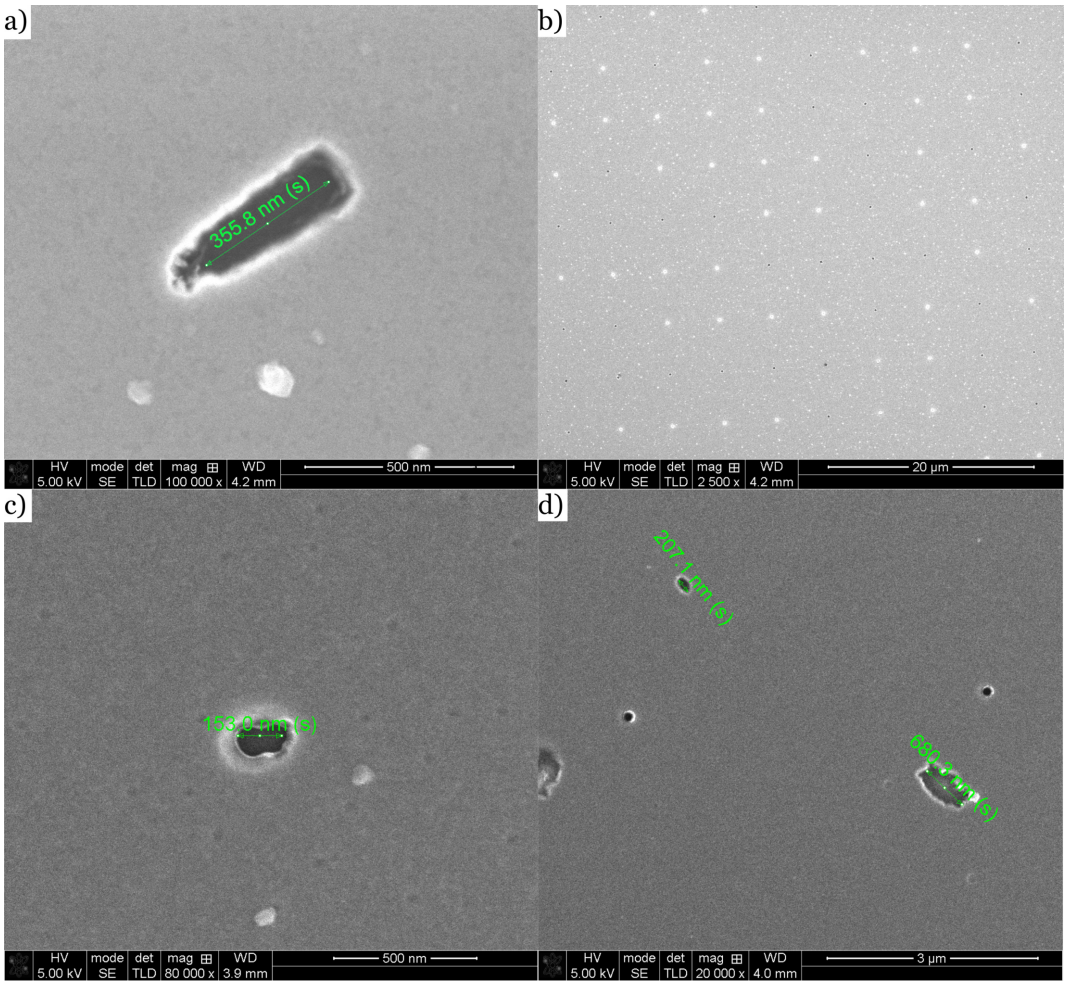

Figure 5.12: SEM images of common artifacts and defects: a) A resist pillar that toppled over during the development process. This has been resolved in more recent samples with properly thinned resist. b) Incomplete lift-off in Section C. This is a common problem for too high doses or too thick metal films, as the resist becomes harder to dissolve. c) A 100 nm hole that was most likely underdeveloped so that residual resist remained beside the 100 nm resist pillar. d) Larger defects next to 100 nm grid holes. These likely originate from dust particles on the surface prior to Ru deposition, that are removed along with the metal layer in the ultrasonic bath.

5.3.2 Optical measurements and calibration

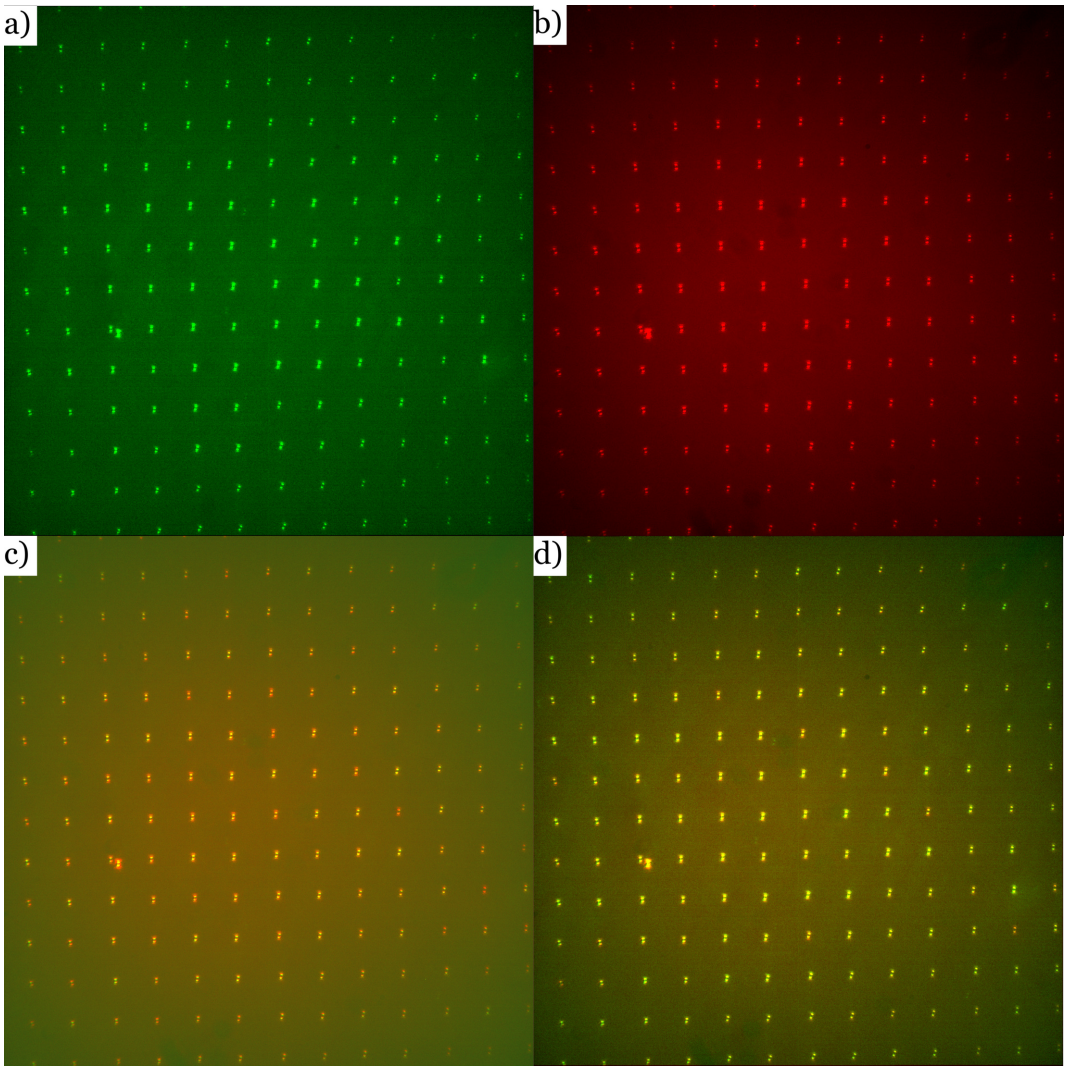

Figure 5.13: Wide field image at 100x magnification with a 1.49 NA objective from the Nikon Eclipse Ti2-E STORM setup: a) flattened and de-warped 580 nm fluorescence channel to match the reference channel in b). b) flattened 670 nm fluorescence channel. c) overlay of the uncorrected 580 nm channel (green) and the 670 nm channel (red) d) overlay of the corrected 580 nm channel (green) and the 670 nm channel (red). All corrected images were also adjusted for contrast and brightness for better visibility. The left side of the chosen field of view contains a defect, which produces the additional PSF used as a marker. Alignments were performed using an early version of DoubleHelix' 3DTRAX plugin for FIJI. The final release version may differ. Images provided courtesy of DoubleHelix LLC.

Optical measurements and calibration tests on the finished nanohole apertures were performed at the BioFrontiers Institute at the University of Colorado in Boulder, Colorado in collaboration with DoubleHelixOptics LLC. The experimental setup consists of a modified Nikon Eclipse Ti2-E inverted microscope that uses the Nikon

n-STORM technology and supports imaging in 2D and 3D. The excitation sources for fluorescence at 580 nm and 670 nm were coupled to the system using the DoubleHelix Spindle^2, which is a high precision splitter/combiner. Wavelength specific DoubleHelix phase masks (DH1-580-2045 and DH1-670-2045 respectively), that produces a double-helix point spread function were placed inside the Spindle^2. This provides additional depth of field and an easier way of localizing single emitters on the z-axis as the over- and underfocused double-helix PSF rotate in different directions.
Figure 5.13 illustrates the results of the alignment process at a magnification of 100x with a 1.49 NA objective using the NHA as a calibration sample in combination with the DoubleHelix 3DTRAX plugin for FIJI. The version of this program used to generate these images is still in development, so the release version may be different. Each pixel in the image has a size of 65 nm. All corrected images in this figure are adjusted for contrast and brightness for better visibility. The defect on the left side of the field of view, which creates an additional PSF, was used as a marker. Figure 5.13 a) shows the corrected 580 nm fluorescence channel of the setup. This means that the image was flattened to remove the 'field of view warp' caused by the microscope optics. An additional de-warping step was added to match this channel to the reference channel, which in this case is the red 670 nm one in Fig. 5.13 b). Fig. 5.13 b) shows an image of the 670 nm channel after flattening to adjust for the 'field of view warp'. As the orientation of the PSF also depends on the alignment of the phase masks, the resulting corrected PSFs can have a slightly different alignment than the other channel. This is not an issue during the fitting procedure that localizes the emitter.
The images in Fig 5.13 c) and d) each show an overlay of the 580 nm and the 670 nm channel for the uncorrected raw data and the fully corrected overlay, respectively. At this magnification the difference between Fig. 5.13 c) and d) is extremely subtle and mostly visible in the difference of the dominant color in the images. Whereas the uncorrected image appears in a dark shade of orange and the green channel is barely visible for some PSFs, the corrected image is mostly colored in a uniform yellow that is caused by the increased overlap of the two channels. Since the base microscope is already quite precise, and the aim is to align the image space at a super resolution level, the adjustment happens in the order of single pixels at this magnification, which is why it is impossible to detect the warp in the image with the naked eye. It should be noted, however, that it is not expected that the PSFs of both channels overlap entirely in the image space in this example, as the double helix PSF's size is affected by the wavelength. The accuracy of the alignment is also limited by the uncertainty of the localization, i.e. the fitting of the PSF. There remains a slight tilt in the corrected images, that is assumed to be the result of a real tilt of the sample versus the optical axis of the objective lens. As this is an error specific to the placement of the sample in this measurement, said tilt was intentionally not removed.

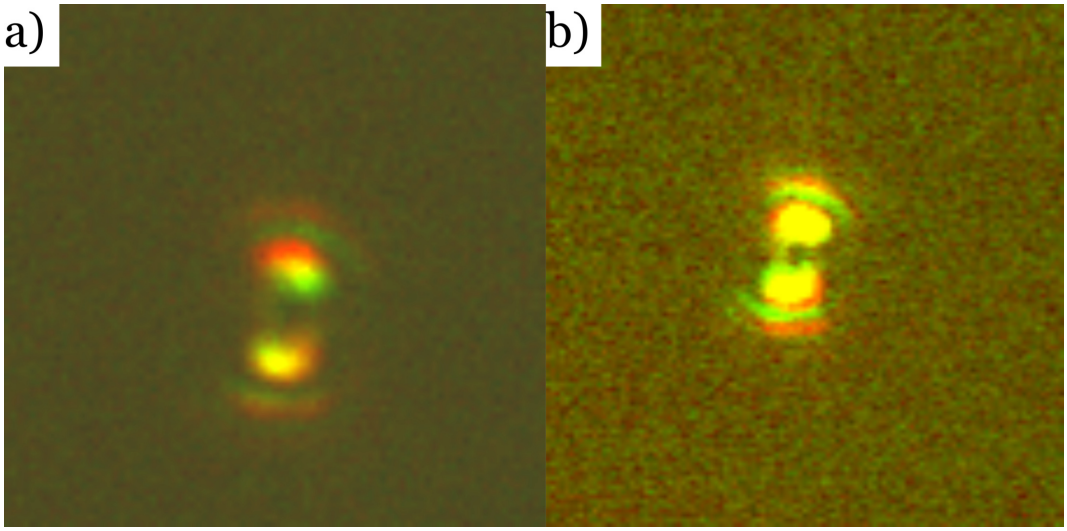

Figure 5.14: Zoom-in on an individual PSF in the overlay of the 580 nm channel (green) and the 670 nm channel (red) of the Nikon n-STORM setup for a) the uncorrected image and b) the image after calibration using the NHA and 3DTRAX. Images provided courtesy of DoubleHelix LLC.

A zoom-in on individual PSFs from these overlays is shown in Figure 5.14 for the uncorrected case (a) and the correctly calibrated image using the NHA and the 3DTRAX software (b). In the uncorrected image, the combined PSF has clear red and green fringes at opposing sides of the main lobes, which indicates a misalignment. The corrected image in Fig. 5.14 b) shows an almost perfect overlap of the two PSFs in the main lobes, indicating a successful calibration. Red and green fringes are as expected still visible in the halo shaped secondary lobes of the double-helix PSFs in the corrected images, because the size of the PSF is affected by the wavelength. Since this image is heavily zoomed-in, and the 3DTRAX software that calibrates the experimental setup with the data from the NHA is still in development, a final precision in the order of single pixels even at higher magnifications is estimated.

5.4 Summary and Outlook

The quality of optical components has always been a limiting factor in microscopy. Macroscopic materials like mirrors and lenses have improved considerably over the years through the use of highly optimized machines, be it for cutting and polishing lenses or the deposition of coatings for specialized mirrors. The possibilities offered by augmentation of macroscopic materials with nanotextured components are not yet fully explored, as it is a comparatively young field of research. With prototyping being time-intensive and requiring specialized machines, the production of nanotextured tools and materials is still challenging and expensive. For industrial applications, these processes are mostly only economically viable, when components are produced in large quantities, which limits the options for custom-built optical components.
As part of this work, it was demonstrated that both focused ion beam and lithography techniques can be used to manufacture small-scale prototype series of high precision optical devices. For the purpose of multicolor alignment and 2D warp correction in 3D-capable STORM microscopy, the lithography approach proved to be superior because of the more precise depth control. For the use in different 2D super-resolution microscopy techniques like structured illumination microscopy (SIM), similar devices prepared by the faster focused ion beam method could be viable. The nanohole aperture (NHA) device was designed in collaboration with DoubleHelixOptics LLC. Through careful optimization and automation of the lithography process, it was possible to create a fabrication work flow that yields repeatable highly accurate optical devices with manufacturing tolerances of only a few nanometers. While this work focuses on the production of apertures, the presented techniques are easily transferable to other applications.
Each optimized NHA consists of more than 71000 individual holes spread out in different sizes and spacings in four sections within a labeled frame for easy navigation in the microscope. The devices were tested in a modified Nikon n-STORM setup at BioFrontiers Institute in Boulder, Colorado, where lasers of various wavelengths are used to create super resolution images of complex biological samples with a combination of multiple color channels. Due to aberrations, these images contain a slight warp as well as an offset between different color channels, so that a calibration is needed to correct the mismatch. It has been shown that the nanohole apertures, which are filled with multi-colored fluorescent material, are highly effective to calculate a correction matrix for the different color channels based on the known size and position of the holes on the device.
This approach offers several benefits compared to similar state-of-the-art calibration methods that involve fluorescent beads. To complete the color correction calibration with beads, a section with only individual beads without agglomerates has to be found, which can be time-consuming. Additionally, only the size of the bead is known and relative distances between the color channels are used for the calibration. In comparison, the nanohole apertures offer an easy work flow, as the nanotextured features are periodically distributed. Furthermore, the spacing between individual emitters on the NHA is well known, so that the intrinsic warp of any color channel image can be corrected. Since beads are distributed randomly on a cover slide, this is not possible without a nanotextured grid. As a result, this subtle yet powerful improvement can enable high precision co-location experiments in biological systems, where for example the proximity of differently marked proteins is of interest. The apertures are made of non-oxidizing materials and therefore can be safely

stored for long times as long as the fluorophores are not bleached. In conclusion, the nanopatterned apertures produced in this work offer a high precision calibration for multi-color super resolution microscopy as well as a new method to correct warped images, as the devices create a reliable ground truth.
To further develop this technique, it would be interesting to create a similar grid of diffraction limited emitters that provides precise information on the location of the emitters in all three dimensions. Engineered point spread functions offer a high level of accurate emitter detection in the axial direction. However, the influence of aberrations or warp in that direction is largely unknown and impossible to accurately calibrate up to this point. Improving upon the current design of the NHA, the aperture grid could include either a slope or a stair-step structure of a defined height so that the z-position of each emitter is clearly defined. From a process engineering point of view, the manufacturing of such a sample with the same precision as the NHAs presented in this work is extremely challenging but potentially useful for a future project.
A patent for the device developed in this work was filed in the USA and will be filed for the EU market in the near future.

6 Nanopatterned GMR devices for differential phase contrast magnetic imaging in the TEM

Nanostructured materials have gathered a lot of attention as so-called "meta materials" with impressive mechanical or optical properties like extreme mechanical stability against projectiles or a negative index of refraction [79, 80]. On the other hand, nanopatterned magnetic materials have been an essential part of research regarding data storage solutions and high-density magnetic recording is still a highly researched topic even in the age of solid-state drives (SSD) in consumer electronics [31]. Due to their longevity and comparatively low cost, magnetic recording media are still an important component for enterprise IT and long-term data storage solutions. Granular recording media consisting of a nanotextured FePt-C alloy are used for state-of-the-art hard disk drives (HDD) [81] and considerable effort is put into the improvement of the read and write density on nanotextured magnetic media. One approach is to have each bit represented by a single high anisotropy magnetic grain or particle in so-called bit patterned media (BPM), which can be rewritten by applying localized heat to the particle to reduce its H_C. Hence, this approach is commonly referred to as heated dot magnetic recording HDMR [82].
Beside their interesting properties for magnetic recording, nanopatterned magnetic materials can also exhibit unique magnetic ordering and domain wall structures like vortices that are of tremendous interest for magnetic microscopy methods [83, 84]. Schumacher *et. al.* investigated the propagation of domain walls in the presence of indentations (i.e. defects) that were fabricated with an atomic force microscope (AFM) by polar magneto-optical Kerr effect (PMOKE) measurements, showing that these nanopatterns can be pinning and nucleation centers for domain walls [85]. Other works investigated the effects of nano-sized defects and patterns on the magnetic switching behavior of thin films and small magnetic objects like rings, ellipsoids and bow ties which were prepared by lithography [86, 87, 88]. It was shown that not only the presence, but also the placement of the defect has significant impact on the vortex rotation in permalloy nanodisks [86].
The idea of regular nanopatterns of magnetic materials has been explored for example in the investigations on artificial spin ice structures [89, 90]. In an artificial spin ice, free-standing nanopatterned particles that typically have some form of shape anisotropy are aligned in a regular pattern. For various grid types like the famous Kagome lattice, the easy axis of adjacent particles can not always be aligned which can create so-called frustrated states [90]. The magnetic switching of these lattice structures is particularly interesting for microscopy techniques that are sensitive to the chemical and magnetic structure of a sample like synchrotron-based photoemission electron microscopy (XPEEM) [91].
Transmission electron microscope methods offer great options to image the magnetostatic ordering in a nanopatterned sample through Lorentz-TEM or differential phase contrast (DPC) microscopy at a high resolution [92, 93]. However, the experimental setup used in this work is not suitable to image processes that happen on a short time scale like the dynamics of magnetic switching. Recent studies on magnetic thin film systems in the TEM have proven the utility of DPC imaging to investigate the correlation of structural and magnetic properties at high magnifications [94].
Given that the investigation of nanopatterned magnetic materials in the context of large scale magnetic ordering is still a relatively young field of research, this work

will explore nanopatterned magnetic materials with various symmetry properties and characterize both the magnetic ordering and the electrical transport effects in this kind of sample. For the purpose of magnetic imaging using differential phase contrast in the TEM as well as Lorentz-TEM, the nanopatterned samples will be prepared by dual beam FIB methods on a 10 nm SiN membrane, so that the sample appears transparent for the TEM.
First, reference samples of $Co_{70}Fe_{30}$ thin films were prepared on a 5 nm Py seed layer to investigate the effects of the nanopatterning on a simple magnetic layer. As a second stage, Co-Cu-multilayer GMR thin film stacks are prepared in the same manner to investigate the effect in more complex samples [34, 95]. Additionally, as the magnetic imaging modes in the TEM can not resolve the magnetic structure along the specimen's z-axis, a reference is needed to spot any magnetic structures that are caused by the interlayer coupling in the GMR stack. The same patterns are then fabricated by e-beam lithography on Silicone substrates to characterize the electric transport properties. Since nanopatterning has been shown in the examples above to influence the magnetic switching behavior and domain wall movement, the observed magnetic structures in the TEM can be linked to the response of the GMR signal in multilayer thin film systems.
The theory of magnetic Lorentz fields (c.f. chapter 6.1.1) has been known for decades [96]. However, and maybe precisely for that reason, since magnetoresistive effects were yet to be discovered at that time, a characterization of the influence of such fields on GMR sensors especially in the context of direct magnetic imaging has not been researched before to the best of the author's and contributor's knowledge.

6.1 Theoretical background

6.1.1 Lorentz fields in magnetism

To understand the unique physical properties of nanopatterned magnetic thin films, it is important to understand what the introduction of voids does to a magnetic material. The polarization of dielectric materials in an external electric field can serve as a first, more commonly known, model system. In a dielectric medium the induced dipole moment $\vec{p}$ is proportional to the local electric field $\vec{E}$ and the polarizability α[97]. In a simple plate capacitor the polarized charge in the dielectric medium will create a local electric field $\vec{E}_{\mathrm{d}} \propto -\vec{P}/\epsilon_0$ with the polarization $\vec{P}$ and the dielectric constant ϵ_0 that opposes the electric field $\vec{E}_0$ created by the capacitor plates, the so-called depolarization field. This field is created by the surface charge of the polarized material. When a void is present in the dielectric medium, a similar surface charge of opposite polarity is introduced at its surface, which creates the so-called Lorentz field $\vec{E}_{\mathrm{L}}$that is of the same origin as the depolarization field $\vec{E}_{\mathrm{d}}$ but oriented in the same direction as $\vec{E}_0$[97]. This example is illustrated in Figure 6.1.

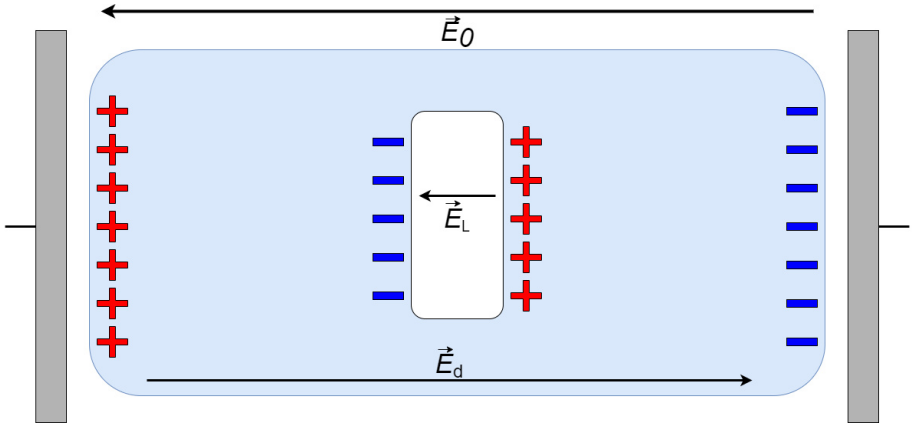

Figure 6.1: Schematic sketch of a plate capacitor with a dielectric medium that contains a void. The depolarization field of the medium opposes the external field $\vec{E}_0$, but the Lorentz field $\vec{E}_{\mathrm{L}}$ is oriented parallel to it.

Since there are no magnetic charge carriers, the same logic can not directly be applied to voids or defects in magnetic materials. However, the concept of an effective magnetic surface charge can be beneficial to develop an intuitive understanding of the mechanisms that govern the magnetic order in ferromagnetic materials with complex shapes. To establish the basic idea, there will be a brief digression into magnetostatics mainly following the considerations made in [98].

$$\nabla \cdot \mathbf{B} = 0 \tag{6.1}$$

$$\nabla \times \mathbf{H} = \mathbf{J} \tag{6.2}$$

Eq. 6.1 and Eq. 6.2 are the macroscopic Maxwell equations for the magnetic flux $\mathbf{B}$ and Ampere's circuit law for the magnetic field $\mathbf{H}$ in with magnetized materials in the presence of free currents $\mathbf{J}$. For practical reasons, the displacement field $\mathbf{D} = \epsilon_0\mathbf{E} + \mathbf{P}$ with the electric field $\mathbf{E}$ and the polarization $\mathbf{P}$ is omitted. In a

magnetic material the free currents $\mathbf{J}$ also obey the conservation law $\nabla \cdot \mathbf{J} = 0$. In a classical image microscopic currents inside the atoms are responsible for the magnetization $\mathbf{M}$ which describes the magnetic dipole moment per unit volume. The relationship between $\mathbf{H}$, $\mathbf{B}$, and $\mathbf{M}$ can be written as

$$\mathbf{H} = \frac{1}{\mu_0}\mathbf{B} - \mathbf{M}. \tag{6.3}$$

From a quantum mechanical point of view, the spontaneous magnetization arises from the exchange energy $\mathcal{J}$ that is related to the fermionic character of electrons and the postulation of total antisymmetry for the electronic wavefunction, an in-depth derivation of which can be found in [99]. Looking at the integral form of Eq. 6.1 for a small Gaussian pillbox at the surface of a homogeneously magnetized material, it follows that $B_2^{\perp} - B_1^{\perp} = 0$. Thus, the perpendicular component of the magnetic flux is continuous at the interface. However, the perpendicular component of $\mathbf{H}$ is not when the two adjacent media have a different magnetization since $H_2^{\perp} - H_1^{\perp} = -(M_2^{\perp} - M_1^{\perp})$. It also follows directly from Eq. 6.1 that a vector potential $\mathbf{A}$ for the magnetic flux of the shape $\mathbf{B} = \nabla \times \mathbf{A}$ can be defined as the divergence of a curl is always zero.
Similarly, without free currents when $\mathbf{J} = 0$, Eq. 6.2 becomes $\nabla \times \mathbf{H} = 0$ so that a scalar potential for the magnetic field can be defined as

$$\mathbf{H} = -\nabla \Phi_{\mathrm{M}} \tag{6.4}$$

similar to the electrostatic potential where $\mathbf{E} = -\nabla\Phi$. In a uniform and linear medium where $\mathbf{B} = \mu\mathbf{H}$ with the magnetic permeability μ it is possible to apply Eq. 6.1 and obtain the Laplace equation for the magnetic scalar potential

$$\nabla^2 \Phi_{\mathrm{M}} = 0. \tag{6.5}$$

Assuming a hard (or saturated) ferromagnet where $\mathbf{M}$ is mostly independent of the magnetic field, the equations 6.1 and 6.3 can be combined so that

$$\nabla \mathbf{B} = \mu_0 \nabla(\mathbf{H} + \mathbf{M}) = 0 \tag{6.6}$$

and thus

$$\nabla \mathbf{H} = -\nabla \mathbf{M} \tag{6.7}$$

Again using the magnetic scalar potential from Eq. 6.5 we can formulate the magnetostatic Poisson equation

$$\nabla^2 \Phi_{\mathrm{M}} = -\nabla \mathbf{M} = -\rho_{\mathrm{M}} \tag{6.8}$$

with the effective magnetic charge density $\nabla \mathbf{M} = \rho_{\mathrm{M}}$. This problem is equivalent to the electrostatic Poisson equation and a general solution can be given using the Green's function for the Laplacian operator ∇^2 as follows [100]:

$$\Phi_{\mathrm{M}}(\mathbf{r}) = -\frac{1}{4\pi} \int \mathrm{d}^3 r' \frac{\nabla \mathbf{M}(\mathbf{r}')}{\mid \mathbf{r} - \mathbf{r}' \mid} \tag{6.9}$$

If we apply this solution to a homogeneously magnetized sphere or radius R with $\mathbf{M} = M\mathbf{e}_z$ inside the sphere and 0 everywhere else in space, the calculation is greatly simplified and the solution for the magnetic scalar potential Φ_{M} becomes

$$\Phi_{\mathrm{M}}(\mathbf{r}) = \frac{1}{4\pi} \frac{\mathbf{m_{tot}} \cdot \mathbf{r}}{r^3} \tag{6.10}$$

where the total magnetic moment of the sphere is $\mathbf{m_{tot}} = (4/3)\pi R^3 M \mathbf{e}_z$, since $\mathbf{M}$ was assumed as homogeneous. This potential is well known from electrostatics as the potential of a single dipole and therefore the field distribution outside the sphere is exactly the same as the field of a single dipole. For differently shaped materials this is only true in the approximation of long distances to the dipole. Inside the sphere the solutions are

$$\mathbf{H} = -\nabla\Phi_{\mathrm{M}} = -\mathbf{M}/3 \tag{6.11}$$

and $\mathbf{B} = \mu_0(\mathbf{H} + \mathbf{M}) = (2/3)\mu_0\mathbf{M}$. It is worth noting that inside the sphere $\mathbf{B}$ is parallel to $\mathbf{M}$ so that it forms closed loops with the flux outside the sphere and $\mathbf{H}$ is antiparallel. The solution for $\mathbf{H}$ is visualized in a sketch in Figure 6.2 a). The above derivation is only true in the limit of homogeneously magnetized objects, e.g. saturated ferromagnets, so that the field equations are linear. Therefore, it can also be expanded to dia- and paramagnetic materials where $\mathbf{B} = \mu_0(1 + \chi_m)\mathbf{H}$ with the magnetic susceptibility χ_m that is positive for paramagnetic and negative for diamagnetic materials. In general the relation between $\mathbf{B}$ and $\mathbf{H}$ in ferromagnetic materials is strongly nonlinear, which leads to the typical hysteresis of ferromagnets. Nevertheless, the above considerations provide a solid idea about the magnetization of homogeneous objects and the concept of an effective magnetic surface charge.

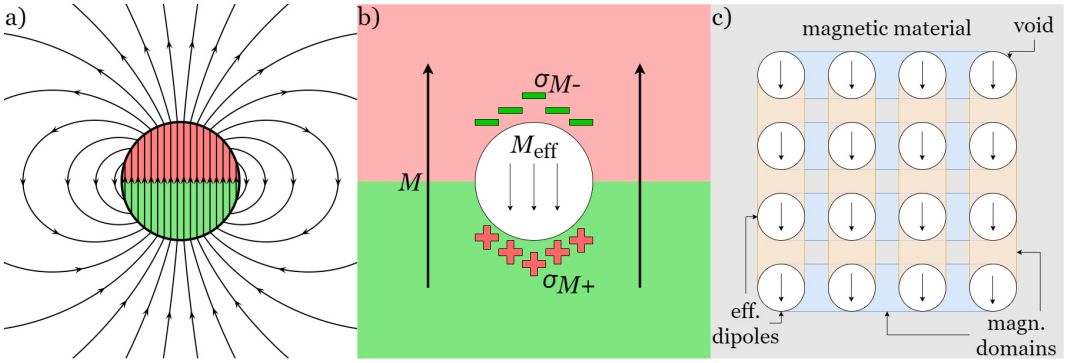

Figure 6.2: Schematic sketch to visualize the idea of nucleation fields in nanopatterned ferromagnets: a) A homogeneously magnetized sphere and its stray field. Image reprinted from [101] under the Creative Commons Attribution Share Alike 4.0 license. b) A hole in a homogeneously magnetized slab generating an effective magnetic surface charge at the boundaries. This object behaves in approximation similar to a homogeneously magnetized particle with magnetization M_{eff} antiparallel to the surrounding material. c) A grid of holes similar as described in b). Close together the holes can couple through dipole interaction and form an ordered domain structure in the surrounding material.

To approach the concept of nanopatterned ferromagnets the given example is now inverted so that everything but the sphere is homogeneously magnetized, as illustrated in Figure 6.2. Instead of considering deliberately created voids in the ferromagnets, it is first beneficial to consider the influence of random magnetic inhomogeneities on the nucleation field of the ferromagnet, i.e. the field where part of the materials magnetization starts to deviate non-uniformly from the coherent state [102]. In a granular system this is easy to imagine as the point where the first

grain's magnetization starts to rotate from the coherent saturated state. For a homogeneous ferromagnet the nucleation field corresponds to the homogeneous rotation of the magnetic moments in the presence of a magnetic field that is aligned antiparallel to the saturated magnetization $\mathbf{M}_\mathrm{S}$. In that context, Kronmüller explored a theoretical model to explain the so-called 'Brown's paradox', where the theoretical coercive field H_C of hard ferromagnets is sometimes ten times larger than the realized values for $H_\mathrm{C}$in experiments with sintered magnets [103]. The following discussion closely follows the considerations made in [103] and [96].
In a homogeneously magnetized ferromagnet the theoretical value for the nucleation field H_N is given by

$$H_\mathrm{N} = \frac{2K_1}{M_\mathrm{S}} - N_\mathrm{eff} M_\mathrm{S} \tag{6.12}$$

with the saturation magnetization M_S, the magnetocrystalline anisotropy constant K_1 and the effective demagnetization factor N_eff. Since this consideration is confined to one axis, none of the symbols are written as vectors. For hard ferromagnets like $Fe_{14}Nd_2B$ the magnetocrystalline anisotropy K_1 is dominant over the shape anisotropy. In real ferromagnets, other microstructural factors lead to a reduction of this theoretical value. Possible inhomogeneities include misaligned magnetic grains, uneven distribution of grain size and grains of a non-magnetic phase. In sintered magnets a non-magnetic phase usually separates the grains as a thin layer that is ideally only a single atom wide, but can cause disturbances when larger grains of said phase form for example as a result of improper thermal treatment. For the purpose of this work, I will concentrate on the contribution of non-magnetic grains, as they can be treated in the same way one would treat voids, i.e. empty grains in the crystal.
To calculate complex magnetization states, the fundamental micromagnetic equations, play an important role. The basic idea behind this system of partial differential equations is that the free energy G should be minimal. Various factors contribute to G like the magnetocrystalline energy E_K where the anisotropy constant K_1 is a factor, the magnetoelastic coupling energy E_ME, the exchange energy E_ex, the magnetic stray field energy E_S and the magnetostatic energy E_H in an external field $\mathbf{H}$. In this example, the magnetoelastic coupling shall be ignored. The total free energy G is therefore:

$$G = E_\mathrm{K} + E_\mathrm{ex} + E_\mathrm{S} + E_H. \tag{6.13}$$

The stray field energy is dependent on the stray field $\mathbf{H}_\mathrm{S}$ which is linked to the magnetic potential Φ_M and the magnetization $\mathbf{M}$ by Eq. 6.8. This calculation can be very involved depending on the shape of the magnetic material and the spatial dependence of $\mathbf{M}$ inside the material, since the continuity boundary conditions that were discussed earlier also have to be met.
A comparatively easy example is the stray field of a spherical void with radius R in a homogeneously magnetized ferromagnet that was introduced in Figure 6.2 b). The z-axis is again aligned parallel to the external field $\mathbf{H}$, like in the previous example of the homogeneously magnetized sphere. The angle between the magnetization $\mathbf{M}$ and the z-axis is called θ and the polar angle in the xy-plane is ϕ, so that the problem can be described in spherical coordinates. In the limit of large external fields θ is small and the magnetization $\mathbf{M}$ has a spherical symmetry of

$$\mathbf{M}(\theta, \phi) = \mathbf{M}(\pi + \theta, \phi) \tag{6.14}$$

everywhere in space, since everything but the hollow sphere at the coordinate origin

is homogeneously magnetized. The normal component of the magnetization M_n can then be expanded into a series

$$M_\mathrm{n}(\theta) = M_\mathrm{S} \sum_{n=0}^{\infty} a_n P_{2n+1}(\cos(\theta)) \tag{6.15}$$

with the Legendre polynomials P_{2n+1} and the expansion coefficients a_n. With Eq. 6.9 follows for the potential Φ_M inside and outside the sphere:

$$\Phi_\mathrm{M,in} = -M_\mathrm{S} R \sum_{n=0}^{\infty} \frac{a_n}{4n+3} \left(\frac{r}{R}\right)^{2n+1} P_{2n+1}(\cos(\theta)) \tag{6.16}$$

for $r < R$ and

$$\Phi_\mathrm{M,in} = -M_\mathrm{S} R^2 \frac{1}{r} \sum_{n=0}^{\infty} \frac{a_n}{4n+3} \left(\frac{R}{r}\right)^{2n+1} P_{2n+1}(\cos(\theta)) \tag{6.17}$$

for $r > R$ using the absolute of the saturation magnetization M_S. With Eq. 6.4 it is now possible to calculate the magnetic field $\mathbf{H}_\mathrm{S}$. In the limit of completely homogeneous magnetization this calculation can be simplified so that the stray field inside the hollow sphere can be written as

$$\mathbf{H}_\mathrm{S,in} = \mathbf{H}_\mathrm{L} = \frac{M_\mathrm{S}}{3} \mathbf{e}_z \tag{6.18}$$

where $\mathbf{H}_\mathrm{L}$ recognizes the field as the so called magnetic Lorentz field. Outside the hollow sphere the effective magnetic surface charge generates a stray field

$$\mathbf{H}_\mathrm{S,out} = -\frac{\mathbf{M}_\mathrm{S}}{3} \left(\frac{R}{r}\right)^3 (2\cos(\theta)\mathbf{e}_r - \sin(\theta)\mathbf{e}_\theta) \tag{6.19}$$

with a z-component

$$\mathbf{H}_\mathrm{S,out,z} = -\frac{\mathbf{M}_\mathrm{S}}{3} \left(\frac{R}{r}\right)^3 (3\cos(\theta) - 1). \tag{6.20}$$

This is exactly the solution for a single magnetic dipole and therefore the solution for a homogeneously magnetized sphere. It is worth noting that in this case, the sign is opposite to the magnetized sphere (c.f. Eq. 6.11 and 6.18), which means that a hollow sphere inside a homogeneously magnetized ferromagnet acts like a ferromagnetic dipole with an opposite orientation to the surrounding magnetization. Looking back at Eq. 6.13, we can see that the free energy G will try to minimize the stray field within the constraints given by the other energy contributions. Therefore, the difference between the actual solution of the micromagnetic equation and $\mathbf{H}_\mathrm{L}$ acts as a gauge for the perturbation in the local magnetization around the void. To compensate for the hollow sphere, the magnetization can do either of two things. First, the magnetization can continuously distort around the hole to minimize the stray field. Second, it is possible to form closing domains around the hole if the energy required to form the domain walls is lower than the stray field contribution. It is expected that this solution will be energetically favorable in the presence of a large number of holes, especially in the case of a hole grid as illustrated in Figure 6.2 c), so that the resulting domains have a regular pattern. This chapter will explore the experimental realization of such structures and discuss the impact of the introduced voids on the magnetic order and the transport properties of thin film systems. A detailed derivation of the micromagnetic equations for the given example of the hollow sphere can be found in [96].

6.1.2 Micromagnetic simulations

The micromagnetic simulations for nanopatterned thin films shown in this work were created with the MicroMagus 7.1ext code package [104]. With this program, it is possible to perform quasi-static simulations to determine the equilibrium magnetization configuration of a system in a given external field. As a consequence, it is possible to obtain a set of magnetization configurations for a complete magnetic field loop using a series of individual calculations. The program additionally produces text output files containing a list of all energy contributions for all simulation steps as well as the total magnetic moments for all applied fields and simulation steps, which allows for the creation of hysteresis loops and, in case of multilayer systems, GMR curves.
In principle, MicroMagus uses the basic equation of theoretical micromagnetics Eq. 6.13 $G = E_\mathrm{K} + E_\mathrm{ex} + E_\mathrm{S} + E_H$, which is known from the previous chapter. For multilayer systems with an interlayer exchange coupling (IEC) like GMR, an additional term for $E_\mathrm{ex}^\mathrm{il}$ is added:

$$E_\mathrm{ex}^\mathrm{il} = -\int_S J_\mathrm{il}^{(12)}(\mathbf{r}) \cdot (\mathbf{m}_1(\mathbf{r})\mathbf{m}_2(\mathbf{r}))\, dV \tag{6.21}$$

with the space-dependent exchange integral $J_\mathrm{il}^{(12)}(\mathbf{r})$ and the space dependent magnetic moments of both involved layers $\mathbf{m}_{1/2}(\mathbf{r})$. The stray field $\mathbf{H}_\mathrm{S}$ that is used in E_H is calculated with a dipole model from the magnetization distribution inside a ferromagnet. Instead of trying to find an analytical solution for the minimal free energy G the program uses a numerical finite difference approach, where the model system is subdivided into a grid and the micromagnetic equation is solved on each grid point. For systems of periodic nanoparticles, or in this case periodic voids in a thin film system, it is useful to employ periodic boundary conditions (PBC), which simplifies the calculation and avoids errors at the boundaries where the translation symmetry is broken. It is worth noting that a key application for the program is the simulation of magnetic particles, which means the input data for the sample structure needs to be inverted for hollow structures. The program requires a geometric input detailing the layer structure and shape, a set of magnetic parameters like saturation magnetization and anisotropy constant, which can be found in literature, and a set of external field values. For polycrystalline samples it is possible to additionally supply a noise pattern with certain dimensions to imitate a random granular structure with an average grain size of d_grain. Detailed information on the involved mathematics can be found on the official program website [104] or in [105] by the same author.
In this work, the micromagnetic simulations of different nanopatterned system are used as an important consistency check between experiment and theory. Given the established model of voids in a magnetic material behaving like magnetic particles of the opposite magnetization, it should be possible to create interesting magnetic microstructures and to potentially enforce certain patterns of magnetic ordering, i.e. domains. These structures can be imaged using differential phase contrast and Lorentz microscopy in the TEM. An agreement of experiment and theory validates both the theoretical model used in the simulation as well as the accuracy of the magnetic imaging experiment.

6.1.3 Lorentz microscopy and differential phase contrast (DPC) in the TEM

In a previous chapter of this work, the transmission electron microscope was used to obtain high resolution images of a sample's microstructure with up to atomic precision. Besides direct imaging, modern transmission electron microscopes can also use a variety of magnetic imaging modes like differential phase contrast (DPC) and Lorentz microscopy. Both techniques are used in this work to characterize the magnetic order in nanopatterned thin films.
Lorentz microscopy exploits the fact that the electron beam in an electron microscope, in this case a TEM, is not only deflected by the Lorentz forces $F_\mathrm{L} = -e(\mathbf{E} + \mathbf{v} \times \mathbf{B})$ of the magnetic lenses, but also by the magnetic field of the specimen. Since this deflection is comparatively small, the specimen needs to be shielded from external magnetic fields. Additionally, this ensures that the magnetic structure of the specimen is not influenced by external sources. To achieve this, either the objective lens closest to the specimen is switched off or a special shielded Lorentz lens is used, so that the immediate surroundings of the specimen remain field free. Due to the nature of the vector product, only magnetic components in the sample plane are detectable [106].
The so-called Fresnel mode operates slightly above or below what would normally be considered in focus. It is used to image magnetic domain walls by either a bright or dark contrast depending on the orientation of the domain wall and whether the focal plane is above or below the specimen. The contrast is generated since the magnetization on opposite sides of a domain wall points in different directions so that electrons passing through on different sides are either both deflected towards the domain wall or away from it [106].
For the differential phase contrast (DPC) magnetic imaging, which operates on a similar principle, the specimen is kept in focus and the total deflection of the beam is measured as well as the deflection angle θ. Using DPC it is possible to map the charge density in thin samples with atomic resolution [107]. Even though the resolution for the magnetic counterpart is not quite as high, recent studies on cross sections of thin films have helped to identify the magnetic microstructure with a high resolution and to link it to the physical microstructure of the specimen [94].
Similar to Lorentz microscopy in Fresnel mode, the specimen needs to be in a field free environment to conduct the measurement. However, the objective lens can be used prior to the measurement to magnetize the sample in a certain direction. The deflection β of the electron in one direction for a thin specimen with the thickness t is given by

$$\beta = \frac{e\lambda}{h} B \cdot t \tag{6.22}$$

with the electron charge e, the electron's wavelength λ, and Planck's constant h. For simplicity, the magnetic induction B is given as a scalar. To map the deflection along with the angle, a segmented annular detector is used, that consists of four inner and four outer elements. The magnetic signal is obtained by calculating the signal difference of opposing detector elements in the outer ring. Using a detector with eight elements as opposed to just four increases the accessible information and reveals finer magnetic detail [93]. The acquired data can be normalized by subtracting the mean value obtained on a region of interest (ROI) that is known to show no deflection like a hole or the vacuum next to the specimen. To prove the magnetic origin of the measured signal, it is necessary to reverse the magnetization of the sample with an external field before a second measurement. If the thickness

of the specimen is precisely known, the data can be used to quantify the magnetic induction within the magnetic material. Further information on both microscopy techniques can be found in [108, 106, 93].

6.2 Optimization of the GMR stack

6.2.1 Sputtering conditions and sample structure

All thin film samples for this project were prepared in a Leybold T11600 custom magnetron sputter system by 3SC Leybold Germany. This machine supports up to eight targets inside the sputter chamber, seven of which are 4" in diameter and a single 2" target. Additionally, an evaporation system in the chamber center is available. Deposition processes can be automated using the programmable control interface of the machine to ensure consistent results across multiple samples. The chamber base pressure p_{base} is less than 10^{-7} mbar and the working pressure under a constant Ar flux of 20 sccm is $p_{\text{work}} = 2.3 \cdot 10^{-3}$ mbar.
Since it was not known beforehand how the differential phase contrast imaging in the TEM interacts with complex thin film systems like the GMR due to the lack of information on the z-axis, simple layers of $Co_{70}Fe_{30}$ with a thickness of 60 nm on a seed layer of 5 nm Py with a capping of 3 nm Ru to avoid corrosion was chosen as a reference sample for the membranes. Since the only requirement on these samples was to provide a specimen that will certainly produce a magnetic signal in the TEM, the specific sputtering conditions were not important and thus set to tried and tested standard values of 29 W for the 2" Py target and 60 W each for the 4" Ru and CoFe targets. The TEM observations in chapter 6.6 on the structured CoFe thin films that were deposited on a 10 nm SiN membrane to keep the specimen transparent for the TEM show a polycrystalline structure for these samples, which is expected on this kind of amorphous substrate.
To investigate the effect of Lorentz fields in more complex magnetic structures, the tried and tested system of Co and Cu was chosen to produce nanopatterned GMR sensors [95]. When giant magnetoresistance systems are concerned, film roughness and layer thickness are critical parameters that need to be carefully controlled in order to produce good results. Especially for current-in-plane systems, the control of interlayer coupling (c.f. chapter 6.2.2) through the thickness of the non-magnetic Cu spacer is of great importance. As the coupling is quite sensitive to variations in the film thickness, deposition conditions with a low sputter rate that still yield smooth films need to be found so that this level of thickness control is possible.
The deposition rate and estimated surface roughness of calibration samples for each material were measured using X-ray reflectivity (XRR) measurements in the Philips/PANalytical X'Pert Pro diffractometer. Details on the measurement technique can be found in [109]. A low sputter rate can be achieved by decreasing the sputter power or increasing the working pressure. Since the latter can increase the surface roughness as well, the lowest power setting that yields a smooth surface, and a reliable and stable plasma ignition was chosen for Cu. The optimized sputter conditions are summarized in Table 6.1. It can be seen that despite the lower sputtering power, Cu is deposited relatively quickly, so sputtering times of layers in the order of a few nanometers are short.

Material	Power [W]	Sputter rate [nm/s]
Permalloy ($Ni_{80}Fe_{20}$)	29	0.2208
Cobalt	60	0.1635
Copper	45	0.2045
Ruthenium	60	0.085

Table 6.1: Optimized sputtering conditions for Co-Cu-GMR thin film systems at a working pressure of $p_{\text{work}} = 2.3 \cdot 10^{-3}$ mbar.

6.2.2 Maximizing interlayer coupling

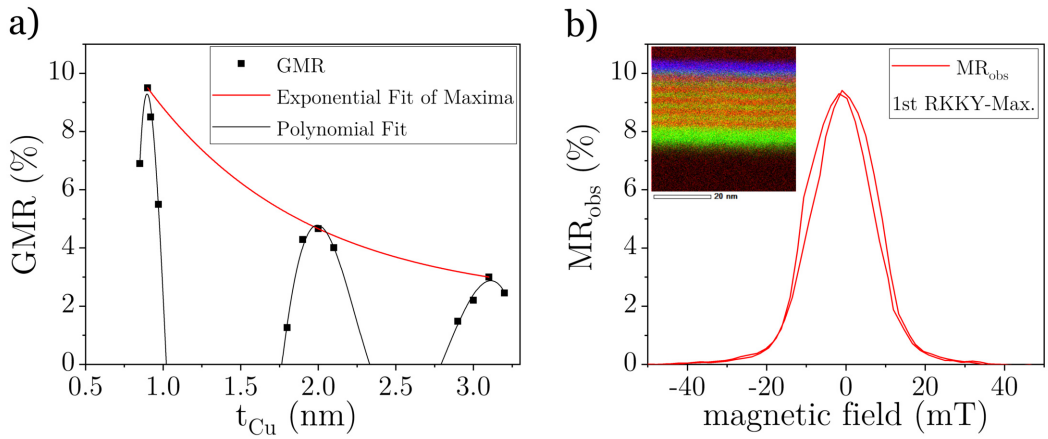

Figure 6.3: a) GMR measurements for Py(3.3 nm)/ Co(2.8 nm)/ [Cu(t_{Cu})/ Co(3.1 nm)]x2/ Ru(3 nm) thin films with varying Cu thickness. The exponential fit shows the characteristic decay of the RKKY-interlayer coupling. A polynomial fit was added to guide the eye and visualize the oscillation of the RKKY-interaction. b) Shows a sample GMR curve measured in the first coupling maximum at $t_{\text{Cu}} = 0.97$ nm. The inset shows an energy dispersive x-ray spectroscopy (EDX) mapping for a cross section of the given film stack and confirms a nice separation of the layers in spite of the low thickness of only a few nanometers. Co is shown in green, Cu is shown in red, and Ru is shown in blue.

The so-called RKKY-interaction is probably the most impactful coupling mechanism between magnetic layers in a current-in-plane GMR system. RKKY refers to the researchers Rudermann, Kittel, Kasuya, and Yoshida who initially proposed the mechanism in an attempt to explain unusually broad nuclear spin resonance lines through a perturbation theory approach [110, 99]. In the original description, nuclear spins would interact with one another through indirect exchange coupling using a conduction electron. Monte Carlo simulations for the transport of itinerant spins in a system of antiferromagnetically coupled multilayers with non-magnetic spacers of variable size by Akabli *et. al.* [111] help to visualize the nature of the interaction. They have shown that the RKKY-interaction J oscillates with the distance between spins r_{ij} for two spins across the non-magnetic layer.
Considering a multilayer system of unbiased free magnetic layers separated by a spacer of thickness t, this means that adjacent ferromagnetic layers will couple ferromagnetically or antiferromagnetically depending on t. An easy playground image

to visualize this is to imagine a magnetic moment injected into an otherwise non-magnetic material. The spins in that material would try to compensate this moment by orienting themselves opposite to the injected moment. This would create a ripple effect until equilibrium is reached at a certain distance from the injected spin.
To maximize the giant magnetoresistance effect in a multilayer system, antiferromagnetic coupling between the layers at $H_{\text{ext}} \approx 0$ is desired, which means the spacer thickness needs to be chosen accordingly. When the magnetic layers couple ferromagnetically at all times, the GMR effect is diminished significantly or could vanish completely. In order to find the optimal thickness of the Cu spacer t_{Cu}, a series of multilayers with different amounts of Cu was fabricated. The sample structure was Py (3.3 nm)/ CoFe (2.8 nm)/ [Cu (t_{Cu})/ Co (3.1 nm)]x2/ Ru (3 nm) for a total of three magnetic layers with two spacers. Technically speaking three layers would be sufficient to produce a GMR, however, using more layers alleviates problems with film roughness that can occur for polycrystalline films on amorphous substrates. Additionally, more layers increase the GMR so that a higher signal-to-noise ratio is achieved.
The results of the transport measurements are illustrated in Figure 6.3 a) where the exponential fit to the maxima of the three distinct peaks shows the expected exponential decline in the coupling strength. A polynomial fit was added to guide the eye, as the actual analytical expression for the interaction is quite complex and hard to fit to a low amount of data points. Figure 6.3 b) shows a sample GMR measurement for the first RKKY-maximum at $t_{\text{Cu}} = 0.97\,\text{nm}$. The inset shows an energy dispersive x-ray spectroscopy (EDX) image taken from a cross section of a GMR stack. Co is shown in green, Cu in red, and Ru in blue color in this overlay. All layers are nicely separated and show no signs of interdiffusion. It is worth noting that the EDX mapping shows a sample with 5 Cu-Co multilayers from an early test cycle. The sputtering conditions were the same as for the Py (3.3 nm)/ CoFe (2.8 nm)/ [Cu (t_{Cu})/ Co (3.1 nm)]x2/ Ru (3 nm) samples that were used for the transport measurements.
We decided to reduce the total number of layers so that micromagnetic simulations of the GMR system would require less computation power. The final values for the Cu thickness determined from the experiments are $t_{\text{Cu,1}} = 0.97\,\text{nm}$ for the first RKKY-maximum, $t_{\text{Cu,2}} = 1.9\,\text{nm}$ for the second and $t_{\text{Cu,3}} = 3.0\,\text{nm}$ for the third RKKY-maximum. Since a total film thickness of 50-80 nm is desirable for differential phase contrast imaging, because the beam deflection is proportional to the magnetic material's thickness, the number of Cu-Co multilayers was increased for the GMR membrane samples to Py (3.3 nm)/ CoFe (2.8 nm)/ [Cu (t_{Cu})/ Co (3.1 nm)]x12/ Ru (3 nm). In the context of GMR measurements, the RKKY-interaction is also often referred to as interlayer exchange coupling (IEC).

6.3 Focused ion beam structuring of CoFe and GMR membranes

The patterning of the coated SiN membranes was done in the Helios Nanolab 600i dual beam system via focused ion beam milling. To make the structures even and repeatable across multiple samples, the basic scripts used to create Co-nanoparticles in chapter 4 were adjusted to produce the desired shapes on a rectangular grid. All shapes were milled at an acceleration voltage of 30 kV with an ion beam current of 9.7 pA to ensure the highest possible resolution.

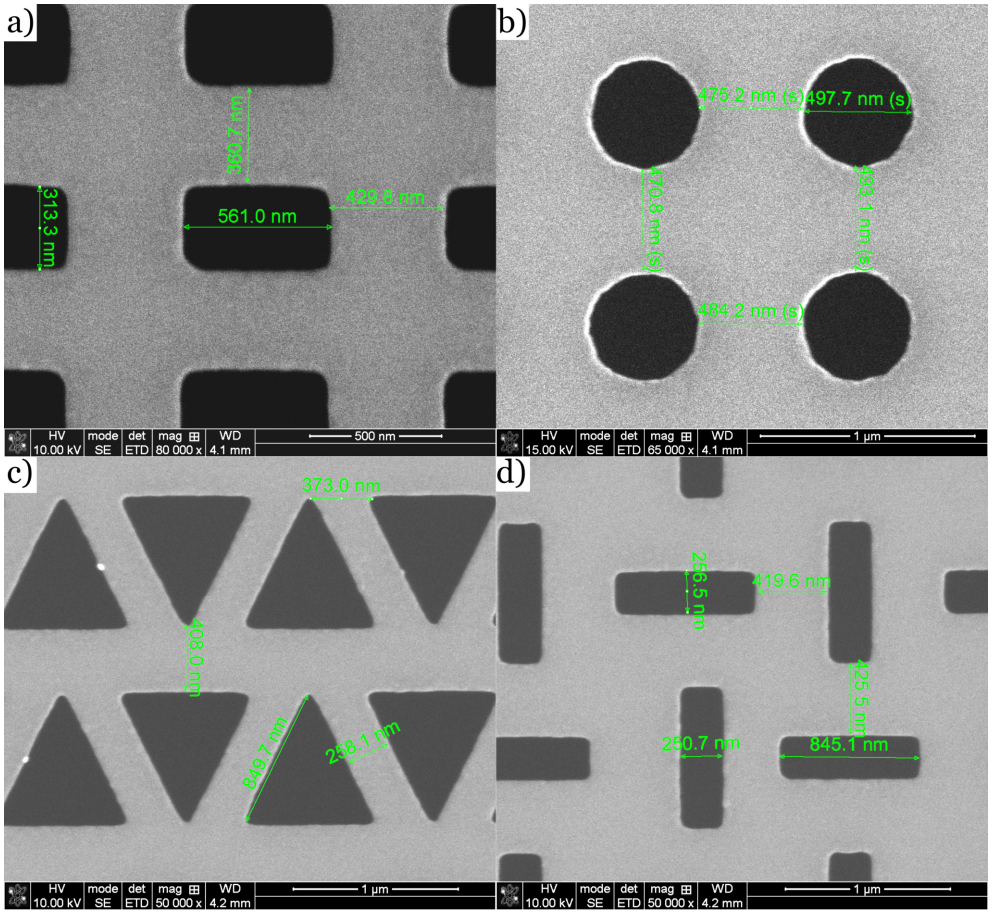

Figure 6.4: SEM images of the patterned CoFe thin films on a 10 nm SiN membrane: a) rectangles, b) circles, c) triangles d) herringbone parquet. The holes were cut using the focused ion beam in the Helios Nanolab 600i with a semi-automated script. For the GMR samples, the exact same scripts were used. Precise measurements can be found in the respective image.

While the 50 μm square membrane window that is located at the center of a 5 mm SiN disc is easy to locate since 10 nm of SiN produce a significantly lower amount of secondary electrons than the surrounding wafer, the window becomes difficult to locate once the metal film is deposited on top. To alleviate this problem, the electron beam acceleration voltage had to be increased to 15 kV instead of the usual 5 kV that is used for surface sensitive imaging. The higher penetration depth of the beam at 15 kV helps to locate the window. The sample has to be carefully aligned at the eucentric height so that the electron and ion image match exactly before moving

onto the membrane window since the coated membrane is invisible in the ion image and easily damaged. On the other hand, the redeposition of material sputtered by the ion beam, which is usually a concern for larger milled structures, is not a problem with membrane substrates, as the material is thin and the ion beam passes through the entire sample without getting "stuck" in the substrate material.
Figure 6.4 shows the four patterns that are investigated in this work including their respective measurements. With a minimum structure size of about 250 nm for the triangle and herringbone parquet pattern in Figure 6.4 c) and d), the holes are comparatively large. Using the FIB at the given beam parameters, it is possible to create circular structures of less than 100 nm. With the goal of magnetic differential phase contrast imaging that is performed at low magnifications in the TEM in mind however, larger structures are easier to extract reliable magnetic information from given the resolution limitations of the DPC measurement. Additionally, the mechanical stability of the patterned membrane would be a concern for densely packed smaller structures since the ion beam locally heats the specimen and the free membrane is not a particularly effective heat sink compared to conventional thicker substrates. This is especially important for the GMR membranes since heat-induced interdiffusion in the exceptionally thin layers can easily destroy the effect. Therefore larger structures are beneficial for the goal of this project.
Whereas the rectangle and circle patterns in Figure 6.4 could be scripted using just the basic commands outlined in chapter 3, the triangle and herringbone parquet pattern required a little more effort. Since the microscope control software does not support triangles as a basic shape, the triangles were drawn using the "polygon" command, where the x- and y-coordinates of each corner can be specified. To optimally fill the space, the unit cell for the triangular pattern consists of two triangles, one of which is inverted. The unit cell is then repeated on a rectangular grid. Similarly, the herringbone parquet pattern consists of a unit cell of four rectangles that are placed in a vortex-like pattern as shown in Figure 6.4 d). Due to a small error in the programming, every second horizontal gap in every second row is roughly 100 nm smaller. This will be considered in the discussion of the results.
The presented shapes were chosen for their different symmetry properties, even though they are technically all ordered on a rectangular grid. Given that the Lorentz-field means, that the voids can be seen as a magnetic particle of a magnetization opposite to the surrounding magnetic material (c.f. chapter 6.1.1), the shape anisotropy of the rectangle that has an aspect ratio of roughly 2:1 could have interesting effects on the formation of magnetic domains. Circles on the other hand are isotropic defects. Since it is well known that grain boundaries, and by extension of that fact holes in the magnetic material, can act as nucleation and pinning centers for magnetic domain walls [112, 85], a different pinning behavior during a magnetic reversal loop is expected for defects of different symmetry. The triangle shape was chosen for the same reason.
In an attempt to introduce forced magnetic frustration into the patterned films, the herringbone parquet pattern was inspired by works on artificial spin ice. Recent experiments by Branford *et. al.* on isolated magnetic islands arranged in the famous Kagome lattice pattern showed interesting chiral magnetic structures [89]. Though it is not quite as complex as the Kagome lattice, the herringbone parquet fabricated for this work could facilitate unique magnetic states in the magnetic film.

6.4 Electron beam lithography nanopatterning for transport measurements

Besides the accuracy of the fabrication method, the preparation time also needs to be considered for larger GMR structures that are used for electrical transport measurements. Since the effective interaction range of a magnetic dipole is small, it is a reasonable assumption that any effect of the magnetic ordering induced by the Lorentz field of the patterned structure is confined to the immediate vicinity of the pattern. Therefore, the impact of the patterning on the observed magnetoresistance MR_{obs} should scale with the ratio of patterned material to unpatterned material. As the high amount of machine time needed for larger structures is one of the main drawbacks of focused ion beam milling, the samples for electrical measurements were fabricated using electron beam lithography.

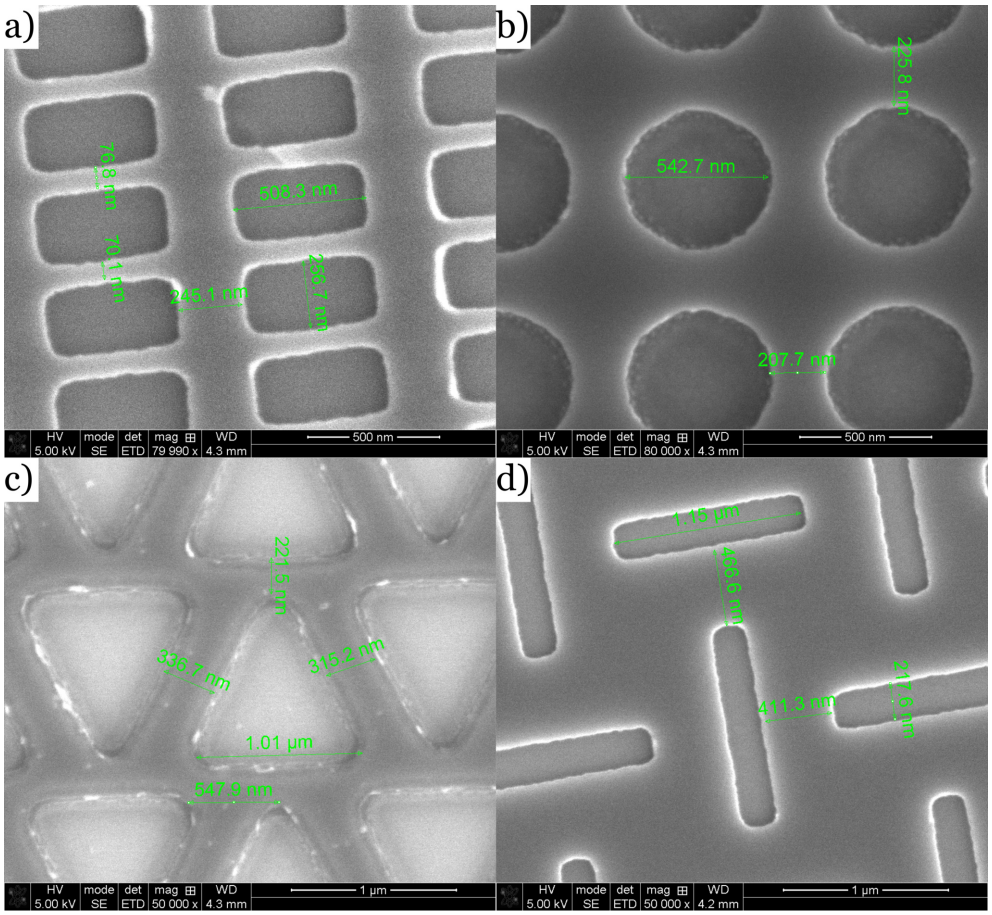

Figure 6.5: SEM images of nanopatterned GMR thin film stacks on a regular Si wafer for transport measurements: a) rectangles, b) circles, c) triangles, d) herringbone parquet. Exact measurements can be found in the images. Due to the different fabrication method, the measurements are not completely identical to the patterned membranes.

To maximize the patterned area while keeping the fabrication time at a reasonable level, the GMR thin film stacks were patterned into bar shapes with the pattern stretching along the entirety of the roughly $10 - 15\,\mu$m wide bar, depending on the

respective pattern. Larger contact pads were added to both ends of the bar for easier measurement. After the deposition of the Py (3.3 nm)/ CoFe (2.8 nm)/ [Cu (t_{Cu})/ Co (3.1 nm)]x2/ Ru (3 nm) thin film system on a Si wafer, AR-N 7520.18 negative e-beam resist was applied (c.f. chapters 2.1 and 5.2.4). Following the exposure in the Zeiss LEO 1530 SEM and development in AR 300-47 developer, excess material was removed through ion milling in a secondary ion mass spectrometer (SIMS). The resist protects the thin films in the desired areas, while the milled ions from the surrounding area are monitored in the mass spectrometer to track the milling progress. The lift-off of the excess resist was done for 10-15 minutes in an ultrasonic bath using NMP as a solvent. While it is technically faster to use a positive resist on an empty wafer and expose the structure before sputtering, because it saves the milling time in the SIMS, the use of negative resist has a few benefits. First, the achievable resolution in AR-N 7520.18 negative resist is higher than for a comparable positive resist AR-P 617.08. Second, using a negative resist after sputtering the thin films means, that it is possible to batch produce multiple samples without having to wait for the lithography, which is the time bottleneck in the process. After application, the resist remains usable for 24-48 hours at best before results start to noticeably deteriorate. When a single exposure can take 6-15 hours depending on the pattern, it is not feasible to prepare several samples with positive resist at the same time, which in turn blocks a lot of time on the sputtering machine.
Figure 6.5 shows SEM images of the structured GMR thin films including the respective measurements of the structures. These structures closely resemble the patterns in the TEM samples for DPC measurements that were patterned with the focused ion beam. Due to the broadening of the structures because of scattered secondary electrons, the measurements of the densely packed structures differ slightly. Unlike the previous structures on a SiN membrane, on a sturdy Si wafer substrate it is possible to pack individual features closer together without fear of breaking the sample entirely, for example by ripping the membrane. Thus, bars as narrow as 70 nm could be created in the rectangular grid in Figure 6.5 a). Since the total height of the GMR stack is below 20 nm, it is possible to thin the e-beam resist (c.f. chapter 5.2.4) to more accurately control the pattern size and shape.

6.5 Results

6.6 TEM analysis of nanopatterned CoFe membranes

To get a better understanding for interpreting magnetic differential phase contrast images from the TEM analysis of nanopatterned magnetic thin films, it is useful to first examine results from simple structured samples that are sure to produce a magnetic signal.
This is also important to gauge the utility of physical interpretations derived from complex multilayer systems like GMR samples, since the impact of different magnetic contributions along the z-axis, i.e. the stacking axis, is unclear. In this case, the reference samples consist of 60 nm of $Co_{70}Fe_{30}$ on a 5 nm Py seed layer to promote smoother growth. A 10 nm SiN membrane was used as a substrate and the film was capped with 3 nm of (non-magnetic) Ru to avoid corrosion.
Since there is no spacer between the Py and CoFe layer, no RKKY-coupling needs to be considered and the sample behaves like a single soft-magnetic layer, which is ideal for magnetic imaging. The membrane was patterned using the focused ion beam and contains all structures discussed in chapter 6.3 as well as a single large square hole with an edge length of 2 μm. While this was originally intended as a reference to subtract the background signal from the data, it also serves as a demonstration for the imaging of domains and domain walls using Lorentz microscopy and DPC.

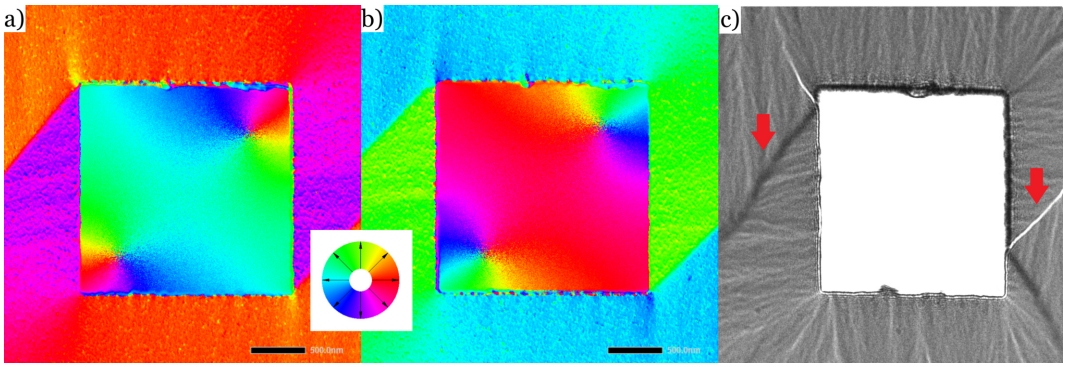

Figure 6.6: a) DPC image of a square hole in the CoFe membrane. The sample was magnetized by the objective lens by tilting the specimen to -25° before switching the objective lens off to take the DPC image. b) DPC image of the same region after magnetizing in the opposite direction through a +25° tilt. c) Lorentz-TEM image of the same region using Fresnel mode to see domain walls (marked with arrows). The Lorentz-image agrees well with the results from the DPC images.

Figure 6.6 a) and b) show the differential phase contrast images of said square hole, where the color wheel indicates the direction of the magnetic induction. In a) the image was taken after tilting the specimen to -25 ° with the objective lens turned on to get an in-plane component to the magnetic field. The objective lens was then switched of and the specimen was tilted back to 0 ° for the imaging. Similarly, the sample was tilted to +25 ° to obtain the image in b). By the nature of the DPC imaging process, the imaging itself takes place in a mostly field free environment except for a possible remanence of the objective lens. This means that the imaged magnetic configuration represents a structure close to remanence magnetization of

the sample. Since magnetic thin film samples have a high shape anisotropy so that in-plane magnetization is preferred, the z-component of the objective lens' magnetic field is assumed to be negligible in this case. Figure 6.6 c) shows a Lorentz microscopy image in Fresnel mode of the same region. As discussed in chapter 6.1.3 domain walls are indicated by lines of much brighter or darker contrast compared to the rest of the magnetic material. These domain walls are marked with red arrows. It can be seen that the lines from the Lorentz image agree well with the color pattern in the DPC images. Furthermore, a closer look at the color wheel reveals that between a) and b) the magnetic induction does indeed point in opposite directions for each region as it is expected for a magnetic signal. Technically speaking all matter displaces the electron beam and produces some form of DPC signal, however, a reversal of the signal after experiencing an external magnetic field clearly proves the magnetic nature of the color contrast. This means that DPC microscopy is useful for imaging magnetic domain structures in magnetic thin films.
From Figure 6.6 a) and b), a few common artifacts in differential phase contrast imaging can also be discussed. First, since the beam deflection in the TEM is proportional to the thickness of the material that the electrons travel through, one would expect holes to produce zero signal. However, to measure the shift caused by magnetic induction accurately, the beam is aligned to the center of the detector while passing through the unmagnetized material, which effectively creates an offset. When the beam passes through a hole, this base deflection is missing, which causes the non-zero signal from inside the hole. While it is possible to remove this signal by normalizing the signal with the integrated average over the hole, it is not necessary to interpret the data from the actual magnetic material. Furthermore, stray fields in larger holes can also interact with the beam which causes the rainbow vortices in the corners of Figure 6.6 a) and b).
Similarly, the hole fringes that sometimes appear in rainbow colors are just artifacts caused by the discontinuity of the magnetization at the edge and additional scattering events that occur at the uneven edges. They are not useful to derive a physical interpretation from the image.
Lastly, when imaging larger areas with differential phase contrast like the following images of the hole grids, a steady color gradient across the entire specimen can often be observed. This is caused by the beam deflection that is necessary for scanning the image, which means that the beam will hit the specimen at different angles and therefore also experience a slightly different deflection. For the interpretation of the images, this gradient needs to be ignored. Sharp color changes like for the domain walls in Figure 6.6 can still be observed even in larger scanning areas and have been proven to be of magnetic origin.
It should be noted, that the color representation of DPC images in general depends on a number of different factors like the scanning direction of the beam, the orientation of the sample and the relative angle of both sample and scanning direction to the magnetizing field. While it is possible to account for these factors, considerable effort is required to program an image correction routine for this application, that goes beyond the scope of this work. As a result, the color wheel in all DPC images in this work can only accurately serve as a guide to eye to discern the relative orientation of the imaged magnetic structures to one another. The actual direction of the magnetic induction might be obscured by the factors explained above. For all micromagnetic simulations, however, the color wheel is an accurate representation of the magnetization.

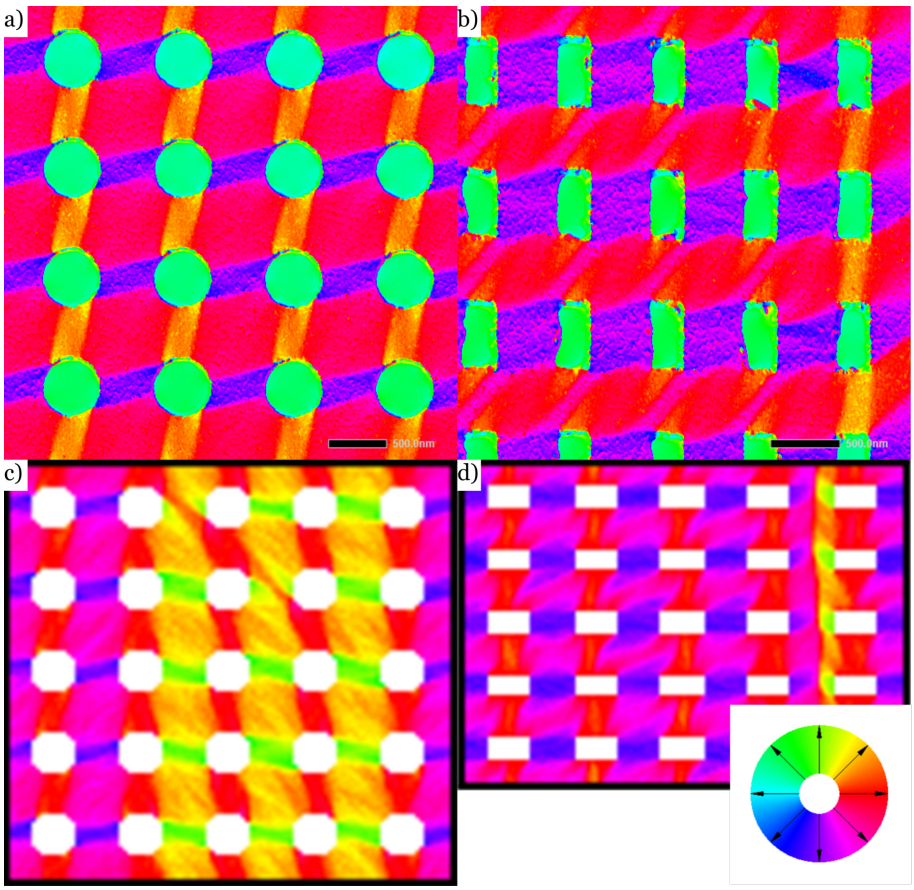

Figure 6.7: Comparison of DPC images from the patterned CoFe membrane a) 500 nm circles and b) 500 nm x 250 nm rectangles to the respective micromagnetic simulations c) circles and d) rectangles. For the DPC images the specimen was magnetized by the objective lens at a tilt of -25°. Images were taken with the objective lens switched off, i.e. at remanence magnetization. Small fields could be present due to remanence magnetization of the objective lens itself. Simulation results are extracted from a full magnetic reversal loop at c) 1 mT and d) -2.5 mT. The measurement used in the simulation were extracted from the SEM images of the respective patterns.

Figure 6.7 a) and b) show the differential phase contrast images for the circle and rectangle pattern shown in Figure 6.4, as well as micromagnetic simulations of the magnetic order in these structures (c and d). The membrane was tilted to -25 ° prior to the image acquisition to magnetize the specimen, whereas the image was taken with the objective lens switched off. Thus, the image should represent a state close to remanence magnetization depending on any external fields induced by the remanence of the objective lens. For the simulations, the measurements of the patterns were extracted from their respective SEM images with only slight alterations to simplify the node placement for the simulation program. The exact measurements used for the calculation are 496 nm circles with a distance of 472 nm between them (c) and 472 nm by 240 nm rectangles with a spacing of 448 nm (d). Full magnetic reversal loops were calculated and the images presented in Figure 6.7 c) and d) are taken

from the -1 mT and -2.5 mT points in the loop, respectively. In the DPC images, the external field during the magnetization process was not exactly parallel to either of the lattice axes in the pattern, which was assumed in the simulation. Therefore, the orientation of the pattern in b) and the color representation in both a) and b) are not completely identical to the simulations. However, it is easily visible that the simulation qualitatively represents the observed structure quite well.
For the circle structure in Figure 6.7 a) and c), domains clearly form between nearest neighbors. In the simulation, these domains are partly oriented perpendicular (green) to the external field on the x-axis, which is not the case for the DPC observation. This could, however, be due to the aforementioned misalignment of the external field and the pattern's lattice. It is worth noting that even in the simulation where axes are aligned perfectly, the domain walls are slightly askew compared to the lattice axes, which could indicate that the periodic pattern inhibits a free rotation of the magnetization by creating stable configurations at an angle to the external field. This is very similar for the rectangle pattern, where the simulation, ignoring the orientation of the rectangles, nicely resembles the observed domain structure. Here, diagonal domains that connect opposite corners of adjacent rectangles are also found. In general, the color representation in both b) and d) matches almost perfectly, which is likely due to the symmetry of the pattern so that the roughly 90 ° rotation produces comparable results. Especially from the yellow domains toward the right side of b) and d), it can be concluded that domains likely nucleate at the corners and are also in part pinned to them, which creates this regular and relatively stable domain pattern. Additionally, the slight angle between the external field and the lattice axis does not seem to have as much impact on the domain structure in the rectangle pattern as in the circle pattern.

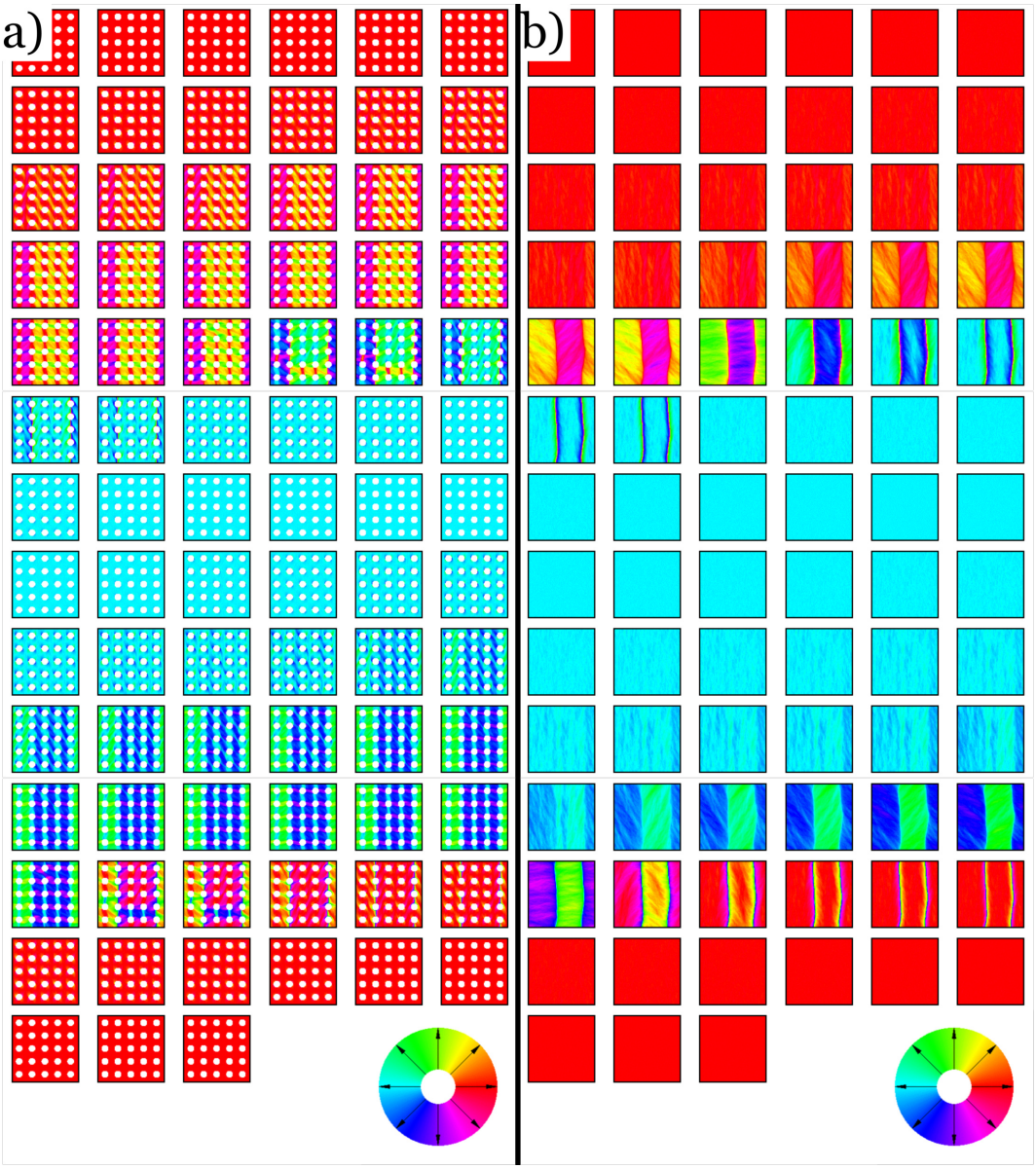

Figure 6.8: Comparison of a full magnetic reversal loop simulation for a patterned CoFe membrane with a) 496 nm holes with a spacing of 472 nm in x- and y-direction to b) an unpatterned free CoFe layer.

A direct comparison of simulations of a full magnetic reversal loop for the circle pattern and a homogeneous magnetic film without any defects shows a few more interesting properties of the patterned system. The loop is presented as a series of images showing the magnetic configuration in Figure 6.8 a) with the circle pattern and b) without it. Both simulations used the same material parameters and step sizes for the external magnetic field in a range from -1000 mT to +1000 mT. Since the material is soft magnetic, the step size is decreased close to $H_{\text{ext}} = 0$, where the magnetic ordering is most interesting. A detailed image of the same simulation for the rectangular pattern can be found in the Appendix along with the step sizes for H_{ext}. For the considerations in this chapter, the qualitative results of the simulation are sufficient. As the MicroMagus program uses periodic boundary conditions for this calculation, the area in which the magnetic switching first occurs is arbitrary. In a real system, the nucleation of domains would most likely start at the edges or defects in the crystal structure.
The side by side image in Figure 6.8 shows that for a magnetic film with a hole grid, domains that are rotated compared to the field axis form at much higher fields than for an unpatterned film. These domains that are mostly located between neighboring structures are stable over a large field range. Even so, the value for H_{ext} where the switching of the magnetization occurs rapidly, i.e. H_{C} seems to be mostly unaffected. It can also be seen that the nucleation of domains starts around the holes, where they are aligned at a 45 ° angle to the external field. At lower fields, stable domains at a 90 ° angle (green) start to form. Domains in the unpatterned film are considerably larger and can rotate freely, hinting at a pinning effect of the holes. The result for a grid of rectangular holes (c.f. Appendix) is qualitatively similar. For this pattern, the nucleation of domains starts at the corners of the rectangles and H_{C} is slightly higher at roughly 10 mT compared to the pattern with circular holes where $H_{\text{C}} \approx 5$ mT. This is likely a result of stronger pinning at the corners of the rectangles.

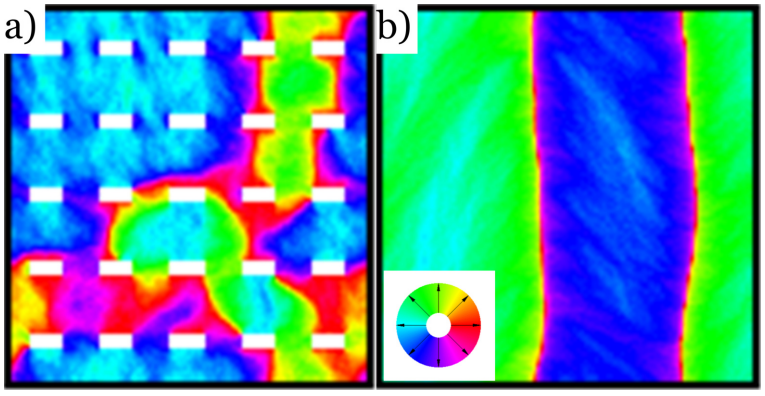

Figure 6.9: Comparison of a micromagnetic simulation of a) 432 nm x 224 nm rectangles with a spacing of 448 nm in the x-direction and 688 nm in the y-direction taken from a magnetic reversal loop at -2 mT to b) a free CoFe layer taken from the reversal loop at -7.5 mT.

Figure 6.9 a) shows an image taken from a simulation of a full magnetic reversal loop at -2 mT for a rectangle pattern of 472 nm by 240 nm with a distance of 448 nm in x- and 688 nm in y-direction. In contrast Figure 6.9 b) shows part of the reversal loop in Figure 6.8 b) of an unpatterned CoFe film at -7.5 mT. In this case the domain

structure of the patterned sample looks more chaotic since domains are not confined to the spaces between the holes. Additionally, many parts of the domain wall are not pinned to the corner or edge of a hole, but instead form an arbitrary pattern in the spaces in between. Since the only difference to the rectangular pattern shown in Figure 6.7 b) is the distance between the holes in y-direction, the formation of stable domains appears to be heavily dependent on the distance between individual structures. Compared to Figure 6.9 b), the magnetic domain structure in a) looks qualitatively similar, but perturbed by the rectangular holes. In the model of these magnetic voids acting like a dipole of the opposing magnetization (c.f. chapter 6.1.1), the holes only have significant impact on the magnetic ordering of the thin film when the distance between dipoles is smaller than an effective interaction range d, where d is in the order of the hole size D. For larger distances the system can find other ways beside the regular magnetic domain pattern to minimize its free energy G. To achieve a maximum effect from the dipole coupling of the hole pattern, structures should be packed as densely as possible within the possibilities of the manufacturing process.

6.6.1 Summary for simple magnetic layers

Before continuing with the investigation of nanopatterned multilayer GMR systems, I will briefly summarize some key results up to this point. First, Lorentz microscopy and differential phase contrast imaging have been proven to produce high resolution images of the magnetic ordering in CoFe thin films that are consistent with one another. Being able to resolve the lateral orientation of the magnetic induction and by extension of that the magnetization in the film, this technique is far more powerful than other well-known magnetic imaging methods like magnetic force microscopy (MFM), the only downsides being the elaborate sample preparation process and the lack of information in the axial beam direction, which in most cases means the z-direction of the thin film system.
Second, micromagnetic simulations using the MicroMagus 7.1 software were shown to produce results that closely resemble the observed magnetic structure with DPC. Since both methods use different physical approaches and yet produce mostly consistent data, the results in this project make a strong case for a simulation-guided approach to more complex hole patterns that produce interesting magnetic results.
Lastly with regard to the imaging of GMR systems, or systems of magnetic multilayers in general where the influence of possibly antiparallel magnetic regions in the axial beam direction is unclear, differential phase contrast could provide unique new information on the antiparallel state that is responsible for the increased resistance. Most information on GMR sensors is derived from either measurements of the microstructure using the TEM, atomic force microscopy (AFM), or electrical transport measurements. However, with DPC it could be possible to directly image the magnetic configuration of such systems, which will be explored in the next chapter.

6.7 Characterization of nanopatterned GMR systems

Besides the uncertainty in which way the magnetic structure in the z-direction influences the DPC signal, a second interesting question is whether the patterning of the sensor has significant impact on the shape of the observed magnetoresistance MR_{obs} as a function of the external field H_{ext}. Since the influence on the magnetic order in simple ferromagnetic thin films can be modeled with magnetic dipoles, these moments can interact with or perturb the interlayer exchange coupling (IEC) in the RKKY-model. Therefore, the patterns presented in the previous chapter will be investigated for different RKKY-maxima to discern the influence of the coupling strength on the results. If both energies are of roughly the same magnitude, their respective effects can compete with each other.

6.7.1 Results for simple shapes on a rectangular grid

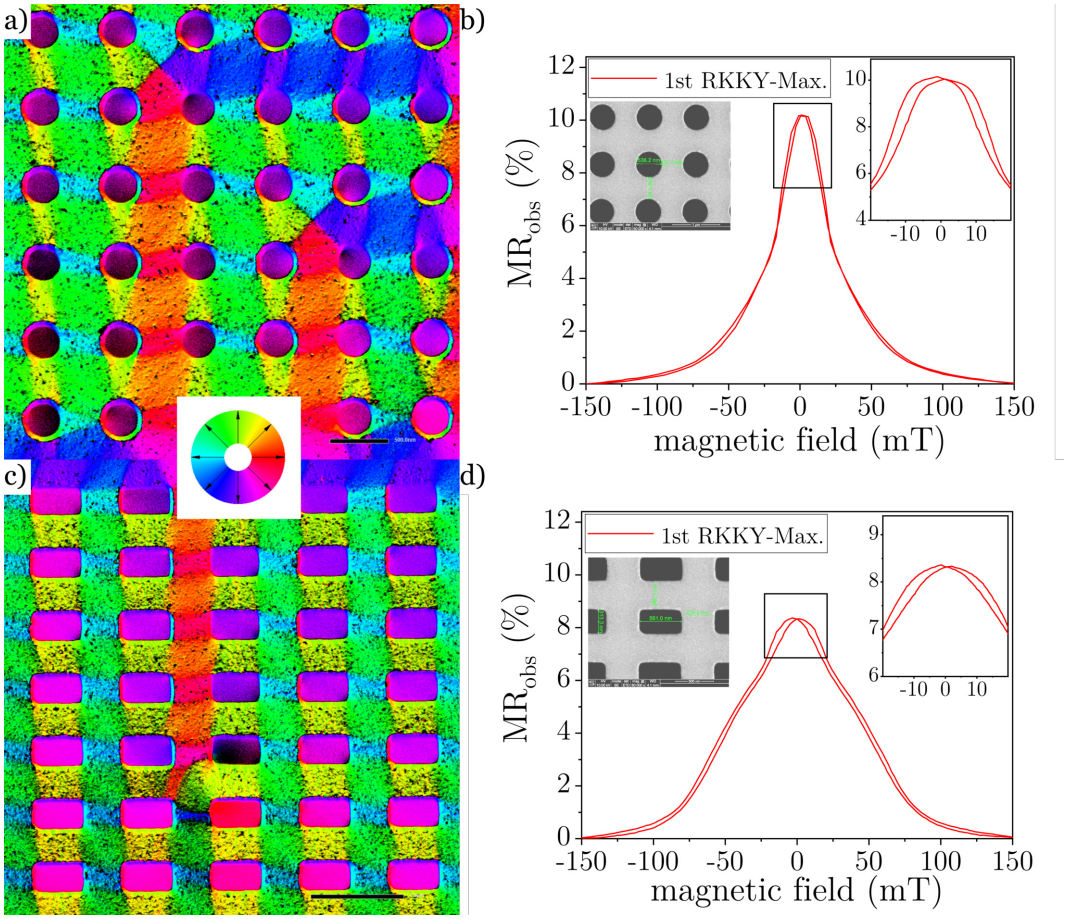

Figure 6.10: Results for the first RKKY-maximum: a) DPC image of 500 nm circles and the corresponding GMR curve b) for the same pattern on a Si wafer using e-beam lithography. b) DPC image of 500 nm x 250 nm rectangles and the corresponding GMR curve for the same pattern on a Si wafer using e-beam lithography. The insets in b) and d) show a zoom on the respective peak region and a reference to the SEM images of the pattern.

Figure 6.10 compares the DPC images and the respective transport measurements for GMR samples at the first RKKY coupling maximum with a circle pattern (a, b) and a rectangle pattern (c, d). The same script that was used for the circle and rectangle pattern in the CoFe-film from Figure 6.4 was also used for the GMR samples. Since the Cu-Co multilayer mills faster, the rectangles in this case exhibit less grainy fringes in the holes. With a differece of a few nanometers due to the increased milling rate, the measurements for both the CoFe and the GMR samples are identical. It is worth noting, however, that even though both films were magnetized at a tilt angle of -25 ° just like in chapter 6.6 before the objective lens was turned off for the imaging process, the colors do not match perfectly.
One important factor for the color shift is the rotation of the specimen with regard to the scanning direction and the magnetizing field, which was explained in the previous section. Even though reference markers were placed on the SiN wafer, due to the size of the sample a perfect alignment is very difficult. A second important reason for a shift in color lies in the multilayer nature of the GMR sample. In this case the DPC image represents a superposition of all individual layer contributions, which can result in more complex observed patterns. Since multiple magnetic layers, that are antiferromagnetically coupled at $H_{\text{ext}} = 0$ due to the RKKY-interaction, are present and the DPC images are taken at close to remanence conditions in the TEM, it is possible that the beam deflection is integrated over a series of magnetic layers with different alignment. This results in a "net induction" that represents something like the average in the axial direction. That is, if the beam deflection is approximated as linear.
Even so, comparing the domain pattern in Figure 6.10 a) and c) to the emerging pattern in Figure 6.7 a) and b) for a simple CoFe sample, both show clear similarities. In both cases domains that are rotated by 45 ° or 90 ° (e.g. green to yellow or light blue to green) with regard to adjacent domains form in the spaces between neighboring holes, hinting at a stabilization of these states by the dipole interaction between the holes. Additionally, so-called Landau patterns emerge in Figure 6.10 a) in the center between four circles at several places in the pattern. These states consist of four distinct domains that are oriented at a 90 ° angle to adjacent domains around a vortex core. It is unclear whether these vortex cores are located at a crystal defect or grain boundary that is at the center by coincidence or whether these Landau patterns are metastable states as a result of a combination of the interlayer coupling and the magnetic ordering induced by the hole pattern. Since DPC can not resolve the magnetic structure in the direction of the thin film stack, the effect of the hole pattern on the interlayer coupling can not be imaged. However, the electric transport measurements of the respective patterns on a Si wafer, which acts as a heat sink and offers mechanical stability, shown in Figure 6.10 b) and d) provide a few hints.
One of the most obvious findings in these measurements is the fact, that the maximum observed MR ratio MR_{obs} is mostly unchanged compared to the unpaterned sample in Figure 6.3 b). For the circle pattern in Figure 6.10 b) it is about 1 % higher and for the rectangle pattern it is about 0.5 % lower, which lies within the margin of error given that the system is extremely sensitive to minimal deviations in the thickness of individual films. This means, that the interlayer coupling is not destroyed by the patterning and in fact seems to be mostly unaffected by the Lorentz fields caused by the holes.
Compared to the unpatterned GMR, the measured curve for the patterned sam-

ples shows a broadening at the peak, that is stronger in the rectangle pattern than in the one with circles. Whereas MR_{obs} is almost halved for the unpatterned film at 10 mT, the circle pattern loses just about 20% of the maximum amplitude and the rectangle pattern only loses about 10%. This indicates that the Lorentz field, while it does not directly interact with the interlayer exchange coupling, stabilizes the antiparallel state by stabilizing the magnetic domains in the spaces between the holes. Additionally, a pinning effect of the domains manifests itself in the higher coercive field H_C that results in a broadening of the curve, especially on the tails of the peak. At 30 mT MR_{obs} is almost at 0 % for the unpatterned film, however, for the circle pattern more than 100 mT are needed to align the magnetic layers parallel so that MR_{obs} vanishes. As discussed previously, pinning is strong at point defects or sharper corners. As such this effect is more pronounced in the rectangle pattern, where the flanks of the MR_{obs} peak are almost linear, which is potentially useful for a practical application of such a sensor.
Given the large differences of the magnetic properties of the Cu-Co multilayers to simple CoFe-films, the similarity of the observed domain structures in both systems as well as the similarity to the micromagnetic simulations of CoFe-films is surprising. Since micromagnetic simulations for simple CoFe films have been reliable for predicting the observed magnetic order, the results from chapter 6.6 help to form a hypothesis about the origin of the change in the GMR curve. The simulations have shown that rotated domains start to nucleate at higher fields for patterned magnetic layers than for continuous thin films. Additionally, the Lorentz field of a periodic hole pattern seems to stabilize domain patterns that can have an angle of 45 ° or 90 ° with regard to H_{ext}. As the IEC is strong compared to the dipole interaction between the holes, it is possible that these perpendicular domains also maintain an antiparallel orientation between layers, which broadens the MR_{obs} curve.

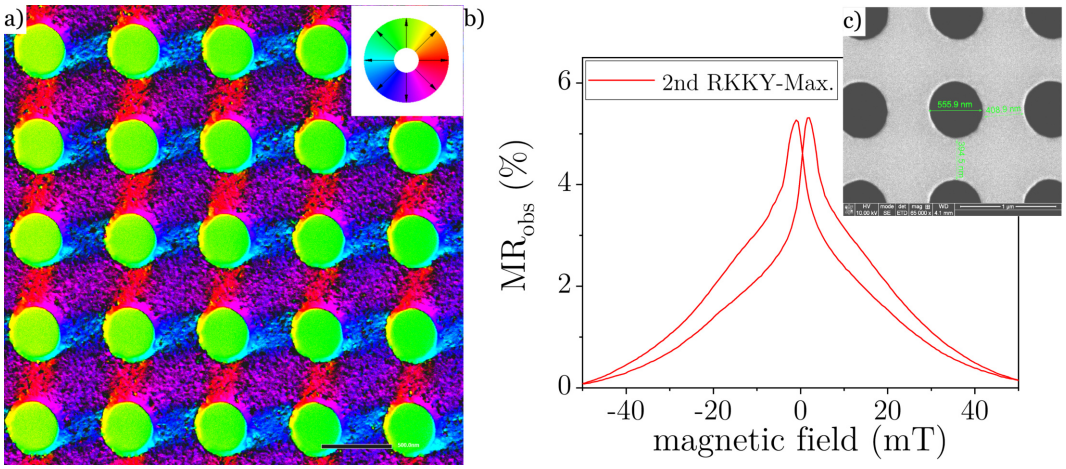

Figure 6.11: a) DPC image of the 500 nm circle pattern in a GMR membrane at the 2nd RKKY-maximum with b) the corresponding GMR curve for the same pattern on a Si wafer using e-beam lithography and the inset c) showing a SEM image for the respective pattern.

Looking at the data for the GMR stack at the second IEC maximum, this hypothesis can be tested for consistency. Figure 6.11 shows a) the DPC image for the same 500 nm circle pattern that was previously shown and b) the corresponding GMR

curve. For the DPC image, the sample was magnetized at -25 ° tilt by the objective lens before it was switched off for the imaging process. Again, the shift in the colors compared to Figure 6.10 a) and Figure 6.7 a) can be explained in two ways. First, the specimen was built in at a different angle with regard to the magnetic field generated by the objective lens. Second, this image shows a superposition of the beam deflection caused by all layers of the thin film stack. Thus, the influence of the non-magnetic spacer, as well as the relative orientation of all magnetic layers contribute to the observed signal. Qualitatively however, the domain pattern close to remanence that is shown in the DPC image, closely resembles the pattern seen previously for the CoFe film and the first IEC maximum. Thus, a similar broadening in the GMR curve to the one observed in the first IEC maximum is to be expected. The results of the electric transport measurement on this system is illustrated in Figure 6.11 b), whereas c) shows an SEM image of the pattern including measurements. Since this measurement is from the second maximum, the coupling is considerably weaker, i.e. the ratio of ferromagnetically coupled area to antiferromagnetically coupled area is larger. The maximum MR_{obs} of 5.4 % is consistent with the result for the unpatterned film.
A broadening of the tails of the peak is clearly visible, which was expected. However, the broadening at the top of the peak, that indicated stabilized domains with an antiparallel orientation of the magnetic films is not seen in this case. Instead, the peak is slim and slightly farther shifted from $H_{ext} = 0$ than for the first IEC maximum. This shift is consistent with experiments on unpatterned Py (3.6 nm)/ Co (3.5 nm)/ Cu (2.6 nm)/ Co(3.9 nm) GMR systems investigated by Hütten *et. al.* in [95]. From [95], it can be estimated that at the second IEC maximum about 38 % of the thin film area is ferromagnetically coupled. As the interaction is overall weaker, this can explain the narrower peak in the observed MR ratio. Additionally, the hypothesis on the connection between the domain structure that is stabilized by the Lorentz field and the GMR discussed above can be expanded. Considering the weaker interlayer coupling and the larger ratio of ferromagnetically coupled material, ferromagnetically and antiferromagnetically coupled areas are likely not a preferential state within a single Lorentz-field-stabilized domain. Hence, a broadening of the peak due to stabilized domains of antiparallel orientation cannot occur.
In conclusion, the micromagnetic simulations for the CoFe layers proved to be surprisingly similar to the observed structures in Cu-Co multilayer GMR systems and were useful to obtain a qualitative estimate of the domain structure in a nanopatterned GMR film. Due to a superposition of contributions from different layers to the total beam deflection, the similarity between simulations and the observed DPC image is less strong, but the qualitative result is consistent and helps to explain the results for the electric transport measurements. Using the GMR curves in combination with the images of the magnetic domain structure, a hypothesis for the interplay between IEC and the Lorentz field in a GMR multilayer system could be formulated. In the following chapter, this model will be extended to more complex patterns such as the triangle and herringbone parquet illustrated in Figure 6.4 c) and d).

6.7.2 Results for complex patterns on a rectangular grid

The triangle and herringbone parquet pattern shown first in Figure 6.4 c) and d) have unique symmetry properties compared to the simpler patterns discussed up to this point. As these patterns are inspired by works on artificial spin ice [90, 89], these patterns are expected to produce interesting domain structures that can be imaged using differential phase contrast. Additionally, such a complex magnetic structure could, depending on the interplay between interlayer exchange coupling (IEC) and the Lorentz field caused by the holes, lead to unique electric transport properties characterized by the GMR curve.

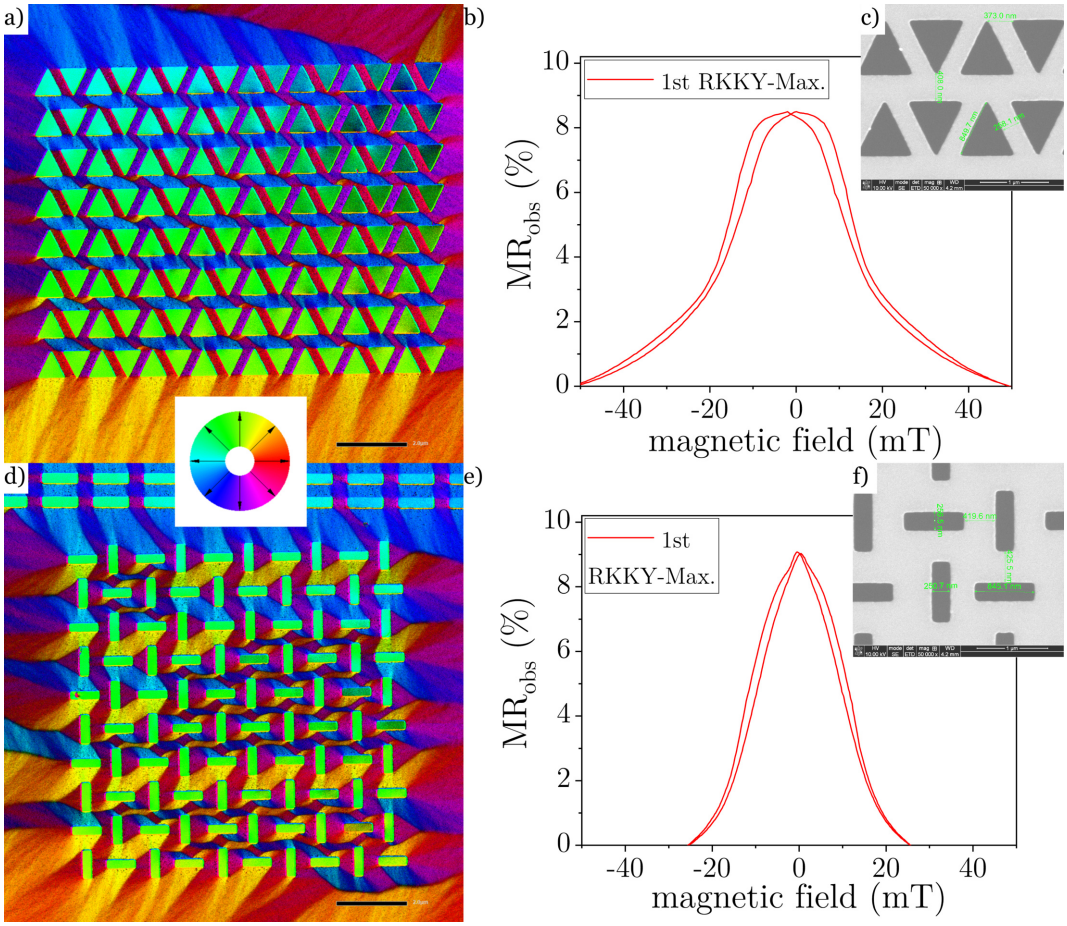

Figure 6.12: Results for more complex patterns in patterned GMR thin film membranes at the first RKKY-maximum: a) DPC image for a triangle pattern with an edge length of roughly 850 nm b) the corresponding GMR measurement for the same pattern on a regular Si wafer prepared by e-beam lithography. c) A SEM image of the triangle pattern. d) DPC image for a herringbone parquet pattern with a hole size of roughly 800 nm x 290 nm b) the corresponding GMR measurement for the same pattern on a Si wafer prepared by e-beam lithography. c) A SEM image of the herringbone parquet pattern.

Figure 6.12 a)-c) shows the DPC and GMR measurements as well as a SEM image of the membrane following the same principle as the data in the previous chapter.

For the DPC image in a) the specimen was magnetized by the objective lens at a tilt of -25 ° before the objective lens was turned off for imaging. The patterns used for the GMR measurement were prepared on a Si wafer as explained in chapter 6.4 and measured at a bias voltage of 70 mV. Figure 6.12 c) contains the measurements for the pattern that were taken directly from the SEM. Each equilateral triangle has an edge length of roughly 850 nm with a width of roughly 400 nm for the horizontal bars and 300 nm for the angled bars.
The DPC image in Figure 6.12 a) shows a particularly regular domain structure, which forms mostly diagonal connections between triangles. On the wider horizontal bars, a regular pattern of rhombic domains forms between the long sides of triangles in different rows. These domains are interrupted by purple domains (at a 45 ° angle) that form on the forward-tilted bars and are sometimes connected in a zigzag pattern over several rows. Similarly, most backward-tilted bars are red domains at a 90 ° angle relative to the purple domains. Similar to the rectangular pattern, domains mostly nucleate from the corners of the holes, since they act as pinning centers. On the left and right fringes of the triangle grid, it can also be seen that smaller domains form at the sharp corners of the triangle that fade into the continuous film at a certain distance. Given the regularity of the domain pattern, the magnetic structure that is stabilized by the triangle grid seems to be quite stable in spite of the angle between adjacent domains.
This is only partly reflected in the GMR measurement in Figure 6.12 b), since the magnetic information in the axial direction can not be imaged by DPC. Similar to the rectangle structure in the previous chapter, the peak of the curve is significantly broadened compared to the unpatterned GMR system, which agrees well with the hypothesis that the domain structure promoted by the Lorentz field is quite stable around $H_{\mathrm{ext}} = 0$. The tails of the peak are also broader than for the unpatterned sample, however, the flanks are not as close to linear as in the curve for the rectangle pattern in Fig. 6.10 d). After surpassing the nucleation field of the stable state at $H_{\mathrm{ext}} = 0$, the magnetic switching probably becomes relatively easy and the broadened tails represent small domains that are pinned to the sharp corners of the triangles, that were discussed above. As the maximum observerd MR ratio did not change compared to other patterns at the first IEC maximum, it can be concluded that the interlayer coupling is largely unaffected by the addition of Lorentz fields.
The DPC results for the herringbone parquet pattern at the first IEC maximum shown in Figure 6.12 d) present a new phenomenon that none of the other samples have. This pattern consists of 800 nm by 290 nm rectangles that are aligned in a way so that the short side is always perpendicular to the center of the long side of adjacent rectangles at a distance of about 420 nm. Since this structure is inspired by works on artificial spin ice where magnetic islands with an easy axis that is determined by shape anisotropy are forced into frustrated magnetic states, it is expected that the Lorentz fields in this pattern also show unique coupling behavior.
At a glance, it is possible to identify different regions of magnetic ordering in this pattern. Some regions form large rhombic domains that connect to the corners of rectangles that are diagonal to each other, for example the yellow domains on the right of the top row. Within these rows, trapezoid domains form between the short and wide sides of adjacent rectangles with a relative angle of 90 ° to the adjacent yellow domains. In the second row from the top, similar structures but with a reversed magnetic induction (blue) and a reversed tilt direction of the rhomboid form. On the left side of the grid, the same structures form, where every other diagonal is

either blue or yellow. These blue and yellow domains, which are at 180 ° relative to one another, are connected by red/purple domains, which represents a perpendicular orientation of the magnetic induction. In the other presented structures, the relative angles of domains were mostly 45 ° and 90 ° which indicates that the "frustrated" Lorentz field promotes more exotic domain structures.
Particularly interesting though is the second kind of region that can be identified in parts of the pattern. In these regions, for example in the space between the second and third row from the bottom of the grid, instead of single domains, complex patterns of multiple domains form. On the diagonal connections between rows of rectangles, magnetic ribbons of blue and red/purple domains form, which are separated by slim yellow domains, which are at a 180 ° angle relative to the blue domains. This extraordinary magnetic state is present throughout the grid and surprisingly stable. Multiple magnetization loops of tilting the specimen to +25 ° and -25 ° in a strong magnetic field generated by the objective lens could not remove this pattern. Since DPC imaging superimposes beam deflection contributions from multiple layers, the origin of these zigzag ribbon domains is unclear. Perhaps this phenomenon is not actually a domain pattern that is present in a single film but rather a superposition of the magnetic contributions from different FM layers. In this case, some parts of the deeper magnetic layers could couple either ferromagnetically or antiferromagnetically because the order promoted by the Lorentz field is competing with the IEC that promotes antiferromagnetic coupling between the layers at $H_{\mathrm{ext}} = 0$. Thus, the visible color contrast is created.
Like the magnetic structure in the DPC images, the electric transport measurements on the herringbone parquet pattern show some unique characteristics, that were not present in the previously discussed films. Whereas the other patterns broadened the resulting GMR curve, which is likely due to a pinning effect of the holes on the domains, the curve in this case is almost as slim as for the unpatterned case with a full width half maximum (FWHM) at around 10 mT. Additionally, the curve shows small kinks near the peak, that are asymmetric, i.e. they only appear on one side of each half loop. Such a shoulder on the GMR curve indicates that there are two regions with different coercive fields and possibly also different pinning or coupling strengths are present in the structure. In an unpatterned Cu-Co multilayer system, a similar effect would not occur without additional pinning layers, that alter the switching behavior of individual magnetic layers [113]. This qualitatively agrees well with the findings in the DPC magnetic imaging for the first IEC maximum since regions with different magnetic structure were clearly identified. The exact mechanism is still unclear however. A possible explanation for the generally low coercive field compared to other patterns with rectangular holes, that should be strong pinning centers, will be given later in this chapter.

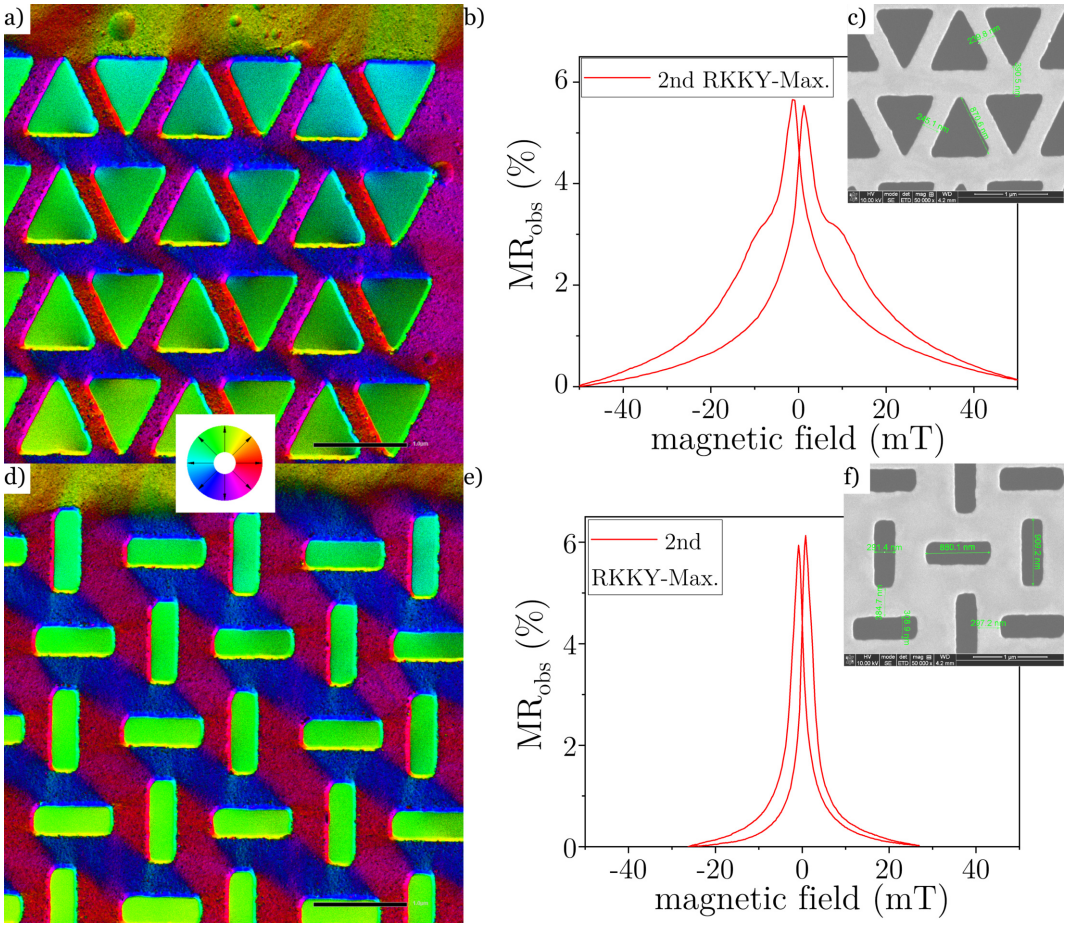

Figure 6.13: Results for more complex patterns in patterned GMR thin film membranes at the second RKKY-maximum: a) DPC image for a triangle pattern with an edge length of roughly 870 nm b) the corresponding GMR measurement for the same pattern on a regular Si wafer prepared by e-beam lithography. c) A SEM image of the triangle pattern. d) DPC image for a herringbone parquet pattern with a hole size of roughly 800 nm x 290 nm b) the corresponding GMR measurement for the same pattern on a Si wafer prepared by e-beam lithography. c) A SEM image of the herringbone parquet pattern.

Given that the unique magnetic order in the herringbone parquet pattern system may be related to an interplay of the Lorentz field and the IEC, it is worth looking at the same system for the second IEC maximum since this should change the dynamic of the two interactions. Figure 6.13 shows the DPC, GMR, and SEM data for the triangle (a-c) and herringbone parquet (d-f) patterned layer system at the second RKKY maximum. Since this system mills faster due to the higher Cu content, the holes are slightly larger than for the previously discussed sample. The equilateral triangles now have an edge length of 870 nm, with horizontal bars of 380 nm and smaller angled bars at 245 nm. In the herringbone parquet, the size of the rectangles increased to 880 nm by 290 nm and the spacing shrank to 300 nm and 380 nm respectively. Otherwise all experimental conditions are identical to those used for the first IEC maximum.
For the triangle pattern, the magnetic structure imaged using DPC looks identical

in almost all aspects to the domain pattern observed for the first IEC maximum, the only exception being that the borders between domains appear slightly less sharp. Therefore, the interpretation of the data remains the same. The GMR data, however, shows a completely different curve shape to the one at the first IEC maximum. Here the maximum MR_{obs} is at 5.9 % which is expected for the second coupling maximum, but instead of a broad peak, it is relatively sharp. Additionally, shoulders appear for each half loop of H_{ext} similar to the herringbone parquet pattern at the first IEC maximum. The tails of the peak remain broad, which is consistent with the other GMR curves. This hints at a magnetic interaction in these patterned films that can not be observed using DPC. A possible explanation for these shoulders is the existence of a metastable magnetic configuration due to an interplay between the Lorentz field and the IEC, which is invisible to the TEM since it occurs in the z-direction.
The DPC image of the herringbone parquet pattern for the second maximum, which is shown in Figure 6.13 d) looks mostly identical to the magnetic structure observed in Figure 6.12 d) for the first coupling maximum. However, in this case the grid only exhibits one of the two domain patterns, which is the simpler kind with large rhombic domains that connect diagonal rectangles of the same orientation. The complex multi-domain ribbons that were visible and very stable for the first IEC maximum are not present in this sample. In spite of this simpler result for the magnetic imaging, the resulting GMR curve for the herringbone parquet at the second coupling maximum in Figure 6.13 e) shows a different behavior than for the first maximum. The shoulder that was present in the first maximum's GMR curve is invisible for this sample. However, the width of the peak has decreased further. Whereas the FWHM for the first coupling maximum was around 10 mT, the observed MR ratio has fallen to almost zero for the second maximum at 10 mT. Such a slim peak is normally a sign of an unstable antiparallel state as a result of bad IEC coupling and is accompanied by a significantly reduced maximum MR_{obs}. Here, the maximum MR_{obs} is at 6.2 % even higher than for the triangle pattern. Thus, the peak shape has, at least in part, a different origin.
A possible explanation for this behavior can be found in the field of artificial spin ice, from which this pattern was inspired. In artificial spin ice, magnetic islands carry an anisotropy so that the magnetization has a preferred axis. However, the islands are arranged in a way that conflicts with this easy axis and generates frustrated magnetic states. When such a system is subjected to an external field in a magnetization loop, a switching of the magnetic islands in an artificial spin ice structure can occur in cascades as the magnetic moments try to reach a low energy state [114]. If the magnetic domain pattern that is promoted by the Lorentz fields of the hole pattern is also metastable in this particular case, the narrow peak of the GMR curve can be explained. Since the objective lens has to be switched off for DPC magnetic imaging, however, it is not trivial to directly observe the magnetization dynamics in this system. Hence, this explanation remains a hypothesis.
In conclusion, the observations of differential phase contrast magnetic imaging and GMR measurements on higher complexity hole patterns in GMR thin film systems have discovered interesting magnetic interactions. For these samples, the correlation between the observed magnetic structure in the DPC and the measured GMR curve is more difficult since shoulders start to appear in the MR_{obs} peak around $H_{ext} = 0$. Additionally, the DPC image for the first IEC maximum of the herringbone parquet pattern shows complex domain patterns that are likely a result of a superposition of

several domain structures from different magnetic layers. These structures showed high stability and were too prevalent to be considered artifacts. A more comprehensive interpretation for the presented data will be given after comparing the observed results to different micromagnetic simulation approaches.

6.7.3 Comparison to CoFe thin films

In order to investigate the origin of the unique multidomain structure that was observed in the differential phase contrast images of the herringbone parquet on a GMR system at the first interlayer exchange coupling maximum, the results are compared to both direct observations and micromagnetic simulations of the pattern on a simple CoFe thin film. This will provide hints to the contribution of the multilayer structure to the cumulative displacement of the electron beam in the TEM, which is the basis for the DPC images.

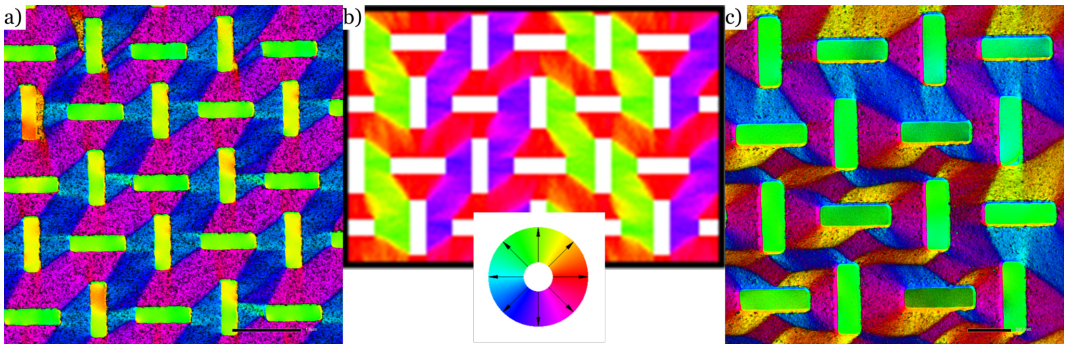

Figure 6.14: a) DPC image of the herringbone parquet pattern after magnetization by the objective lens in the TEM at -25° tilt. b) Micromagnetic simulation of the herringbone parquet pattern taken from a full magnetic reversal loop at -2 mT. c) DPC image of the same pattern on the GMR membrane with the first RKKY-coupling maximum after magnetization by the objective lens at -25° tilt.

Figure 6.14 a) shows the differential phase contrast image of the herringbone parquet in a 60 nm CoFe film on a 5 nm Py seed layer, which is identical to the sample used in chapter 6.6. The film was magnetized by the objective lens at a tilt of -25 ° before the objective lens was switched off for the DPC imaging. The conditions are therefore the same as for the patterned GMR multilayer at the first IEC maximum in Figure 6.14 c), which is the same structure as in Figure 6.12 d) at a higher magnification. Qualitatively, the CoFe in a) organizes in the same domain structure as the GMR multilayer at the second IEC maximum from Figure 6.13 d). Large domains that are rotated 90 ° to the adjacent domains form between rectangles of the same orientation on the off-diagonal. The same structure, albeit on the main diagonal is present for the first IEC maximum in c), whereas the lower half shows a complex multi-domain pattern on the off-diagonal.
The micromagnetic simulation of the herringbone parquet in a CoFe thin film, shown in Figure 6.14 b), which is taken from a full magnetic reversal loop (for the full loop c.f. Appendix) at -1 mT exhibits the same pattern of large domains on both the main and the off-diagonal. In this case, the periodic structure is probably a result of the periodic boundary conditions used for the simulation. It shows, however, that

in principle both the pattern along the main and the off diagonal are stable for symmetry reasons. Thus, the preferred off-diagonal direction of the CoFe film in Fig. 6.14 a) is likely a result of a small angle between the pattern and H_{ext} which induces a preferred direction. As established in chapter 6.6 the micromagnetic simulations with MicroMagus 7.1 provide reliable and consistent results with the experimental data for a single nanopatterned magnetic layer.
Considering the DPC image of the GMR stack in Fig. 6.14 c) represents the cumulative signal of multiple coupled magnetic layers, it is possible to formulate a hypothesis to the origin of the complex observed domain pattern based on the simulation results and the state observed for the simple CoFe-film. Comparing Fig. 6.14 a) and b) carefully, large uniform domains across the pattern diagonal can form for both the horizontal rectangular holes as well as the vertical ones. If a domain connecting the vertical holes on the off-diagonal is superimposed with a domain connecting the horizontal holes on the main diagonal, extra fringes would appear, that closely resemble the multi-domain structure observed in Fig. 6.14 c) for the first IEC maximum in the GMR stack. When instead domains are superimposed, that both connect for example the horizontal holes, the resulting combined pattern changes slightly, which would explain the variance observed in the DPC image. Since these domains on opposite diagonals are oriented at 180 ° relative to each other (green/purple and blue/yellow on the color wheel), which is precisely the state that is strongly promoted by the IEC at the first maximum for neighboring ferromagnetic layers, this interpretation appears plausible.
As these structures are not observed for the second IEC maximum it is possible, that the coupling is too weak. On the other hand, it is possible that this state is just not present in the range of H_{ext} that was present in the TEM during the experiment for example as a result of a remanence magnetization of the objective lens.

6.7.4 Simulations for the GMR of complex patterns

To investigate the origin of the shoulders in the GMR curve of the herringbone parquet and triangle patterned multilayer systems (c.f. Fig 6.12 and 6.13), the observed results are compared to micromagnetic simulations using the MicroMagus 7.1 program. The simulation used the same parameters for the layers as the actual samples at the first IEC maximum Py (3.3 nm)/ CoFe (2.8 nm)/ [Cu (0.9 nm)/ Co (3.1 nm)]x2/ Ru (3 nm). In order to put the simulation results into perspective, both an unpatterned system and the herringbone parquet pattern were simulated in this manner. To obtain realistic results, the rectangles in the herringbone parquet were 848 nm by 256 nm in size and spaced 416 nm in x-direction and 424 nm in y-direction, which closely resembles the real observed structure in the SEM. The GMR curve is calculated from a set of micromagnetic states calculated as part of a full magnetic reversal loop for the multilayer system (c.f. Appendix).

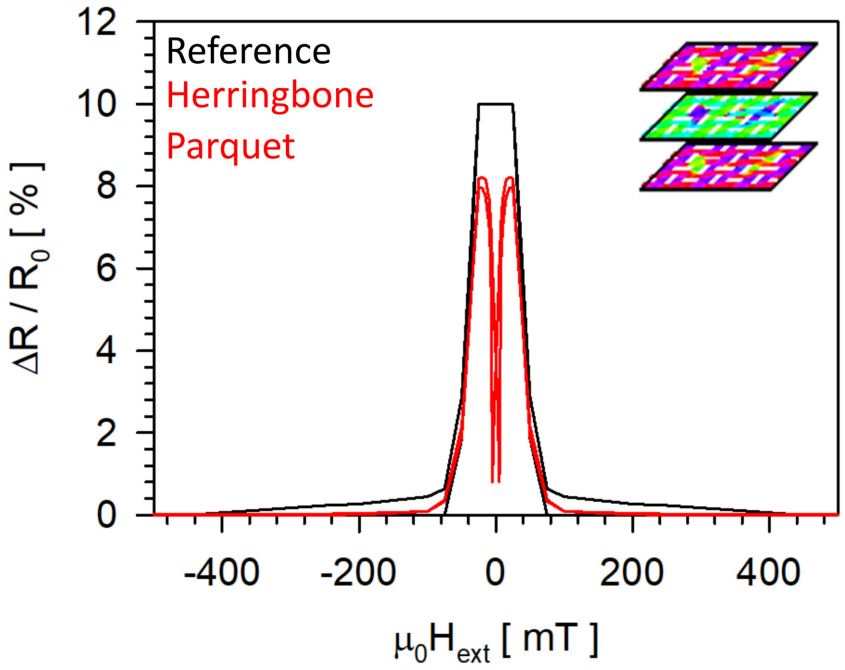

Figure 6.15: Micromagnetic simulation for the GMR curve of a thin film system consisting of Py (3.3 nm)/ CoFe (2.8 nm)/ [Cu (0.9 nm)/ Co (3.1 nm)]x2/ Ru (3 nm) without patterning (black) and with a herringbone parquet hole pattern (red) of 848 nm by 256 nm rectangles with a spacing of 416 nm in x-direction and 424 nm in y-direction. The magnetoresistance curve is calculated from a set of micromagnetic configurations of the ferromagnetic layers. An example for such a configuration at -2 mT is shown in the inset on the top right. Different layers in this model clearly show opposing magnetic orientations. The calculation was performed with the MicroMagus 7.1 program.

Figure 6.15 illustrates the result of the micromagnetic simulation comparing the GMR of an unpatterned Cu-Co multilayer with the given specifications (black) and the same thin film stack with the herringbone parquet pattern (red). The inset in the top right corner shows the magnetic configuration of the ferromagnetic layers at

-2 mT as an example for the base data this graph is derived from. An antiferromagnetic coupling between the layers in this image is clearly visible. The black graph represents the measured data for the unpatterned GMR system very well with a maximum MR_{obs} ($\Delta R/R$) of about 10 % and a FWHM between 5 mT and 10 mT. It is worth noting that the magnetic switching in this calculation is quite sudden, resulting in sharp edges at the peak. While the simulation includes a randomized grain pattern to account for the polycrystalline nature of the thin film, random defects are not considered, which means less pinning occurs that would smoothen and broaden the curve slightly.
Similarly, the red curve for the magnetoresistance of the patterned GMR system is a lot narrower than the actual experimental results for this reason. Additionally, the simulated curve shows a sharp drop of MR_{obs} around $H_{ext} = 0$, which was not observed in any of the previously studied systems regardless of the pattern. Since the simulations were very reliable for both the magnetic structure and the prediction of the magnetoresistance curve for a simple unpatterned system, there has to be an explanation for the difference between the observed MR curve and the simulation for the nanopatterned GMR systems. MicroMagus 7.1 only considers linear exchange terms of the form

$$E_{ex} \approx -\sum_{ij} J_{ij}(\mathbf{S}_i \cdot \mathbf{S}_j) \tag{6.23}$$

with the exchange constant J_{ij} and the spins $\mathbf{S}_i$ and $\mathbf{S}_j$ which scales with the $\sin(\theta)$, with θ being the angle between two spins, for the calculation of the exchange energy contribution. However, in real thin film systems it can be necessary to include higher order exchange terms for example the biquadratic exchange interaction of the form

$$-\sum_{ij} K_{ij}(\mathbf{S}_i \cdot \mathbf{S}_j)^2 \tag{6.24}$$

with the biquadratic exchange constant K_{ij} which scales with $\sin^2(\theta)$[115]. Slonczewski has shown, that Fe/Cr/Fe-trilayer GMR systems exhibit biquadratic coupling that is not of microscopic origin, but instead related to microscopic bilinear coupling that is caused by terraced thickness fluctuations of the epitaxial Cr layer [116]. For the polycrystalline Cu-Co multilayers in this work, this means that thickness fluctuations caused by the surface roughness of the polycrystalline thin films add an additional interlayer exchange coupling term, that is not considered in the calculation. This biquadratic exchange coupling could be responsible for the broadening of the curve and that fact that the sharp dip of MR_{obs} around $H_{ext} = 0$ is not observed.
To investigate a possible influence of a biquadratic exchange interaction term, the GMR curves for Cu-Co thin film systems with variable interlayer exchange coupling were calculated using a free energy minimization approach in MicroMagus 7.1. This approach is identical to the other simulations presented in this work. As the strength of the biquadratic interaction in the investigated samples is unclear, the simulated system was set up with a base MR ratio of 20 % and the strength of the biquadratic exchange coupling was given in units of the "regular" interlayer exchange coupling. For the purpose of the simulations the interlayer exchange coupling is denoted as 'spacerlayer coupling (LC)' and the biquadratic exchange interaction is denoted as 'QC'. Figure 6.16 shows the resulting GMR and hysteresis graphs for a) the first IEC maximum and b) the second IEC maximum in an unpatterned Cu-Co GMR system of the form Py (3.3 nm)/ CoFe (2.8 nm)/ [Cu (0.9 nm)/ Co (3.1 nm)]x2/ Ru

(3 nm). Adding the patterning and therefore the Lorentz fields to this model is not possible with the given code package and would be very computationally intensive.

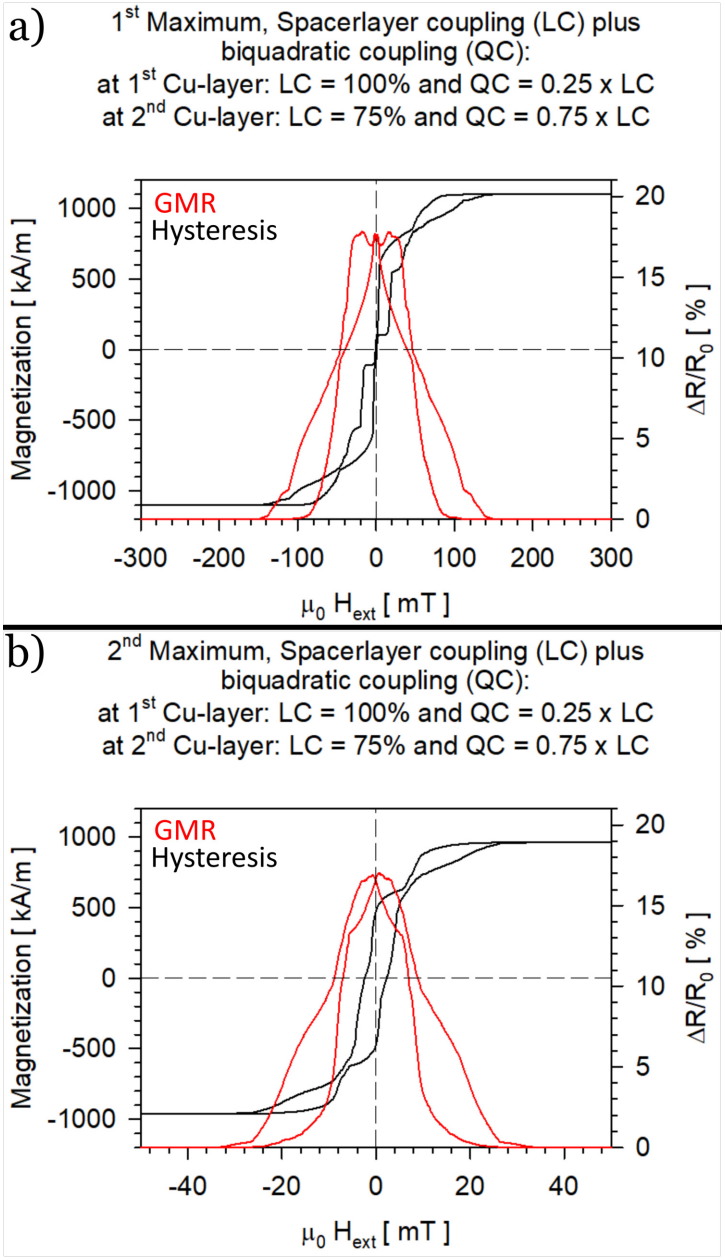

Figure 6.16: Simulations for a Cu-Co GMR system with variable interlayer coupling. The base MR_{obs} of the system was set to 20 %. a) The system is at the first IEC maximum, which is denoted as 'spacerlayer coupling (LC)' with an additional biquadratic exchange interaction term denoted as 'QC' in units of LC. For the first Cu-layer, ideal LC and low (25 %) QC are assumed. In the second layer LC is reduced by 25 % of the base value and QC is at 75 % of LC. In a polycrystalline system, LC can be reduced by increased interface roughness along the growth direction. Thus, QC is stronger when LC is weakened, as QC scales with the interface roughness. b) The same is assumed for the second IEC maximum.

For both IEC maxima, the exchange coupling terms were set up differently for each spacer layer. Across the first spacer layer, the linear coupling term is assumed to be at full strength and the quadratic term is relatively weak at $0.25 \cdot \mathrm{LC}$. In the second layer, the LC term is weakened to 75 % strength and the magnitude of the quadratic term (QC) is increased to $0.75 \cdot \mathrm{LC}$. As the real samples are polycrystalline, it is a reasonable assumption that the interface roughness is not the same across the whole thin film stack. With an increasing number of interfaces the roughness of the films can increase, which weakens the linear interlayer exchange coupling and strengthens the biquadratic interaction since it is a consequence of the interface roughness [116]. The simulated GMR curves for both the first IEC maximum (Fig. 6.16 a)) and the second IEC maximum (Fig. 6.16 b)) show signs of small secondary peaks and a broad shoulder of the central GMR peak. While both GMR curves show only a slight decrease in the maximum MR ratio compared to the 20 % base value, the curve for the second IEC maximum is considerably narrower, which qualitatively agrees with the experimental data. In general, the shape of both curves resembles some but not all of the experimental GMR data that was presented previously for the patterned thin film systems. Changing the relative strength of the QC only lead to minor changes in the resulting simulated GMR curves. However, since these simulations are for *unpatterned* thin films which did not show any notable deviation from the expected Gaussian shape in experiments, a clear influence of a biquadratic exchange interaction term in the presented samples cannot be confirmed.
In spite of some apparent similarities between the presented experimental data and these simulations for a biquadratic exchange contribution, it is impossible to separate the contribution of the biquadratic exchange interaction and the magnetic Lorentz field in the experimental data. Furthermore, none of the unpatterned GMR thin films showed any electrical transport properties that resemble the simulation data presented in Figure 6.16. Therefore, it is reasonable to assume that the new phenomena in the measured GMR curves presented in this work are indeed caused by dipolar interactions due to the magnetic Lorentz field in the patterned thin film systems. Differences to the simulated GMR curves would likely shrink by considering interface roughness, defects, or other minor perturbations in the model system for the calculation.

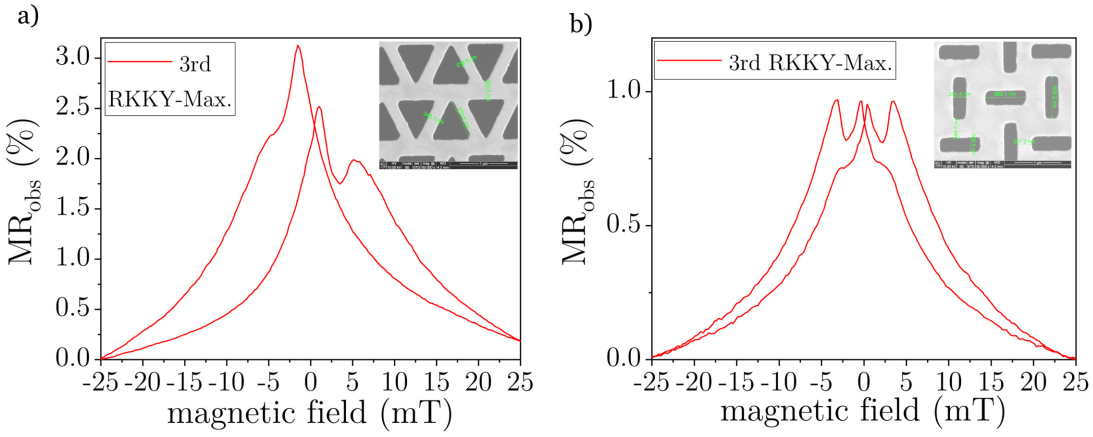

Figure 6.17: GMR measurements for a) the triangle pattern and b) the herringbone parquet pattern of a GMR sample at the third RKKY-Maximum. Both measurement curves show a clear second peak that is not seen in conventional GMR curves.

Figure 6.17 shows the measured GMR data for the third IEC maximum at $t_{Cu} = 3.1\,\text{nm}$ for the triangle pattern (a) and the herringbone parquet pattern (b). Both curves fall to almost 0 % MR_{obs} at 25 mT, however the maximum MR_{obs} for the triangle pattern is with 3.1 % of the same order of magnitude as an unpatterned sample (c.f. Fig. 6.3 a)), whereas the herringbone parquet pattern only produces a maximum MR_{obs} of 0.95 %. More striking than the reduction of MR_{obs} however, is the peculiar shape of the GMR curve. Both samples exhibit a second peak at $\pm 4\,\text{mT}$ for the herringbone pattern and $\pm 5.5\,\text{mT}$ for the triangle pattern, respectively. In the latter case, the magnetic state responsible for these peaks appears to be unstable so that the half loops are asymmetric and one of the side peaks appears as a shoulder of the higher central GMR peak. For the herringbone pattern, the result is completely symmetrical, albeit at a lower absolute MR_{obs}. This unexpected result means, that besides the common antiparallel interlayer coupling around $H_{ext} = 0$, a combination of the interlayer coupling and the patterning results in a second stable antiparallel state at higher values of H_{ext}.
Looking back at the simulation for the first IEC maximum, a similar characteristic was postulated. While the double peak shape of the curve in the simulation is symmetrical around $H_{ext} = 0$ and can thus be interpreted as a dip in the standard GMR curve, the interactions in the real samples shift the curves from the center. It seems that the appearance of a distinct side peak comes at the expense of the maximum observed MR ratio. Therefore, a possible explanation for this phenomenon is that the regions in the pattern that are responsible for the antiferromagnetic coupling at $H_{ext} \approx \pm 5\,\text{mT}$ do not contribute to the antiferromagnetic coupling at $H_{ext} = 0$.
By extension of this hypothesis, the side peak would be present in all previously discussed GMR measurements, particularly those that showed a broadened peak, since the side peak might just not have been shifted far enough from $H_{ext} = 0$ to separate from the central peak. The reason for the difference of the calculation to the experimental results could then be explained by the mathematically quite challenging biquadratic exchange interaction term (c.f. [116]). Since neither this term nor random defects or interface roughness are considered in the simulation, these factors might also obscure the dip in most previously discussed GMR measurements as a

consequence of the generally broader MR curve. A clearer separation, as observed for the third IEC maximum, and in part for the second IEC maximum, could be the result of generally weaker exchange coupling which means that the biquadratic term is also weaker.
This explanation is consistent with the micromagnetic simulations as well as the GMR measurements, and is plausible with regard to the magnetic structures observed using DPC methods in the TEM. Since the magnetization dynamics, especially in the stacking direction (z-direction) of the GMR system, can not be accurately imaged by differential phase contrast, this interpretation remains a plausible hypothesis.

6.8 Summary and Outlook

Since the theory of magnetic Lorentz fields was well established long before the discovery of magnetoresistive effects, the combination of both effects has not gathered much attention to this day. Furthermore, microscopy groups dealing with high resolution differential phase contrast magnetic imaging in the TEM are always curious about samples with interesting structures. Since the range of systems that can be explored using DPC is comparatively small because of the elaborate preparation process necessary, the technique has only recently become more accessible due to the advances in lithography and dual beam methods. In this work, these methods were combined with a well established micromagnetic simulation package as the theoretical backbone to investigate the effect of Lorentz fields in patterned magnetic thin films and giant magnetoresistance devices.
It was successfully demonstrated through a combination of differential phase contrast magnetic imaging and scanning Lorentz microscopy that the magnetic microstructure of free CoFe thin films on 10 nm SiN membranes can be observed. Additionally, the data obtained by these experiments agrees well with micromagnetic simulations of the given system using the real measurements taken from samples via scanning electron microscopy. Similarly, it was possible to image magnetic domain patterns for Cu-Co multilayers, that are a well known system for GMR devices. Since DPC cannot resolve along the beam axis, the obtained data is to be interpreted as a superposition of individual contributions to the electron beam deflection from each magnetic layer. Regardless, the observed domain structure surprisingly still agreed well with simulations of a single patterned CoFe layer for simple patterns like a grid of circular or rectangular holes. Thus, a simulation-guided approach to nanopatterned thin film systems has been established.
More elaborate hole patterns like a triangle grid and a herringbone parquet pattern were intensively investigated for both the magnetic microstructure using DPC and the electric transport properties of the respective GMR devices. This study showed, that these patterns in a multilayer system produce complex domain patterns in the DPC image, that are not present for a single magnetic layer with the same pattern. In combination with the micromagnetic simulations and reference images from single CoFe thin films, a plausible hypothesis for the origin of these patterns in the DPC images of the multilayer system was formulated.
The nanopatterning of GMR multilayer systems showed a significant impact on the transport properties of these systems. In the realm of strong interlayer exchange coupling, the GMR peak was broadened mainly at the top and tail ends. For weaker couplings, the shape of the MR curve changed more dramatically from that of an unpatterned system, which is in good approximation Gaussian-shaped. At the second and third IEC maximum, the observed MR ratio tends to have shoulders or even secondary peaks that are shifted up to 5 mT from $H_{\mathrm{ext}} = 0$. Micromagnetic simulations predict a dip in the central GMR peak even for the first IEC maximum, which was not observed. Since the simulation does not consider biquadratic exchange coupling as a result of the interface roughness of the multilayers, this interaction might be obscured in the experimental data. Given the sum of all results it is plausible that a combination of this biquadratic interaction and the Lorentz fields resulting from the patterning create more than one stable magnetic configuration of the thin film system with antiparallel interlayer coupling, which results in shoulders or secondary peaks in the observed MR ratio.

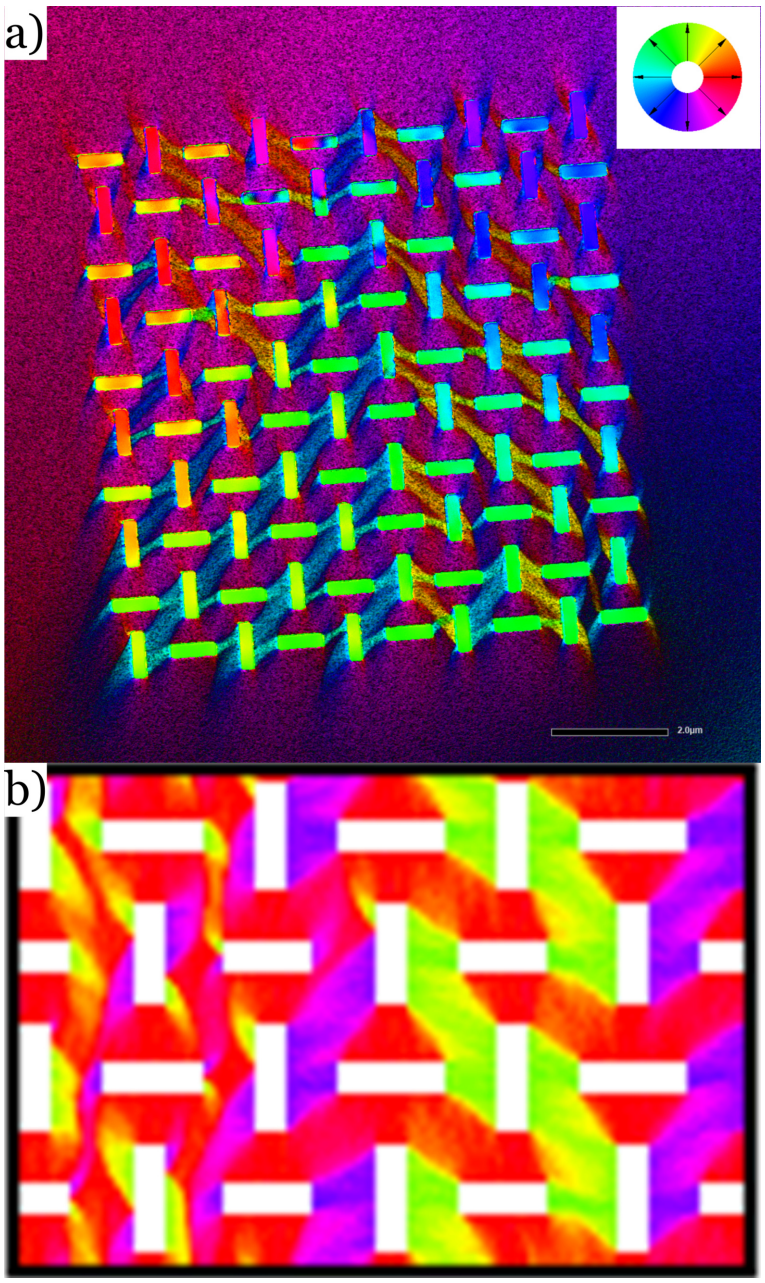

Figure 6.18: a) DPC image of the herringbone parquet pattern on the CoFe membrane at a tilt of -15° with the objective lens at 0500(hex) intensity, which corresponds to roughly 12.5 mT in the thin film plane. b) Micromagnetic simulation of the same pattern in a CoFe thin film. Image taken at 5 mT from a full magnetic reversal loop.

Since DPC imaging is typically performed without the objective lens in a mostly field free environment the imaged systems are close to their remanence magnetization state. Thus, it is hard to image stable states at higher external fields or magnetization dynamics. A possible solution to get a better understanding of the magnetic interactions in patterned thin film systems for a wider field range in future works is to image the magnetic configuration of a sample for a full hysteresis loop using DPC. To achieve the external field in the TEM the objective lens needs to remain

turned on during the magnetic imaging. Alternatively, a specialized sample holder with small, built-in coils would be needed to produce an external field in the sample plane. The specimen has to be tilted relative to the incident electron beam so that the external field generated by the objective lens has an in-plane component. The external field can then be varied over time by adjusting the current flow through the objective lens to obtain snapshots of the magnetic induction in the specimen during a magnetic field sweep.
This technique is promising but also has potential flaws. For example, the actual magnetic field in the sample plane can not be measured in the current TEM setup. Additionally, the tilt angle and the strong out-of-plane component of the external field generated by the objective lens can produce artifacts that need to be carefully considered for the interpretation of the data. Figure 6.18 a) shows a differential phase contrast image of the herringbone parquet in a 60 nm CoFe film on a 5 nm Py seed layer at a tilt angle of -15 ° in an in-plane external field of roughly 12.5 mT. At this angle $\sin(\theta) \approx 0.25$ and the objective lens produces a field of about 50 mT at a power setting of 0500, which is given in hexadecimal. This value has a large margin of error. It can be seen that the domain pattern is qualitatively the same as for the previously discussed images at remanence. However, the domain size has shrunk significantly as a result of the external field.
The micromagnetic simulation shown in Figure 6.18 b) for the same system at 5 mT is in good qualitative agreement with the observed magnetic structure in the DPC image. This is a promising result with regard to future experiments on nanopatterned thin films. However, in order to reach meaningful conclusions using DPC for imaging a complete hysteresis loop in future experiments, the field components in the TEM need to be precisely quantified. Additionally, possible measurement artifacts as a result of the out-of-plane component of the external magnetic field need to be investigated.
With regard to micromagnetic simulations, it would be useful to include a term for the biquadratic exchange interaction in the program possibly using the interface roughness as a fitting parameter for the magnitude of its contribution. This could provide meaningful information to create a reliable model for the interplay between IEC and the magnetic Lorentz field in nanopatterned multilayer systems. The addition of this aspect to the simulation is not trivial and could be part of a future project on this matter.

7 Conclusion and Outlook

In this thesis nanofabrication methods like lithography and the dual beam microscope were used in a wide range of different contexts. The first project used the full capacity of the dual beam microscope for imaging, focused ion beam milling, and even focused electron beam induced deposition of material from a metal-organic precursor in both a bottom-up and top-down approach to create novel granular magnetoresistive devices. The achieved resolution limit with a distance between individual features of 14 nm rivals that of state of the art lithography processes used in the semiconductor industry. While this was technically successful, the limitations in the production speed of the samples and the comparatively low efficiency of the finished devices, make this technique undesirable for larger-scale objects. It does, however, illustrate the overwhelming versatility of the dual beam microscope and nanofabrication techniques in general.
The other projects in this work, namely the development of high-precision optical components for super-resolution microscopy and investigations on nanopatterned magnetoresistive devices using magnetic imaging and micromagnetic simulations, have shown that the full potential of these novel experimental methods is unlocked in collaboration with other fields of science. With the nanostructured aperture grids produced in this work, the localization of fluorescent emitters in super-resolution microscopy, especially across different color channels, can be significantly improved, as a precise ground truth for software-based image correction is established. As nanoscale technology becomes more and more accessible, many disciplines gain the opportunity to explore previously inaccessible phenomena using new preparation techniques. At the same time, the demand for the development of new, smaller, more efficient products with the integration of nanotechnology rises steadily and is not limited to the pioneers of the semiconductor or magnetic data storage industry anymore.
Similarly, the versatile preparation methods offered by lithography and the dual beam microscope help to make other powerful techniques like various TEM imaging modes more accessible by simplifying the complex and time-consuming sample preparation process. This has been demonstrated by the magnetic and electrical characterization of nanopatterned magnetic thin films and multilayers. A combination of careful preparation, high-resolution magnetic imaging and micromagnetic simulations have helped to establish a better understanding of the interplay of different magnetic interactions in these systems. It has been shown that the observed differential phase contrast images agree well with micromagnetic simulations, offering a simulation-guided approach to nanopatterned magnetic thin films. While the theory, particularly for the magnetic Lorentz field, has been well established for a long time, the connection to newer magnetic phenomena like magnetoresistance has not previously been experimentally explored in depth. In this work, the influence of the magnetic Lorentz field on the electrical transport properties of Co-Cu multilayer GMR devices has been clearly established.
Especially in the field of microscopy, nanofabrication techniques have the potential to create new powerful devices or bring about significant improvements in existing devices through the high-precision in the production processes. This is not limited to super resolution microscopy, as this work has shown, but for example anti-reflective nanocoatings already see widespread use for light microscopy, photography, or even eyeglasses. Advanced electron microscopy techniques like differential phase contrast

magnetic imaging in the TEM also benefit greatly from the preparation techniques presented in this work. In spite of the opportunities opened up by nanofabrication techniques, dual beam methods remain comparatively time-consuming which makes them most suitable for prototyping and small-scale production. Given that the semiconductor industry managed to scale up lithography methods to large production volumes and high efficiency, similar methods for the industrial application of focused ion beam techniques might become available in the future.
At the same time this versatility can be one of the biggest downsides, particularly for dual beam methods. Since the dual beam microscope offers a multitude of preparation options, the microscope control software is similarly extensive and a knowledgeable operator is needed for most tasks beyond simple image acquisition. Additionally, specialized tasks may require additional programming to supplement the machine's core features, which has been demonstrated at several points in this work. Therefore, to integrate these novel methods into other highly specialized fields of science, most of the time a team of dedicated experts is needed.
In order to improve the accessibility of dual beam methods in the future, it would be beneficial to either expand the control software capabilities so that the operation of even complex tasks becomes easier. This could be achieved by an extended, well documented core control software that includes functions for automation and possibly machine-learning-driven image recognition to simplify the operation of the machine. Alternatively, a third-party program could be created that accesses the microscopes core controls and provides additional features. Ideally, an open source community-driven platform that would provide a library of additional functions and scripts would help to spread cutting-edge experimental techniques among the scientific community.
Lastly, given the promising results for both the production of optical components as well as the investigations on nanopatterned GMR systems, both projects show great potential for further development in the future. As nanofabrication methods connect to more fields of science, I believe that the potential for completely new research fields and interdisciplinary work will continue to increase.

8 Appendix: Extra simulation data for nanopatterned membranes

This section contains additional micromagnetic simulation data for full magnetic reversal loops of various nanopatterned CoFe thin film and Cu-Co GMR structures. These are supplemental to the discussion in chapter 6.

parameter	value	units
layer thickness (Co)	3.1e-7	cm
layer thickness (Co-Py)	6.1e-7	cm
av. crystallize size (all)	20e-7	cm
spacer thickness (1st max.)	0.9e-7	cm
saturation magnetization (Co)	1422	G
saturation magnetization (Co-Py)	1096	G
exchange stiffness constant A (Co)	3.1e-6	erg/cm
exchange stiffness constant A (Co-Py)	1.802e-6	erg/cm
anisotropy constant (Co)	2.9e4	erg/cm^3
anisotropy constant (Co-Py)	4.5e4	erg/cm^3
interlayer exchange coupling (all)	-0.1076	erg/cm^2
random crystal grains	yes	
exchange weakening at grain boundaries	yes	

Table 8.1: Overview of simulation parameters used for GMR systems in chapter 6.

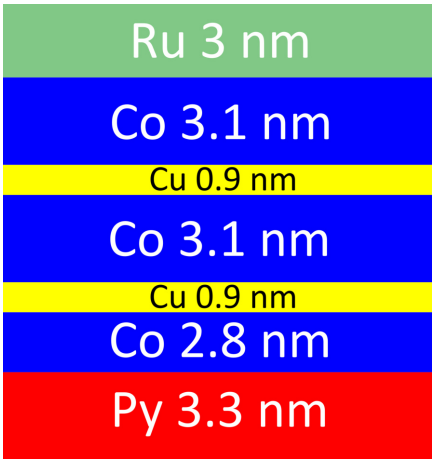

Figure 8.1: Sketch of the GMR multilayer system at the first interlayer exchange coupling maximum used for the simulations related to chapter 6.

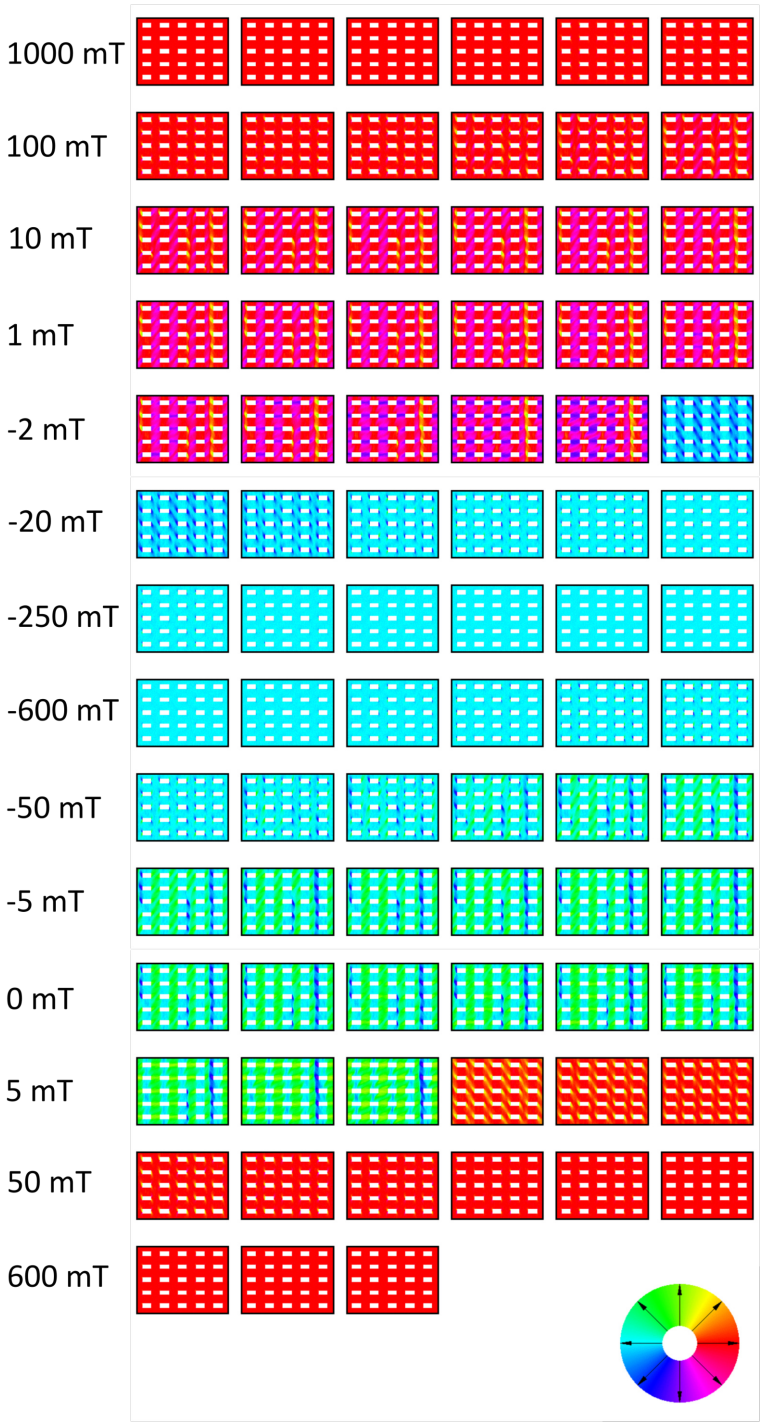

Figure 8.2: Micromagnetic simulation of a full reversal loop of a 60 nm CoFe film on a 5 nm Py seed layer. The pattern consists of 472 nm by 240 nm rectangles with a spacing of 472 nm in x-direction and 448 nm in y-direction, which closely resembles the structure of the real sample, that was characterized and measured in the SEM. Calculations were performed with the MicroMagus 7.1. The external field loop covers a range of ±1000 mT, with decreasing step size close to $H_{\text{ext}} = 0$ to include details of the switching process.

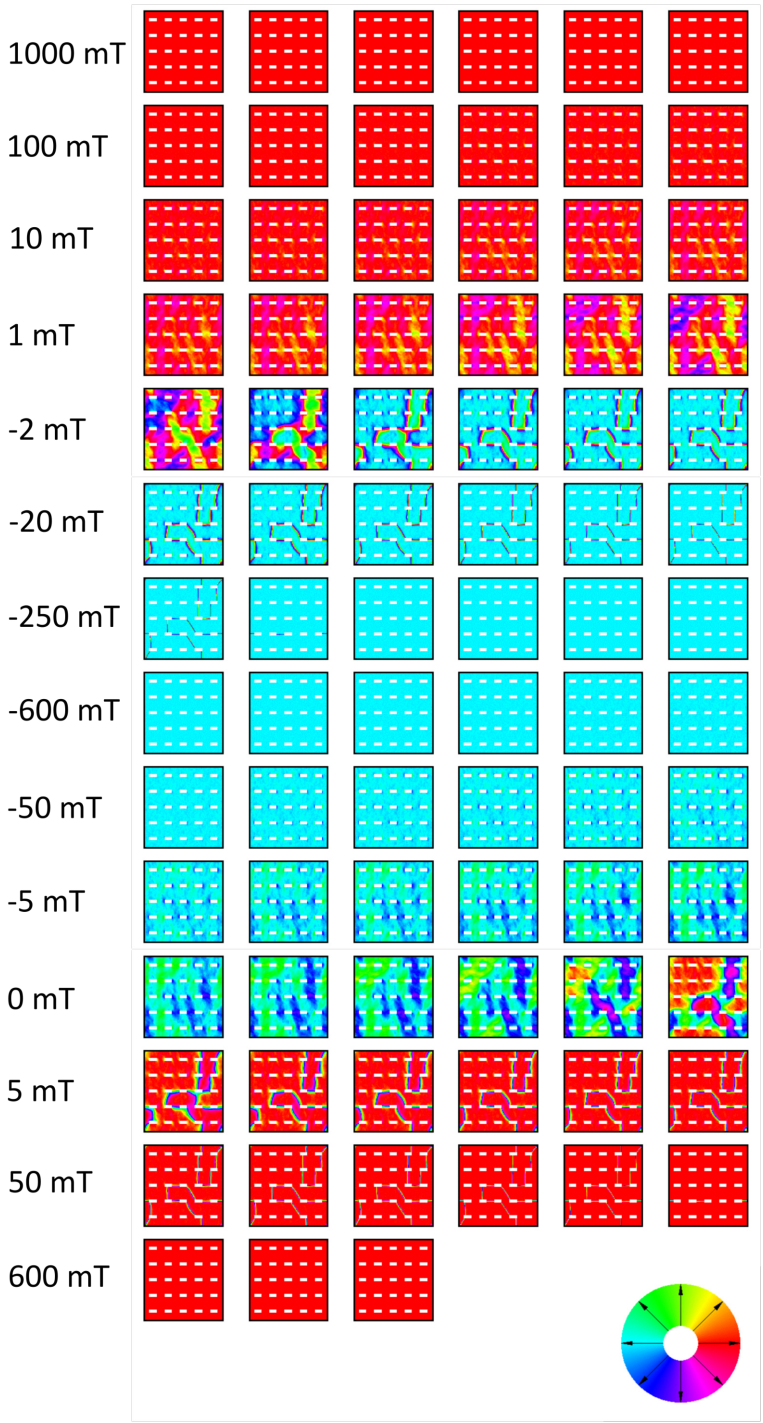

Figure 8.3: Micromagnetic simulation of a full reversal loop of a 60 nm CoFe film on a 5 nm Py seed layer. The pattern consists of 432 nm by 224 nm rectangles with a spacing of 448 nm in x-direction and 688 nm in y-direction, which closely resembles the structure of the real sample, that was characterized and measured in the SEM. This simulation provides a reference for the behavior of the patterned film a large hole spacings, which should approach the result of an unpatterned film in the limit of large distances between individual features. Calculations were performed with the MicroMagus 7.1. The external field loop covers a range of ±1000 mT, with decreasing step size close to $H_{\text{ext}} = 0$ to include details of the switching process.

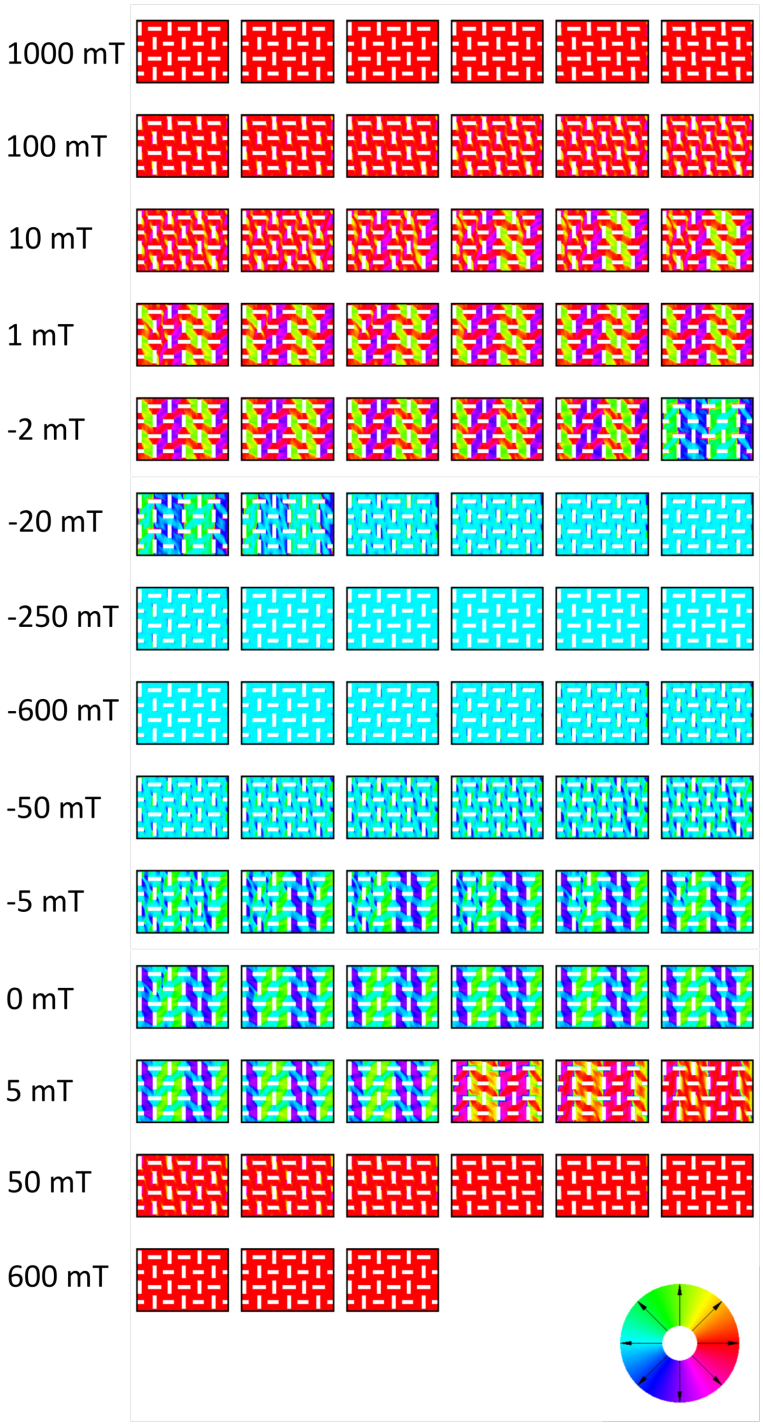

Figure 8.4: Micromagnetic simulation of a full reversal loop of a 60 nm CoFe film on a 5 nm Py seed layer. The pattern consists of 848 nm by 256 nm rectangles with a spacing of 416 nm in x-direction and 424 nm in y-direction, which closely resembles the structure of the real sample, that was characterized and measured in the SEM. Calculations were performed with the MicroMagus 7.1. The external field loop covers a range of ±1000 mT, with decreasing step size close to $H_{\text{ext}} = 0$ to include details of the switching process.

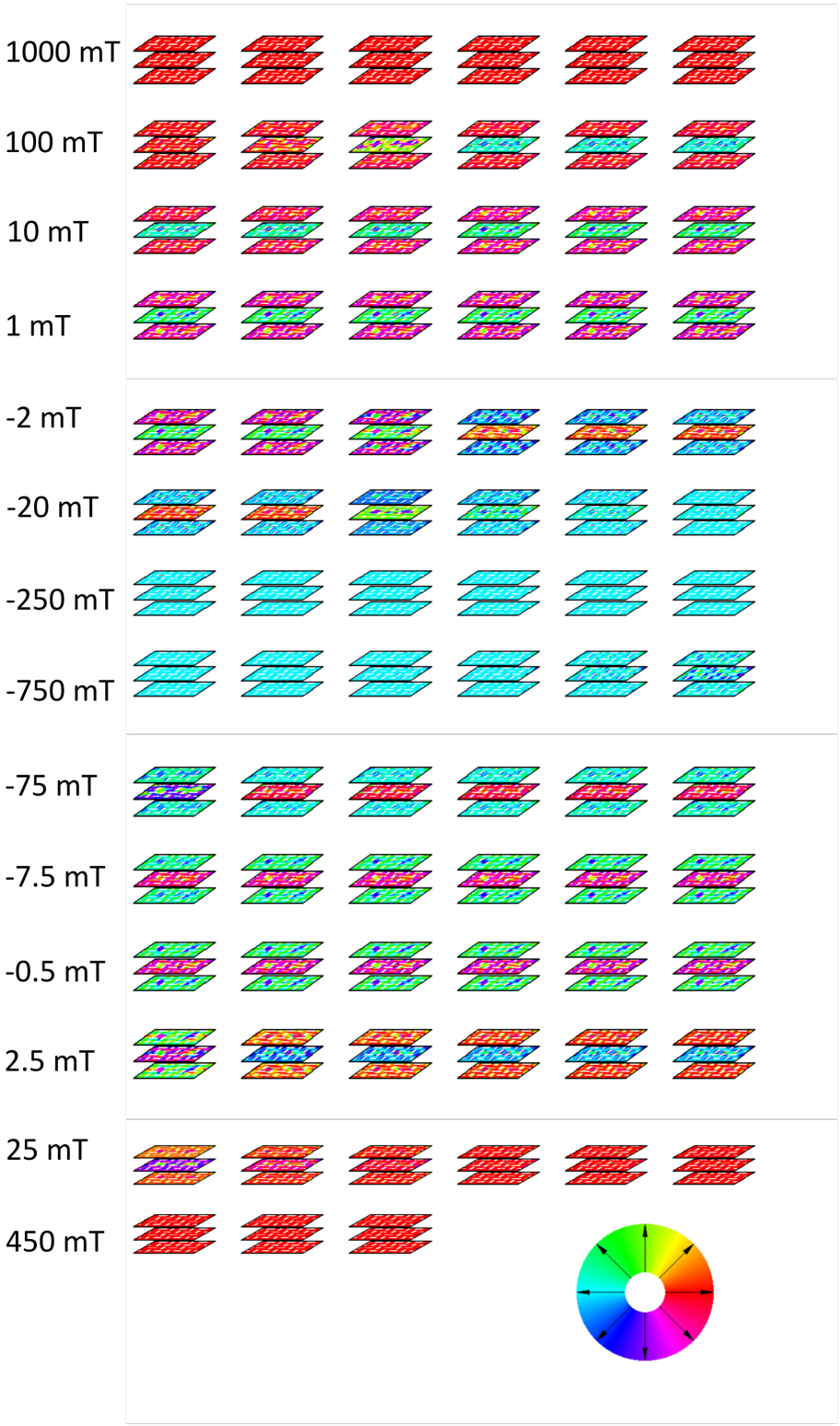

Figure 8.5: Micromagnetic simulation of a full reversal loop of a Py (3.3 nm)/ CoFe (2.8 nm)/ [Cu (t_{Cu})/ Co (3.1 nm)]x2/ Ru (3 nm) GMR stack. The pattern consists of 848 nm by 256 nm rectangles with a spacing of 416 nm in x-direction and 424 nm in y-direction, which closely resembles the structure of the real sample, that was characterized in the SEM. Calculations were performed with the MicroMagus 7.1. The external field loop covers a range of ±1000 mT, with decreasing step size close to $H_{ext} = 0$. Only magnetic layers are shown.

9 List of Publications

1. B. Büker, J.W. Jung, T. Sasaki, Y. Sakuraba, Y. Miura, T. Nakatani, A. Hütten, and K. Hono " Elucidation of the strong effect of an interfacial monolayer on magnetoresistance in giant magnetoresistive devices with current perpendicular to the plane", *Physical Review B*, Vol. 103, p. L140405, April 2021

2. A. Becker, D. Ramermann, I. Ennen, B. Büker, M. Gottschalk, T. Matalla-Wagner, and A. Hütten "The Influence of Martensitic Intercalations in Magnetic Shape Memory NiCoMnAl Multilayered Films", *Entropy*, Vol. 23, p. 462, April 2021

3. A. Hütten, D. Ramermann, B. Büker, A. Becker, I. Ennen, R. Webster, S. McVitie "Imaging microstructural impact on magnetic behavior", *Wiley Analytical Science Magazine*, February 2021

4. D. Kappe, L. Bondzio, J. Swager, A. Becker, B. Büker, I. Ennen, C. Schröder, and A. Hütten "Reviewing Magnetic Particle Preparation: Exploring the Viability in Biosensing", *Sensors*, Vol. 20, p. 4596, August 2020

5. M. Wortmann, N. Frese, A. Mamun, M. Trabelsi, W. Keil, B. Büker, A. Javed, M. Tiemann, E. Moritzer, A. Ehrmann, A. Hütten, C. Schmidt, A. Gölzhäuser, B. Hüsgen, and L. Sabantina "Chemical and Morphological Transition of Poly(acrylonitrile)/ Poly(vinylidene Fluoride) Blend Nanofibers during Oxidative Stabilization and Incipient Carbonization", *Nanomaterials*, Vol. 10, p. 1210, June 2020

6. T. Vordemvenne, D. Wähnert, J. Koettnitz, M. Merten, N. Fokin, A. Becker, B. Büker, A. Vogel, D. Kronenberg, R. Stange, G. Wittenberg, J.F.W. Greiner, A. Hütten, C. Kaltschmidt and B. Kaltschmidt "Bone Regeneration: A Novel Osteoinductive Function of Spongostan by the Interplay between Its Nano- and Microtopography", *Cells*, Vol. 9, p. 654, March 2020

7. Y. Yang, R. Hillman, Y. Qi, R. Korzetz, N. Biere, D. Emmrich, M. Westphal, B. Büker, A. Hütten, A. Beyer, D. Anselmetti, and A. Gölzhäuser "Ultrahigh Ionic Exclusion through Carbon Nanomembranes", *Advanced Materials*, Vol. 32, Issue 8, p. 1907850, January 2020

8. M. Schürmann, F. Oppel, M. Gottschalk, B. Büker, C.A. Jantos, C. Knabbe, A. Hütten, B. Kaltschmidt, C. Kaltschmidt, and H. Sudhoff "The Therapeutic Effect of 1,8-Cineol on Pathogenic Bacteria Species Present in Chronic Rhinosinusitis", *Frontiers in Microbiology*, Vol. 10, p. 2325, October 2019

9. J.F.W. Greiner, M. Gottschalk, N. Fokin, B. Büker, B. Kaltschmidt, A. Dreyer, T. Vordemvenne, C. Kaltschmidt, A. Hütten, and B. Kaltschmidt "Natural and synthetic nanopores direction osteogenic differentiation of human stem cells", *Nanomedicine : Nanotechnology, Biology and Medicine*, Vol. 17, p. 319, April 2019

10. M. Dunz, B. Büker, and M. Meinert "Improved thermal stability in doped MnN/CoFe exchange bias systems", *Journal of Applied Physics*, Vol. 124, p. 203902, November 2018

11. R. Klett, J. Schönle, A. Becker, D. Dyck, K. Borisov, K. Rott, D. Ramermann, B. Büker, J. Haskenhoff, J. Krieft, T. Hübner, O. Reimer, C. Shekhar, J.-M. Schmalhorst, A. Hütten, C. Felser, W. Wernsdorfer, and G. Reiss "Proximity-Induced Superconductivity and Quantum Interference in Topological Crystalline Insulator SnTe Thin-Film Devices", *Nano Letters*, Vol. 18, Issue 2, p. 1264, January 2018

10 Conferences

1. DPG Spring Meeting 2019, Regensburg, Germany: B. Büker, J.W. Jung, Y. Sakuraba, Y. Miura, T. Sasaki, A. Hütten, and K. Hono "Improvement of band matching by monolayer Ni insertion at the $Co_2FeGa_{0.5}Ge_{0.5}$/Ag interfaces in current-perpendicular-to-plane pseudo spin valves", 10 minute talk

2. MMM-Intermag Joint Conference 2019, Washington D.C., USA: B. Büker, J.W. Jung, Y. Sakuraba, Y. Miura, T. Sasaki, A. Hütten, and K. Hono "Improvement of band matching by monolayer Ni insertion at the $Co_2FeGa_{0.5}Ge_{0.5}$/Ag interfaces in current-perpendicular-to-plane pseudo spin valves", 10 minute talk

11 Awards

1. DAAD: "Sprache und Praxis in Japan" Scholarship 2021, Tokyo, Japan: Scholarship for acquisition of profound Japanese language skills and German-Japanese business and research relations, October 2021 - December 2022

References

[1] J. Meyer, *Giant magnetoresistance effects in granular systems with gel matrices.* PhD thesis, Bielefeld University, 2013.

[2] C. Vieu, F. Carcenac, A. Pépin, Y. Chen, M. Mejias, A. Lebib, L. Manin-Ferlazzo, L. Couraud, and H. Launois, "Electron beam lithography: resolution limits and applications," *Applied Surface Science*, vol. 164, pp. 111–117, sep 2000.

[3] C. Mack, *Fundamental Principles of Optical Lithography.* John Wiley & Sons, Ltd, nov 2007.

[4] FEI, *Helios Nanolab 600i - Advanced DualBeam for ultra-high resolution imaging, analysis and fabrication at the nanoscale.* FEI/Thermo Fischer Scientific, 2010. This document concerns an outdated version of FEIs dual beam systems and is no longer available on the official website.

[5] D. Akemeier, *Nano-prototyping and 3D bioimaging with dual beam microscopy.* PhD thesis, Bielefeld University, 2013.

[6] D. Shindo and T. Oikawa, *Analytical Electron Microscopy for Materials Science.* Springer Japan, 2002.

[7] L. Y. Roussel, D. J. Stokes, I. Gestmann, M. Darus, and R. J. Young, "Extreme high resolution scanning electron microscopy (XHR SEM) and beyond," in *Scanning Microscopy 2009* (M. T. Postek, D. E. Newbury, S. F. Platek, and D. C. Joy, eds.), SPIE, may 2009.

[8] T. E. Everhart and R. F. M. Thornley, "Wide-band detector for micro-microampere low-energy electron currents," *J. Sci. Instrum.*, vol. 37, no. 246, pp. 246–249, 1960.

[9] J. Orloff, "Fundamental limits to imaging resolution for focused ion beams," *Journal of Vacuum Science & Technology B: Microelectronics and Nanometer Structures*, vol. 14, p. 3759, nov 1996.

[10] N. Yao, ed., *Focused Ion Beam Systems.* Cambridge University Press, 2007.

[11] R. L. Kubena and J. W. Ward, "Current-density profiles for a ga+ ion microprobe and their lithographic implications," *Applied Physics Letters*, vol. 51, pp. 1960–1962, dec 1987.

[12] *Nanofabrication Using Focused Ion and Electron Beams: Principles and Applications.* OXFORD UNIV PR, May 2012.

[13] I. Utke, P. Hoffmann, and J. Melngailis, "Gas-assisted focused electron beam and ion beam processing and fabrication," *Journal of Vacuum Science & Technology B: Microelectronics and Nanometer Structures*, vol. 26, no. 4, p. 1197, 2008.

[14] M. Huth, F. Porrati, and O. Dobrovolskiy, "Focused electron beam induced deposition meets materials science," *Microelectronic Engineering*, vol. 185-186, pp. 9–28, jan 2018.

[15] M.-M. Walz, M. Schirmer, F. Vollnhals, T. Lukasczyk, H.-P. Steinrueck, and H. Marbach, "Electrons as "invisible ink": Fabrication of nanostructures by local electron beam induced activation of SiOx," *Angewandte Chemie International Edition*, vol. 49, pp. 4669–4673, jun 2010.

[16] A. Botman, J. J. L. Mulders, and C. W. Hagen, "Creating pure nanostructures from electron-beam-induced deposition using purification techniques: a technology perspective," *Nanotechnology*, vol. 20, p. 372001, aug 2009.

[17] E. Villamor, F. Casanova, P. H. F. Trompenaars, and J. J. L. Mulders, "Embedded purification for electron beam induced pt deposition using MeCpPtMe3," *Nanotechnology*, vol. 26, p. 095303, feb 2015.

[18] E. Begun, O. V. Dobrovolskiy, M. Kompaniiets, R. Sachser, C. Gspan, H. Plank, and M. Huth, "Post-growth purification of co nanostructures prepared by focused electron beam induced deposition," *Nanotechnology*, vol. 26, p. 075301, jan 2015.

[19] L. Serrano-Ramón, R. Córdoba, L. A. Rodríguez, C. Magén, E. Snoeck, C. Gatel, I. Serrano, M. R. Ibarra, and J. M. D. Teresa, "Ultrasmall functional ferromagnetic nanostructures grown by focused electron-beam-induced deposition," *ACS Nano*, vol. 5, pp. 7781–7787, oct 2011.

[20] M. Dukic, M. Winhold, C. H. Schwalb, J. D. Adams, V. Stavrov, M. Huth, and G. E. Fantner, "Direct-write nanoscale printing of nanogranular tunnelling strain sensors for sub-micrometre cantilevers," *Nature Communications*, vol. 7, sep 2016.

[21] S. Sengupta, C. Li, C. Baumier, A. Kasumov, S. Guéron, H. Bouchiat, and F. Fortuna, "Superconducting nanowires by electron-beam-induced deposition," *Applied Physics Letters*, vol. 106, p. 042601, jan 2015.

[22] K. Hoeflich, R. B. Yang, A. Berger, G. Leuchs, and S. Christiansen, "The direct writing of plasmonic gold nanostructures by electron-beam-induced deposition," *Advanced Materials*, vol. 23, pp. 2657–2661, apr 2011.

[23] J. D. Fowlkes, R. Winkler, B. B. Lewis, M. G. Stanford, H. Plank, and P. D. Rack, "Simulation-guided 3d nanomanufacturing via focused electron beam induced deposition," *ACS Nano*, vol. 10, pp. 6163–6172, jun 2016.

[24] R. Winkler, J. D. Fowlkes, P. D. Rack, and H. Plank, "3d nanoprinting via focused electron beams," *Journal of Applied Physics*, vol. 125, p. 210901, jun 2019.

[25] L. Keller, M. K. I. A. Mamoori, J. Pieper, C. Gspan, I. Stockem, C. Schroeder, S. Barth, R. Winkler, H. Plank, M. Pohlit, J. Mueller, and M. Huth, "Direct-write of free-form 3d nanostructures with controlled magnetic frustration,"

[26] K. Muthukumar, H. O. Jeschke, R. Valentí, E. Begun, J. Schwenk, F. Porrati, and M. Huth, "Spontaneous dissociation of Co2(CO)8 and autocatalytic growth of Co on SiO2: A combined experimental and theoretical investigation," *Beilstein Journal of Nanotechnology*, vol. 3, pp. 546–555, jul 2012.

[27] J. Moonen and M. Hayles, *Autoscript xT Technical Note*. FEI Company, 2005.

[28] M. Hayes, C. Jiao, S. Reyntjens, D. Wall, J. L. Green, and S. Gilpin, *Helios NanoLab 400/400S/600 System User's Guide*. FEI Company, 2008.

[29] M. N. Baibich, J. M. Broto, A. Fert, F. N. V. Dau, F. Petroff, P. Etienne, G. Creuzet, A. Friederich, and J. Chazelas, "Giant magnetoresistance of (001)Fe/(001)Cr magnetic superlattices," *Physical Review Letters*, vol. 61, pp. 2472–2475, nov 1988.

[30] S. M. Thompson, "The discovery, development and future of GMR: The nobel prize 2007," *Journal of Physics D: Applied Physics*, vol. 41, p. 093001, mar 2008.

[31] T. Nakatani, Z. Gao, and K. Hono, "Read sensor technology for ultrahigh density magnetic recording," *MRS Bulletin*, vol. 43, pp. 106–111, feb 2018.

[32] S. Li, Y. K. Takahashi, T. Furubayashi, and K. Hono, "Enhancement of giant magnetoresistance by L21 ordering in Co2Fe(Ge0.5Ga0.5) heusler alloy current-perpendicular-to-plane pseudo spin valves," *Applied Physics Letters*, vol. 103, p. 042405, jul 2013.

[33] B. Bueker, J. Jung, T. Sasaki, Y. Sakuraba, Y. Miura, T. Nakatani, A. Huetten, and K. Hono, "Elucidation of the strong effect of an interfacial monolayer on magnetoresistance in giant magnetoresistive devices with current perpendicular to the plane," *Physical Review B*, vol. 103, p. l140405, apr 2021.

[34] V. Vovk, *Thermal stability of Py/Cu and Co/Cu giant magnetoresistance (GMR) multilayer systems*. PhD thesis, Westf. Wilhelms-Universitaet Muenster, 2007.

[35] I. Ennen, D. Kappe, T. Rempel, C. Glenske, and A. Huetten, "Giant magnetoresistance: Basic concepts, microstructure, magnetic interactions and applications," *Sensors*, vol. 16, p. 904, jun 2016.

[36] I. Ennen, *Magnetische Nanopartikel als Bausteine fuer granulare Systeme: Mikrostruktur, Magnetismus und Transporteigenschaften*. PhD thesis, Bielefeld University, 2008.

[37] J. Meyer, T. Rempel, M. Schaefers, F. Wittbracht, C. Mueller, A. V. Patel, and A. Huetten, "Giant magnetoresistance effects in gel-like matrices," *Smart Materials and Structures*, vol. 22, p. 025032, jan 2013.

[38] L. Teich, D. Kappe, T. Rempel, J. Meyer, C. Schroeder, and A. Huetten, "Modeling of nanoparticular magnetoresistive systems and the impact on molecular recognition," *Sensors*, vol. 15, pp. 9251–9264, apr 2015.

[39] D. Kappe, *Simulationen der Mikrostruktur und Dynamik von Nanopartikeln im Kontext von Hydrodynamik und magnetoresistivem Transport*. PhD thesis, Bielefeld University, 2019.

[40] C. Reig, S. Cardoso, and S. C. Mukhopadhyay, *Giant Magnetoresistance (GMR) Sensors*. Springer Berlin Heidelberg, 2013.

[41] W. Butler, X.-G. Zhang, D. Nicholson, and J. MacLaren, "Spin-dependent scattering and giant magnetoresistance," *Journal of Magnetism and Magnetic Materials*, vol. 151, pp. 354–362, dec 1995.

[42] T. Valet and A. Fert, "Theory of the perpendicular magnetoresistance in magnetic multilayers," *Physical Review B*, vol. 48, pp. 7099–7113, sep 1993.

[43] S. Lipp, L. Frey, C. Lehrer, E. Demm, S. Pauthner, and H. Ryssel, "A comparison of focused ion beam and electron beam induced deposition processes," *Microelectronics Reliability*, vol. 36, pp. 1779–1782, nov 1996.

[44] "Materialsproject.org - materials explorer." web database.

[45] M. Pozzo, D. Alfè, P. Lacovig, P. Hofmann, S. Lizzit, and A. Baraldi, "Thermal expansion of supported and freestanding graphene: Lattice constant versus interatomic distance," *Physical Review Letters*, vol. 106, p. 135501, mar 2011.

[46] P. J. Flanders, "An alternating-gradient magnetometer (invited)," *Journal of Applied Physics*, vol. 63, pp. 3940–3945, apr 1988.

[47] J. Waddell, S. Inderhees, M. Aronson, and S. Dierker, "Magnetization of cobalt nanodiscs," *Journal of Magnetism and Magnetic Materials*, vol. 297, pp. 54–59, feb 2006.

[48] C. L. Haynes and R. P. V. Duyne, "Nanosphere lithography: a versatile nanofabrication tool for studies of size-dependent nanoparticle optics," *The Journal of Physical Chemistry B*, vol. 105, pp. 5599–5611, jun 2001.

[49] Y. Chen, K. Bi, Q. Wang, M. Zheng, Q. Liu, Y. Han, J. Yang, S. Chang, G. Zhang, and H. Duan, "Rapid focused ion beam milling based fabrication of plasmonic nanoparticles and assemblies via "sketch and peel" strategy," *ACS Nano*, vol. 10, pp. 11228–11236, nov 2016.

[50] J. Bass and W. P. Pratt, "Spin-diffusion lengths in metals and alloys, and spin-flipping at metal/metal interfaces: an experimentalist's critical review," *Journal of Physics: Condensed Matter*, vol. 19, p. 183201, apr 2007.

[51] Allresist, *Positive E-Beam Resist AR-P 610 series.* Allresist, July 2019.

[52] H. Ebert, A. Vernes, and J. Banhart, "Magnetoresistance, anisotropic," in *Encyclopedia of Materials: Science and Technology*, pp. 5079–5083, Elsevier, 2001.

[53] Allresist, *Protective Coating PMMA Electra 92 (AR-PC 5090).* Allresist, July 2016.

[54] Masterbond-Inc., "Electrically conductive adhesive systems." web article, May 2018.

[55] J. Dubowik, "Shape anisotropy of magnetic heterostructures," *Physical Review B*, vol. 54, pp. 1088–1091, jul 1996.

[56] A. V. Svalov, I. R. Aseguinolaza, A. Garcia-Arribas, I. Orue, J. M. Barandiaran, J. Alonso, M. L. Fernandez-Gubieda, and G. V. Kurlyandskaya, "Structure and magnetic properties of thin permalloy films near the "transcritical" state," *IEEE Transactions on Magnetics*, vol. 46, pp. 333–336, feb 2010.

[57] K. Yakushiji, S. Mitani, F. Ernult, K. Takanashi, and H. Fujimori, "Spin-dependent tunneling and coulomb blockade in ferromagnetic nanoparticles," *Physics Reports*, vol. 451, pp. 1–35, oct 2007.

[58] E. Abbe, "Beitraege zur theorie des mikroskops und der mikroskopischen wahrnehmung," *Archiv fuer Mikroskopische Anatomie*, vol. 9, pp. 413–468, dec 1873.

[59] L. Moeckl, D. C. Lamb, and C. Braeuchle, "Super-resolved fluorescence microscopy: Nobel prize in chemistry 2014 for Eric Betzig, Stefan Hell, and William E. Moerner," *Angewandte Chemie International Edition*, vol. 53, pp. 13972–13977, nov 2014.

[60] J. B. Pawley, ed., *Handbook Of Biological Confocal Microscopy*. Springer US, 2006.

[61] A. Yildiz, "Myosin v walks hand-over-hand: Single fluorophore imaging with 1.5-nm localization," *Science*, vol. 300, pp. 2061–2065, jun 2003.

[62] M. Bates, S. A. Jones, and X. Zhuang, "Stochastic optical reconstruction microscopy (STORM): A method for superresolution fluorescence imaging," *Cold Spring Harbor Protocols*, vol. 2013, p. pdb.top075143, jun 2013.

[63] G. T. Dempsey, M. Bates, W. E. Kowtoniuk, D. R. Liu, R. Y. Tsien, and X. Zhuang, "Photoswitching mechanism of cyanine dyes," *Journal of the American Chemical Society*, vol. 131, pp. 18192–18193, dec 2009.

[64] C. Geisler, T. Hotz, A. Schoenle, S. W. Hell, A. Munk, and A. Egner, "Drift estimation for single marker switching based imaging schemes," *Optics Express*, vol. 20, p. 7274, mar 2012.

[65] H. Ma, J. Xu, J. Jin, Y. Huang, and Y. Liu, "A simple marker-assisted 3d nanometer drift correction method for superresolution microscopy," *Biophysical Journal*, vol. 112, pp. 2196–2208, may 2017.

[66] M. Erdelyi, E. Rees, D. Metcalf, G. S. K. Schierle, L. Dudas, J. Sinko, A. E. Knight, and C. F. Kaminski, "Correcting chromatic offset in multicolor superresolution localization microscopy," *Optics Express*, vol. 21, p. 10978, apr 2013.

[67] O. Glushonkov, E. Réal, E. Boutant, Y. Mély, and P. Didier, "Optimized protocol for combined PALM-dSTORM imaging," *Scientific Reports*, vol. 8, jun 2018.

[68] W. Wang, F. Ye, H. Shen, N. A. Moringo, C. Dutta, J. T. Robinson, and C. F. Landes, "Generalized method to design phase masks for 3d super-resolution microscopy," *Optics Express*, vol. 27, p. 3799, feb 2019.

[69] M. Baránek and Z. Bouchal, "Optimizing the rotating point spread function by SLM aided spiral phase modulation," in *19th Polish-Slovak-Czech Optical Conference on Wave and Quantum Aspects of Contemporary Optics* (A. Popiolek-Masajada and W. Urbanczyk, eds.), SPIE, dec 2014.

[70] S. Quirin, S. R. P. Pavani, and R. Piestun, "Optimal 3d single-molecule localization for superresolution microscopy with aberrations and engineered point spread functions," *Proceedings of the National Academy of Sciences*, vol. 109, pp. 675–679, dec 2011.

[71] Allresist, *Negative E-Beam Resist AR-N 7520*. Allresist, Jan. 2017.

[72] D. L. Windt, W. C. Cash, M. Scott, P. Arendt, B. Newnam, R. F. Fisher, and A. B. Swartzlander, "Optical constants for thin films of Ti, Zr, Nb, Mo, Ru, Rh, Pd, Ag, Hf, Ta, W, Re, Ir, Os, Pt, and Au from 24 Angstrom to 1216 Angstrom," vol. 27, p. 246, jan 1988.

[73] Allresist, *Verduenner fuer AR-Resists*. Allresist, Jan. 2016.

[74] Molecular Probes, *Reference Dye Sampler Kit (R-14782)*, July 2003.

[75] Nikon Instruments Inc., *NIKON Super Resolution Microscopes*, 2019.

[76] Nikon, "Nikon n-storm specifications." online, 2021.

[77] D. LLC., "More than double the 3D data with spindle2." doublehelixoptics.com, 2020.

[78] Raith-Nanofabrication, "Laser stage technology for nm-precise sample positioning control." Online. Information from 27.06.2021.

[79] D. R. Smith, "Metamaterials and negative refractive index," *Science*, vol. 305, pp. 788–792, aug 2004.

[80] C. M. Portela, B. W. Edwards, D. Veysset, Y. Sun, K. A. Nelson, D. M. Kochmann, and J. R. Greer, "Supersonic impact resilience of nanoarchitected carbon," *Nature Materials*, jun 2021.

[81] D. Weller, G. Parker, O. Mosendz, A. Lyberatos, D. Mitin, N. Y. Safonova, and M. Albrecht, "Review article: FePt heat assisted magnetic recording media," *Journal of Vacuum Science & Technology B, Nanotechnology and Microelectronics: Materials, Processing, Measurement, and Phenomena*, vol. 34, p. 060801, nov 2016.

[82] A. Kikitsu, "Prospects for bit patterned media for high-density magnetic recording," *Journal of Magnetism and Magnetic Materials*, vol. 321, pp. 526–530, mar 2009.

[83] L. Heyderman, "Magnetisation dynamics." Online, 2015.

[84] S. E. Stevenson, C. Moutafis, G. Heldt, R. V. Chopdekar, C. Quitmann, L. J. Heyderman, and J. Raabe, "Dynamic stabilization of nonequilibrium domain configurations in magnetic squares with high amplitude excitations," *Physical Review B*, vol. 87, p. 054423, feb 2013.

[85] H. Schumacher, D. Ravelosona, F. Cayssol, J. Wunderlich, C. Chappert, V. Mathet, A. Thiaville, J.-P. Jamet, J. Ferre, and R. Haug, "Propagation of a magnetic domain wall in the presence of AFM fabricated defects," *IEEE Transactions on Magnetics*, vol. 37, pp. 2331–2333, jul 2001.

[86] P. Vavassori, R. Bovolenta, V. Metlushko, and B. Ilic, "Vortex rotation control in permalloy disks with small circular voids," *Journal of Applied Physics*, vol. 99, p. 053902, mar 2006.

[87] F. Q. Zhu, G. W. Chern, O. Tchernyshyov, X. C. Zhu, J. G. Zhu, and C. L. Chien, "Magnetic bistability and controllable reversal of asymmetric ferromagnetic nanorings," *Physical Review Letters*, vol. 96, jan 2006.

[88] D. K. Koltsov and M. E. Welland, "Control of micromagnetics in permalloy nanomagnets by means of indentation," *Journal of Applied Physics*, vol. 94, pp. 3457–3461, sep 2003.

[89] W. R. Branford, S. Ladak, D. E. Read, K. Zeissler, and L. F. Cohen, "Emerging chirality in artificial spin ice," *Science*, vol. 335, pp. 1597–1600, mar 2012.

[90] N. Rougemaille, F. Montaigne, B. Canals, A. Duluard, D. Lacour, M. Hehn, R. Belkhou, O. Fruchart, S. E. Moussaoui, A. Bendounan, and F. Maccherozzi, "Artificial Kagome arrays of nanomagnets: A frozen dipolar spin ice," *Physical Review Letters*, vol. 106, feb 2011.

[91] A. Locatelli and E. Bauer, "Recent advances in chemical and magnetic imaging of surfaces and interfaces by XPEEM," *Journal of Physics: Condensed Matter*, vol. 20, p. 093002, feb 2008.

[92] L. cong Peng, Y. Zhang, S. lan Zuo, M. He, J. wang Cai, S. guo Wang, H. xiang Wei, J. qi Li, T. yun Zhao, and B. gen Shen, "Lorentz transmission electron microscopy studies on topological magnetic domains," *Chinese Physics B*, vol. 27, p. 066802, jun 2018.

[93] J. Chapman, R. Ploessl, and D. Donnet, "Differential phase contrast microscopy of magnetic materials," *Ultramicroscopy*, vol. 47, pp. 331–338, dec 1992.

[94] A. Huetten, D. Ramermann, B. Bueker, A. Becker, I. Ennen, R. Webster, S. McVitie, and T. Almeida, "Imaging microstructural impact on magnetic behavior - combined HRTEM and DPC for analysis of Fe/Co2FeSi/Fe layer sandwich," *Wiley Analytical Science Magazine*, 2021.

[95] A. Huetten, T. Hempel, S. Heitmann, and G. Reiss, "The limit of the giant magnetoresistance effect in only three layers," *physica status solidi (a)*, vol. 189, pp. 327–338, feb 2002.

[96] H. Kronmueller, "Mikromagnetische Berechnung der Magnetisierung in der Umgebung unmagnetischer Einschluesse in Ferromagnetika," *Zeitschrift fuer Physik*, vol. 168, pp. 478–494, oct 1962.

[97] W. Demtroeder, *Experimentalphysik 2*. Springer Berlin Heidelberg, 2017.

[98] W. Nolting, *Grundkurs Theoretische Physik 3*. Springer Berlin Heidelberg, 2013.

[99] C. Kittel, *Einfuehrung in die Festkoerperphysik*. MuenchenWien: Oldenbourg, 2002.

[100] G. Arfken, *Mathematical methods for physicists*. Boston: Elsevier, 2005.

[101] Geek3, "Vfpt-sphere-magnet-inside.svg," *Attribution-Share Alike 4.0 International*, July 2018. Online at wikimedia commons.

[102] N. Bo, G. Zhao, H. Zhang, L. Chen, and X. Wang, "Nucleation field, hysteresis loop, coercivity mechanism and critical thickness in composite multilayers with perpendicular anisotropy," *Solid State Communications*, vol. 151, pp. 346–350, mar 2011.

[103] H. Kronmueller, "Theory of nucleation fields in inhomogeneous ferromagnets," *physica status solidi (b)*, vol. 144, pp. 385–396, nov 1987.

[104] D. Berkov, "Micromagus," 2021.

[105] D. Berkov and N. Gorn, *Handbook of Advanced Magnetic Materials*. Springer US, Nov. 2005. Chapter 12 of Vol. II.

[106] A. Petford-Long and J. Chapman, *Magnetic Microscopy of Nanostructures*. Springer-Verlag GmbH, Sept. 2004.

[107] N. Shibata, S. D. Findlay, Y. Kohno, H. Sawada, Y. Kondo, and Y. Ikuhara, "Differential phase-contrast microscopy at atomic resolution," *Nature Physics*, vol. 8, pp. 611–615, jun 2012.

[108] D. Ramermann, *Magnetic investigations in the TEM: EMCD and DPC measurements on Heusler alloys towards interfacial properties and magnetic characterization of thin films*. PhD thesis, Bielefeld University, Dec. 2020.

[109] G. Bracco and B. Holst, eds., *Surface Science Techniques*. Springer-Verlag GmbH, Jan. 2013.

[110] M. A. Ruderman and C. Kittel, "Indirect exchange coupling of nuclear magnetic moments by conduction electrons," *Physical Review*, vol. 96, pp. 99–102, oct 1954.

[111] K. Akabli, H. T. Diep, and S. Reynal, "Spin transport in magnetic multilayers," *Journal of Physics: Condensed Matter*, vol. 19, p. 356204, aug 2007.

[112] R. H. Yu, S. Basu, Y. Zhang, A. Parvizi-Majidi, and J. Q. Xiao, "Pinning effect of the grain boundaries on magnetic domain wall in FeCo-based magnetic alloys," *Journal of Applied Physics*, vol. 85, pp. 6655–6659, may 1999.

[113] F. Radu and H. Zabel, "Exchange bias effect of ferro-/antiferromagnetic heterostructures," in *Springer Tracts in Modern Physics*, pp. 97–184, Springer Berlin Heidelberg, 2008.

[114] S. Lendinez and M. B. Jungfleisch, "Magnetization dynamics in artificial spin ice," *Journal of Physics: Condensed Matter*, vol. 32, p. 013001, oct 2019.

[115] A. Kartsev, M. Augustin, R. F. L. Evans, K. S. Novoselov, and E. J. G. Santos, "Biquadratic exchange interactions in two-dimensional magnets," *npj Computational Materials*, vol. 6, oct 2020.

[116] J. C. Slonczewski, "Fluctuation mechanism for biquadratic exchange coupling in magnetic multilayers," *Physical Review Letters*, vol. 67, pp. 3172–3175, nov 1991.